1-10-2019

Atomic Force Microscopy Tip-enhanced Laser Ablation

Fan Cao
Louisiana State University and Agricultural and Mechanical College

ATOMIC FORCE MICROSCOPY TIP-ENHANCED LASER ABLATION

A Dissertation

Submitted to the Graduate Faculty of the
Louisiana State University and
Agricultural and Mechanical College
in partial fulfillment of the
requirements for the degree of
Doctor of Philosophy

in

The Department of Chemistry

by
Fan Cao
B.Sc., China Pharmaceutical University, 2011
M.S., Hong Kong Baptist University, 2012
May 2019

ACKNOWLEDGEMENTS

I would like to express my great appreciation to my advisor, Dr. Kermit Murray, who generously helped me through my entire Ph.D. career. Thank you for your patient guidance and encouragement whenever I encountered difficulties during my research that were hard for me to conquer. I have learned quite a lot in your lab, such as experimental design, instrumentation built-up, and paper writing. I can hardly achieve any of these without you sharing your knowledge. It is an honor for me to work in your lab and contribute to your great research work. I also want to thank Dr. Megan Macnaughtan, Dr. Louis Haber, and Dr. Touria Khannous for being my committee members with their great support and wise advice.

I would like to thank all the current and former group members, Dr. Chinthaka Seneviratne, Kelin Wang, Bijay Banstola, Chao Dong, Remi Lawal, Achala Priyadarashani, and Jamira Stephenson for all your help during my research in this lab. Especially, I want to express my gratitude to our postdoc, Dr. Fabrizio Donnarumma, who accompanied me through my whole Ph.D. career. Without your kind guidance, I would not be able to have a quick start regarding all sorts of instruments and experiments in Dr. Murray's lab.

I also want to thank my family and friends who provided me their love and encouragement in both my research and daily life here in the US. Special thanks go to my grandparents, Xianzu Cao and Yunxia Wu, who stimulated my passion for pursuing the Ph.D. career aboard.

TABLE OF CONTENTS

LIST OF FIGURES

LIST OF ABBREVIATIONS AND SYMBOLS

AFM	Atomic force microscopy
APCI	Atmospheric pressure chemical ionization
BBO	Barium boron oxide
DNA	Deoxyribonucleic acid
EDX	Energy dispersive X-ray spectroscopy
EI	Electron ionization
ESI	Electrospray ionization
GFP	Green fluorescent protein
ICP-MS	Inductively coupled plasmon mass spectrometry
IMS	Imaging mass spectrometry
IR	Infrared
IT-TOF	Ion trap time of flight
ITO	Indium tin oxide
LCM	Laser capture microdissection
MALDI	Matrix assisted laser desorption/ionization
MS	Mass spectrometry
Nd:YAG	Neodymium-doped yttrium aluminum garnet
OPO	Optical parametric oscillator
PCR	Polymerase chain reaction
RNA	Ribonucleic acid
SIMS	Secondary ion mass spectrometry
SEM	Scanning electron microscopy

SNOM	Scanning near-field optical microscopy
a-SNOM	Aperture scanning near-field optical microscopy
s-SNOM	Scattering scanning near-field optical microscopy
SPM	Scanning probe microscopy
STM	Scanning tunneling microscopy
TEF	Tip-enhanced fluorescence
TELA	Tip-enhanced laser ablation
TERS	Tip-enhanced Raman spectroscopy
TEM	Transmission electron microscopy
TOF	Time-of-flight
UHV	Ultrahigh vacuum

ABSTRACT

In the present work, an apertureless atomic force microscope (AFM) tip-enhanced laser ablation (TELA) system was developed and investigated. An AFM was coupled to an optical parametric oscillator (OPO) wavelength tunable laser for sample ablation with a submicron sampling size. The AFM was used to image the surface and hold the AFM tip 10 nm above the sample surface. The AFM tip is coated with a layer of gold with a thickness of 35 nm. The incident laser wavelength was tuned in the visible and near-infrared (IR) region and focused on the AFM tip. With the tip-enhancement effect, ablation craters on the surface with a submicron size were obtained. The mechanism of TELA was investigated using anthracene and three laser dyes: rhodamine B, methylene blue, and IR 797 chloride. All samples were prepared in thin films and the laser energy was set just below their far-field ablation threshold. The wavelength was tuned from 450 to 1100 nm to cover the visible and near-IR range. It was found that ablation is independent of the absorption of the compounds. The ablation crater volume was measured and found to have a maximum at 500 nm and an approximately linear drop to 800 nm. Craters could not be produced between 800 and 1200 nm and were slightly smaller at 450 nm compared to 500 nm. Apertureless TELA was then performed to sample plasmid DNA with 532 nm, which resulted in a sampling volume of 0.14 μm^3 with 12% in variation. The captured DNA was amplified and the amount of sample transferred from each ablation crater was quantitated at 20 ag/spot.

CHAPTER 1. INTRODUCTION

The work discussed in this thesis is aimed at small-scale sampling of biomolecules. For tissue cells, the commonly used analysis methods are based on bulk analysis where the result is obtained by averaging the data from all the cells. Thus, the chemical information from single cells is lost during the bulk analysis approach. Alternatively, single cells can be targeted at smaller sampling scales, which can facilitate a more accurate and precise characterization of a given cell. Atomic force microscopy (AFM) tip-enhanced laser ablation (TELA) was used in this work for large biomolecule sampling with a sub-micron size. The challenges in exploring the small sized world are introduced. An overview of AFM and near-field effect is also covered in this chapter.

1.1 Exploring the Nano-world

As a unit of length measurement, the nanometer (nm) is a well-known quantity. The diameter of an atom is a tenth of a nanometer and the atomic nucleus size is roughly one hundred thousand times smaller. The diameter of an electron is less than a millionth of a nanometer.[1]

After the famous talk "There's Plenty of Room at the Bottom" given by Richard Feynman at Caltech in 1959,[2] the nanometer has become more than a length unit but rather the core of the new fields of nanoscience and nanotechnology. Nanoscience is the science of nano-structures and measuring of the properties of matter at the nanometer level, and manipulation and handling of nano-materials.[3] Three main challenges for exploring nano-world were claimed, especially for the field of information processing: miniaturization in solid-state technology, complexity in chemistry, and numerically intensive computation.[3]

The rapid development in modern nanoscience and nanotechnology has achieved many milestones in size reduction and capability improvement of computers.[4-7] In addition, there have been great contributions to the fields of medicine, environment, energy, and materials.[8] To explore

the nano-scale, tools with nanometer or sub-nanometer precision are necessary. The major tools in nanoscience and nanotechnology include beam methods,[9-14] probe methods,[15-17] computational methods,[18-20] and new materials.[21-23] Beam methods are the typical fabrication approach for nano-patterning whereas computational methods are used for theoretical studies. New nano-materials with appropriate properties are also needed. Among these tools, probe methods with the ability to provide direct surface information of the sample at the nanometer scale have drawn great attention for decades. AFM has become one of the essential tools to explore the nano-world.

1.2 Atomic Force Microscopy

AFM is a high resolution imaging technique that was first introduced in 1986 by Binning and coworkers.[24] In contrast to conventional optical microscope techniques, AFM imaging utilizes a probe to scan a surface by the physical interaction between the probe and surface down to atomic level resolution.

Another approach to achieve atomic level resolution is the electron microscope, which utilizes a focused electron beam to interrogate the sample.[25-26] Two commonly used techniques in electron microscopes are scanning electron microscopy (SEM) and transmission electron microscopy (TEM). An advantage of AFM imaging over SEM and TEM is that AFM can simultaneously provide measurements in the X, Y, and Z axes. A resolution comparison of AFM to SEM, TEM, and conventional optical microscopy is shown in Figure 1.1.[27]

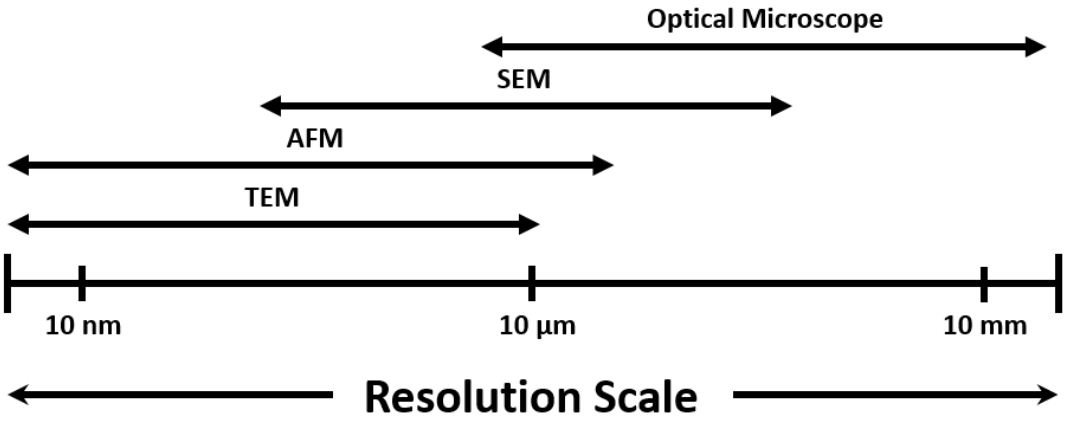

Figure 1.1. Resolution comparison of different microscopy techniques

The working principle of an AFM is similar to that of a stylus profiler that uses a sharp tip dragged along a surface. There is a mirror mounted on the back of the stylus that reflects a light source onto a detector. When the stylus is scanned over the surface, the motion of the cantilever is monitored by the movement of the reflected light to build up a map of the sample height. This surface profiling strategy was applied to develop the scanning probe microscope (SPM) which includes two primary forms, AFM and scanning tunneling microscopy (STM).[28] In 1982, STM was developed and was used to determine the distance between a tip and a conductive surface by measuring the tunneling current.[29-30] Unlike STM, AFM does not require a conductive surface.

AFM imaging techniques are based on the direct physical interaction between a sharp tip and the surface. A schematic of the AFM working principle is shown in Figure 1.2. An AFM system consists of a cantilever and a tip which are mounted to a piezoelectric actuator, a laser, and a four-segment photodiode detector that is position sensitive.[31] The laser beam is directed to the back of the cantilever and reflected to the photodetector. This process requires alignment of the laser beam by reading the photodiode signal to confirm that the laser is reflected onto the center of the detector.

The sample is mounted on a three-dimensional scanner stage where voltage is applied for precise movement at sub-nanometer resolution.[32]

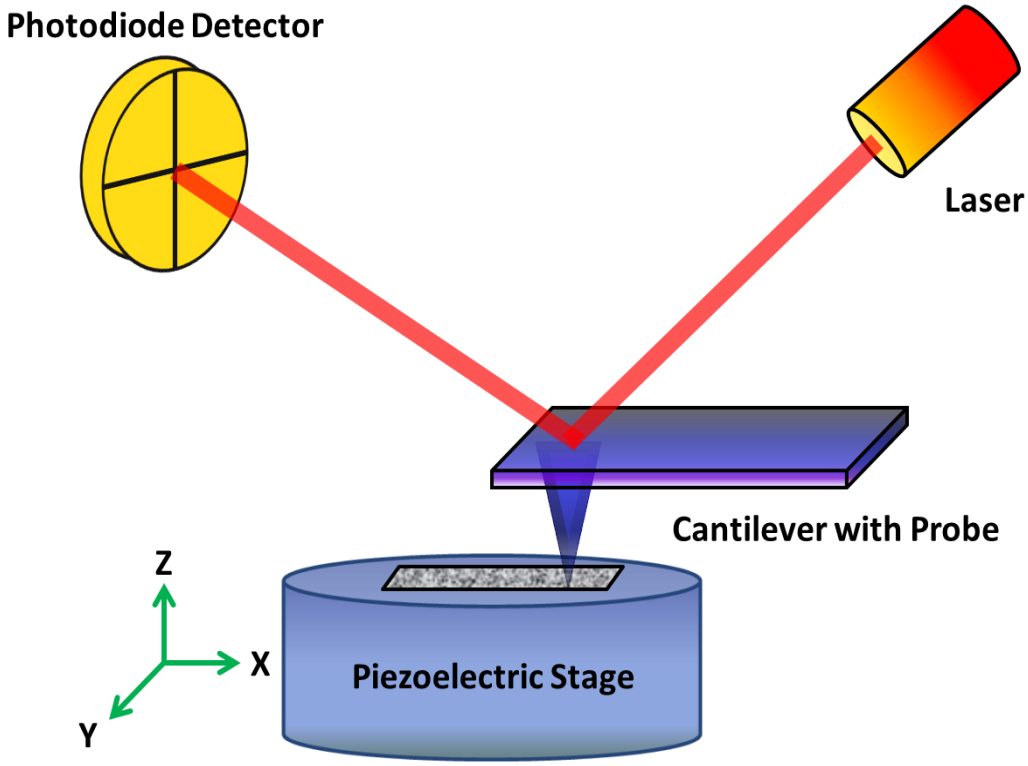

Figure 1.2. Working principle of the AFM

When the AFM probe comes into contact with the surface, the cantilever bends which results in laser beam deflection in both vertical and horizontal directions.[33] With the photodiode detecting the signal, the movement of the cantilever is measured and recorded through computer software. This feedback also enables the control at either a constant force or a constant height above the surface. In the former case, the height deviation is recorded whereas the deflection force is obtained in the latter.[31] In both cases, the topography of the surface is mapped.

1.2.1 AFM Operation Modes

An AFM can be operated in three modes: contact, non-contact, and tapping, which are based on different interaction forces between the AFM tip and the surface. These interactions include attractive forces due to van der Waals interactions, electrostatic and chemical forces, repulsive forces due to hard sphere repulsion and Coulomb interactions.[34] The interaction force curve plotted as a function of the distance between the tip and the surface is shown in Figure 1.3. The three AFM modes are also depicted in this Figure. Details of each mode are discussed below.

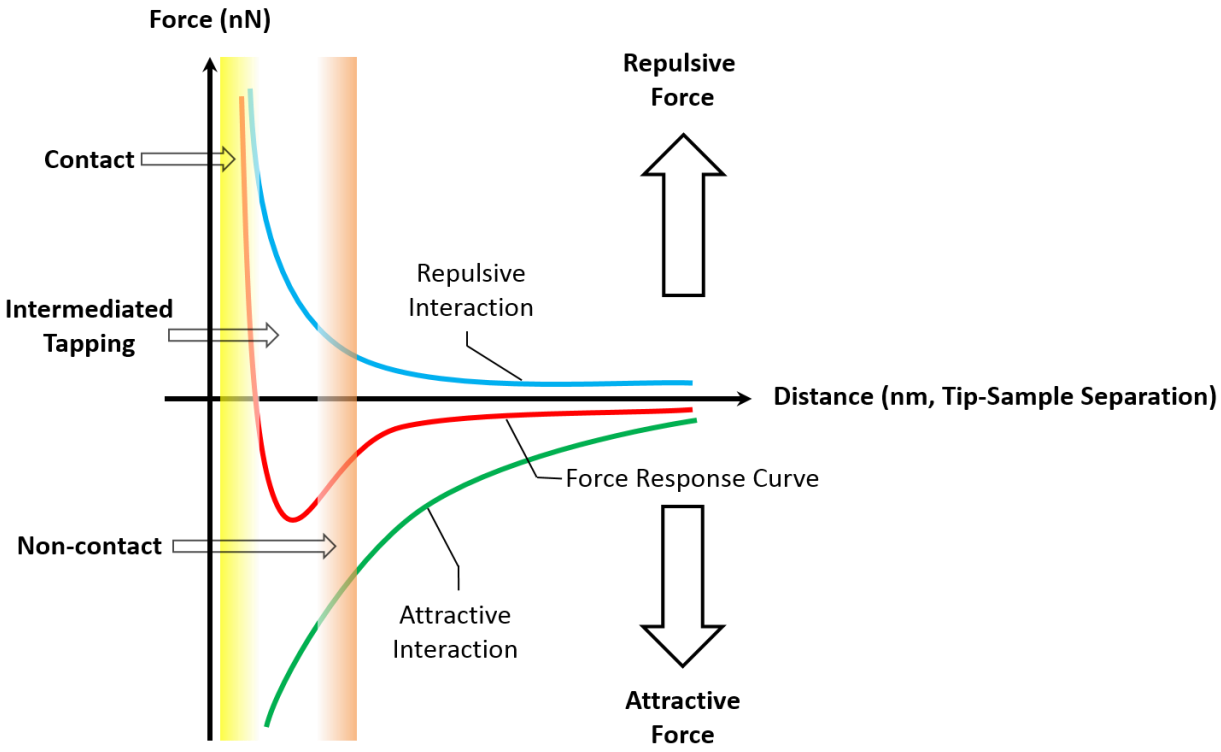

Figure 1.3. Interatomic force curve as a function of the distance between the tip and the surface

Contact Mode

Contact mode was the first operational mode developed for AFM. Here, the AFM tip is in physical contact with the surface during the scanning process. The main interaction between the tip and the surface is the repulsive force, which is depicted in Figure 1.3. A schematic of contact mode AFM operation is shown in Figure 1.4a. Either the height or force of the cantilever is held constant in this mode.

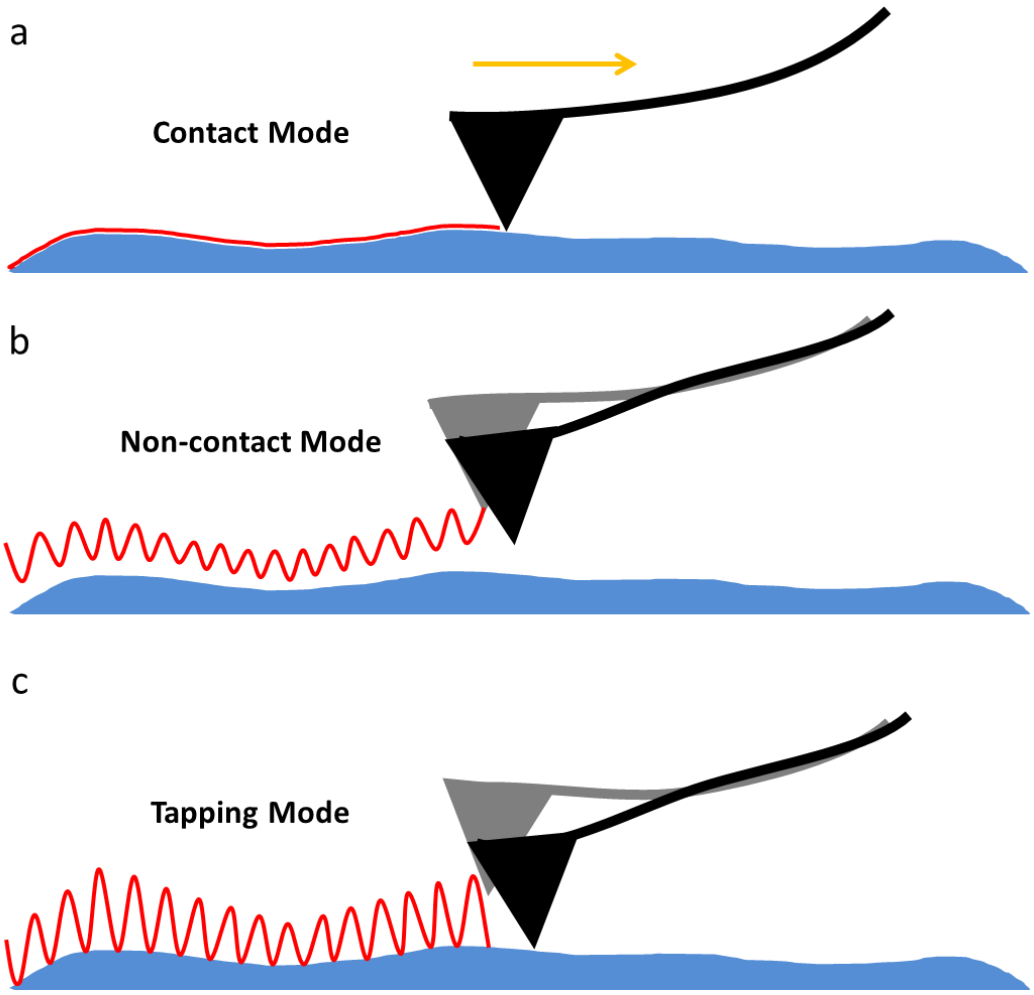

Figure 1.4. Operation modes of AFM: a) contact mode, b) non-contact mode, c) tapping mode

In constant height mode, the height of the AFM probe does not change when scanning across the surface. A bend or twist of the cantilever results in laser deflection which provides a measure of the displacement of the cantilever to map the topography of the sample. However, if the AFM tip is scanned over excessively steep parts of the surface, the tip may get damaged if it hits the surface with too much force.[35]

In constant force mode, the cantilever is held at a constant force according to the laser deflection. By applying the required voltage, the actuator attached to the cantilever moves the tip up or down to compensate for the deflection change during the scan. In this case, the voltage applied to the actuator contains the surface topography information. Constant force mode has a larger height measuring range than constant height mode but has slower scan rates.[36]

Contact mode AFM imaging requires direct contact with the surface, which makes it difficult to image soft materials. The lateral movement of the tip against the surface may result in shear forces, which may alter the surface and distort the image topography.[31] Despite the limitations, contact mode AFM is a widely used measurement tool for nano-materials[37-39] and biological materials.[40-42]

Non-contact Mode

AFM non-contact mode uses a small cantilever oscillation amplitude. The cantilever oscillates at its resonant frequency without direct contact with the surface. The tip is placed close to the surface with a distance of 10-15 nm[31] and the oscillation usually requires a amplitude around 10 nm.[43] The dominant interaction is the attractive van der Waals force, which is shown in Figure 1.3. A schematic of non-contact mode AFM scanning is depicted in Figure 1.4b.

In non-contact mode, the amplitude, phase, or frequency of the cantilever oscillation changes due to the interaction force between the tip and the surface. These changes are monitored through

the laser deflection measured on the quadrant photodiode. The cantilever is returned to its original oscillation set point through a feedback loop. This process is similar to constant force contact mode AFM where the tip is maintained at a fixed distance above the surface. The feedback signal is used to generate the topography of the surface.

Non-contact AFM imaging can be used for soft materials with higher resolution due to the lower repulsive force compared to contact mode imaging. Because the tip is not in contact with the surface, the lateral force while scanning is minimized and both tip and surface damage is minimized. Non-contact mode imaging is widely used for a variety of materials, such as semi-conductors,[44-46] polymers,[47-48] and biological samples.[49-50] In addition, non-contact AFM is a powerful tool for determination of tip-sample interactions.[51] However, under ambient conditions, the surface is usually covered with a contamination layer. In this case, non-contact mode imaging requires a stiff tip and great care since the tip can be trapped by the contamination layer due to the capillary force, which results in significant resolution degradation.[52]

Tapping Mode

Tapping mode AFM is based on an intermediate contact between the probe and surface, which can be envisioned as a combination of contact and non-contact modes. The main interaction forces are both repulsive and attractive forces acting between the tip and the sample, as shown in Figure 1.3. Tapping mode and non-contact mode AFM are known as dynamic AFM techniques. Similar to non-contact mode, the cantilever in tapping mode AFM oscillates close to its resonant frequency. However, the amplitude of oscillation in tapping mode is usually larger than in non-contact mode, which results in the probe periodically touching the surface. A schematic of tapping mode AFM is shown in Figure 1.4c.

In tapping mode AFM, the amplitude of the cantilever oscillation is set to a constant value. When the probe is scanned over the surface, the intermittent tip and surface contact changes the amplitude from the oscillation set-point. Similarly to non-contact mode AFM, the deviation is monitored by the laser deflection, which generates an error signal. Once the error signal is received, the feedback loop adjusts the tip-to-sample distance to compensate for the amplitude change. The error amplitude signal is collected and represents the topography of the surface.

Tapping mode has become a widely used AFM imaging technique because it overcomes the surface contact problems encountered in both contact and non-contact mode AFM. Because the tip touches the surface only occasionally, the contact time between the tip and the surface is minimized, which reduces the lateral force compared to contact mode. The low lateral force reduces surface damage, which facilitates imaging of soft, elastic, and adhesive materials. In comparison to non-contact mode, the probe can penetrate a contamination layer in tapping mode without being trapped because the restoring force of the cantilever can withdraw the probe from the surface. Thus, tapping mode can improve the imaging resolution under ambient conditions. These advances make tapping mode AFM a widely applied technique for a large variety of materials.[27]

1.2.2 Applications of AFM

AFM was widely used in nanoscience and nanotechnology due to its high lateral resolution. Analysis of various samples can be achieved by AFM. The main applications of AFM are surface imaging, mechanical studies, nano-manipulation, and nano-machining, which are introduced in the following sections.

A variety of sample species can be imaged by AFM such as semiconductors,[45, 53] polymers,[54-56] and biological materials.[42, 57-59] Semiconductor surfaces such as silicon materials have been

imaged by AFM at atomic resolution. For example, AFM imaging of Si(111) at atomic resolution was reported from two different groups in 1995.[45, 60] In both cases, AFM imaging was operated under ultrahigh vacuum (UHV) in non-contact mode to avoid surface damage. The Si(111) topography was similar to that obtained with STM imaging; however, fine control of the force gradient applied to the tip was required to avoid image distortion.[45, 60] To improve imaging, a high stiffness (~1800 N/m) cantilever with was developed in 2000.[44] The quartz tuning fork cantilever is more stable in small amplitude oscillation, which improved the image quality and enabled direct observation of subatomic Si(111) features.[53]

AFM has been widely used for imaging of polymer membranes. The diameter of individual membrane pores can be measured by AFM, which allows the determination of the pore size distribution.[56] However, only those pores with openings on the membrane surface can be measured. Therefore, the measured mean pore size may not agree with the results from membrane transport and porosimetry methods.[61-62] In addition, because AFM imaging can measure the height on the surface, it can help monitor the physical change in the roughness of the polymer membrane surface during membrane development. [63]

Biological materials such as DNA and RNA have been imaged by AFM[64-66] and various structures observed under ambient or aqueous conditions.[66-67] For example, AFM imaging was used to observe double helix DNA structures,[68] supercoiled DNA,[69] self-assembling RNA,[70] and chromosome-related structures.[71] The recently developed high-speed AFM has allowed observation of dynamic processes of nucleic acids with an imaging rate over 25 fps.[72] This technique can facilitate direct visualization of dynamic structure changes and dynamic processes of DNA and RNA, which leads to better understanding of nucleic acids operation and function.

AFM can be used to measure surface forces with 10 pN resolution.[73] With the feedback from the interaction forces between tip and surface, mechanical properties such as roughness, hardness, elasticity, and intermolecular forces can be investigated.

Surface height measurement by AFM can be used to determine the roughness of the surface with atomic resolution.[74] AFM has been employed to quantify the roughness of semiconductors,[75-76] metal oxides,[77-78] ceramics,[79-80] polymers,[81-83] and biological materials.[84-85]

In AFM nanoindentation, the probe approaches the surface with a gradient force, which can be used to determine the surface hardness of metals[86] and polymers.[87] The elasticity of biological materials can also be obtained by AFM nanoindentition.[88-89] Single cell penetration was performed on a with an AFM tip,[41] the schematic of which is shown in Figure 1.5. Figure 1.5 a-d illustrates the process of approaching, touching, deforming, and penetrating the cell membrane, respectively, which are also depicted on the left as the points A-D on the force-displacement curve. The

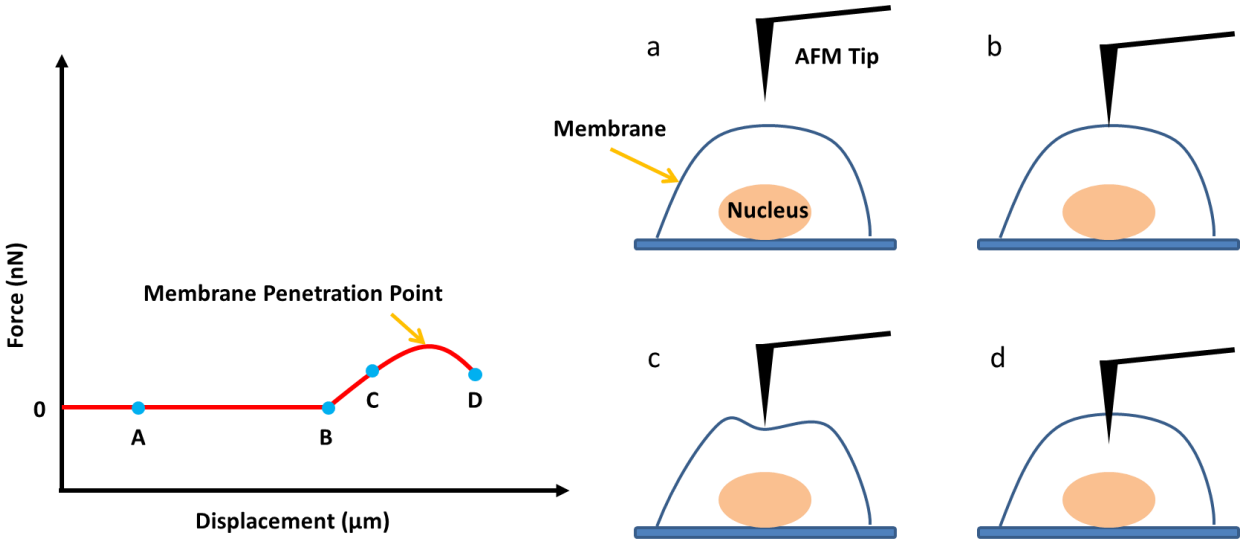

Figure 1.5. AFM tip penetration through a cell membrane

inflection point between points C and D is the point of cell membrane penetration. The corresponding force of this point can be used to determine the elasticity of the cell membrane.

Intermolecular forces of biomolecules, such as proteins and genomic materials, can be measured with contact mode AFM. A biomolecule attached to the AFM probe can be stretched when the cantilever is raised with a gradient force. The force required to overcome intermolecular interactions, such as covalent bonding, hydrogen bonding, and van der Waals interactions, can be determined. Applications include protein unfolding,[90] binding forces in single and double stranded DNA and RNA,[91-93] and measuring binding forces between G-C and A-T base pairs.[94]

With the ability of apply small forces, AFM has become a flexible tool for nanomanipulation such as sample cutting, pushing and pulling, and picking and displacing materials. AFM can be used to cut nanostructures such as biomolecules and for carbon nanofabrication.[95-97] DNA and chromosomes can be cut in a process that involves three steps.[65] First, the biomolecule is imaged in tapping mode. Then, the tip is scanned back and forth in contact mode like a saw. Afterwards, the result is checked by tapping mode imaging. AFM cutting and isolation of single DNA strands with a sharp silicon tip was reported.[98-100] A knife-edged tip was developed to improve the cutting efficiency.[101] AFM cutting of carbon nanotubes with a metal-coated tip was reported.[102-103]

Nanomanipulation has been used for studies of nanoparticles, nanorods, and nanotubes.[104-108] The pushing and pulling process is done in contact mode where small forces are applied. For example, AFM was used to move a 20 nm wide carbon nanotube with a force of 54 nN.[104] AFM was used to push a carbon nanotube to create an electrical contact with two gold electrodes[109] and to assemble gold nanoparticles to form a nanowire.[110] Nanomanipulation has also been performed with biomolecules.[101, 111-112]

Compared to pushing and pulling, nanomanipulation involving picking up nano-objects remains challenging. AFM tips can be used to pick up DNA by adsorption.[113-114] A tweezer-shaped tip was used to grab chromosome pieces by physically clamping them.[115] A two-tip AFM system picking and displacing of nanotubes was developed.[116] A schematic is shown in Figure 1.6. The tips pick up the target like a tweezer with a force of 52 nN.

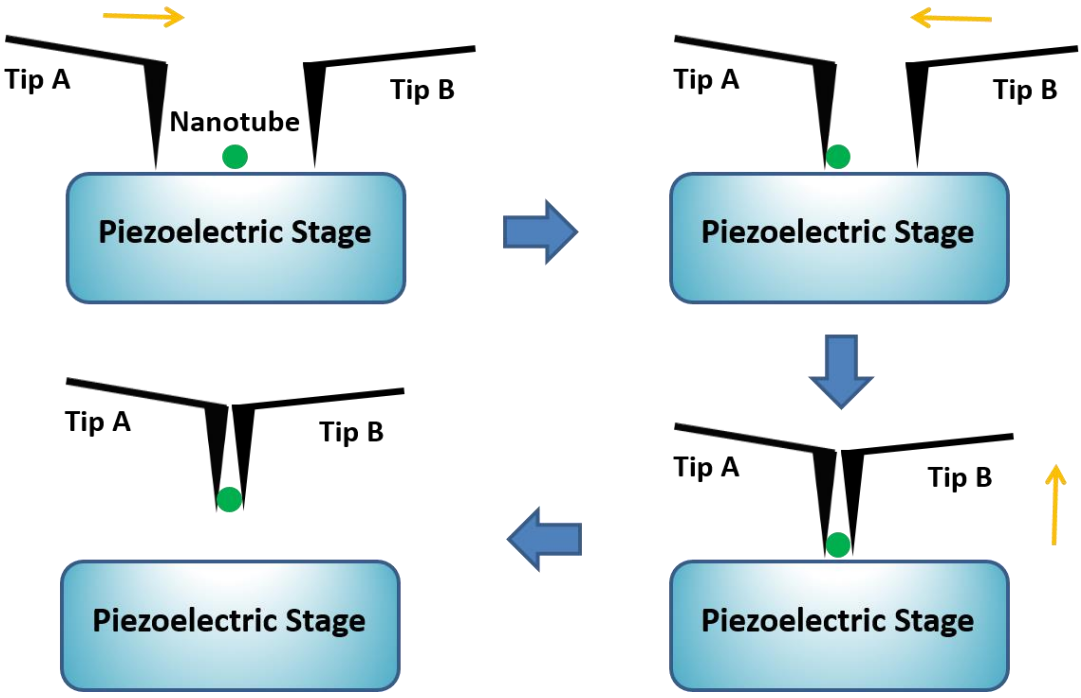

Figure 1.6. Pick nanomanipulation of nanotube by a two-tip AFM nano-tweezers

1.2.3 Challenges

AFM is widely used for imaging, force measurement, and nano fabrication for a variety of samples with a nanometer scale resolution.[64, 117-118] However, with all of these achievements several challenges remain and further improvements are desired.

All measurements and measurement instruments will encounter artifacts. AFM imaging, as an instrument based on the measurement of interaction forces between tip and surface, also has the inevitable challenge of artifacts.

One of the common artifacts found in AFM imaging is produced by the probe during a surface scan. To acquire accurate nanostructure size information, the radius of the probe must be small. An AFM tip may become dull, contaminated, or broken during use,[119] which may generate artifacts. A schematic of various imaging artifacts is shown in Figure 1.7. If the probe becomes blunt during scanning, raised structures will be imaged larger than expected and holes smaller than expected. Spherical nanoparticles with 2 nm diameter have a measured height of 2 nm but a diameter of 10-20 nm when imaged with a blunt probe.[120-121] If the tip breaks during a scan, additional artifacts

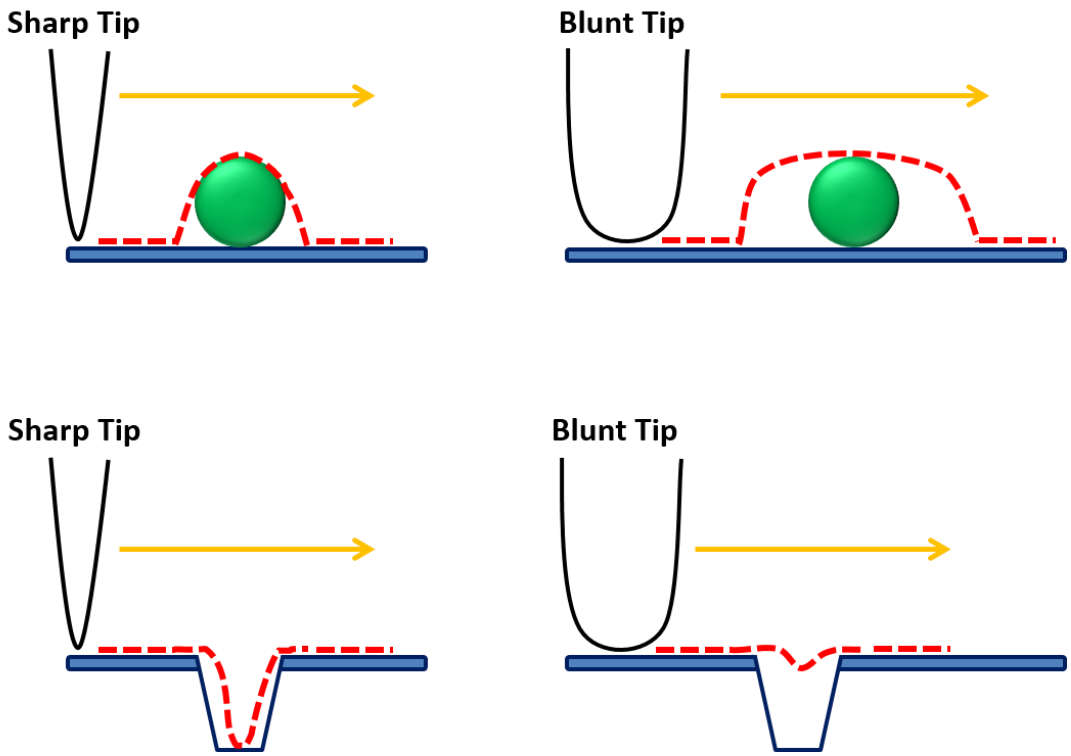

Figure 1.7. AFM imaging artifact due to blunt tips

can be introduced. Broken tips may be spiked or have attached debris producing double or multiple tips, which results in copies of the true structures in the AFM image.[122] In addition, tip contamination from soft materials may degrade the image quality.[123] Thus, to minimize these imaging artifacts, AFM probes with high stiffness and small tip diameter are desired.

Other artifacts can be introduced through environmental vibrational noise such as floor vibration and acoustic vibration. To minimze vibrational noise, instruments can be placed on an isolation table and in an acoustic shileding cabinet.

An additional challenge is 3D imaging. AFM imaging has been used to resolve chemical structures such as pentacene molecules adsorbed on copper with molecular resolution.[124] However, imaging performed in constant height mode has limited planar analysis. A strategy to overcome this limitation is to scan over the same line on the surface multiple times at different constant heights to create the 3D image.[125-127] However, these approaches still lack the precision required for molecular resolution.

Another challenge for AFM imaging is chemical identification.[128] An AFM can measure the phase shift of the cantilever oscillation for phase imaging, which provides limited information on sample composition, adhesion, friction, viscoelasticity, and other factors.[129] However, phase imaging depends on many factors.[130] Other AFM techniques can differentiate samples by their thermal and conductive characteristics.[131-133] However, all these approaches have limited chemical identification ability. To conquer this challenge, AFM has been integrated with other techniques such as spectroscopic methods, which will be discussed in the next section.

1.3 Optical Near-field AFM

The optical near-field effect can be used to couple spectroscopic methods with AFM and to affect surface modification. The resolution limit of far-field optical spectroscopy is set by the diffraction limited spot diameter (D_S) given by:[134]

$$d_{min} = \frac{\lambda}{2\mathrm{NA}} \qquad (1.1)$$

In this equation, λ is the wavelength of the light and NA is the numerical aperture. In order to obtain smaller light beam, a high numerical aperture lens is required and a smallest size of $\sim\lambda/2$ can be approached in conventional optical microscopy.

In 1928, Synge and co-workers developed a theory of illumination through a subwavelength sized aperture placed at a distance smaller than the wavelength ($z \ll \lambda$) to achieve high resolution in the optical near-field below the diffraction limit of the far-field optical system. This field extinguishes rapidly with the increasing distance.[135] This scheme was demonstrated with a scanning probe microscopy metal coated optical fiber with an aperture in the center to reach a resolution of $\lambda/20$[136] and $\lambda/16$[137] in 1984.

When the near-field effect is used with AFM, a technique called scanning near-field optical microscopy (SNOM) is established. There are two modes for SNOM: aperture and apertureless. In aperture SNOM (a-SNOM), the light is directed through a fine pulled optical fiber to illuminate a small area of the surface,[138] while in apertureless SNOM or scattering SNOM (s-SNOM), a sharp metal coated AFM tip acts as an antenna for field enhancement.[139] When the SNOM tip is irradiated while a few nanometers from a surface, an evanescent electric field is formed with the size dependent on the diameter of the aperture (a-SNOM) or the radius of the AFM tip (s-SNOM).

The resolution of SNOM is below the diffraction limit whereas the detection can still be in the far-field. The working schematic of both a-SNOM and s-SNOM is depicted in Figure 1.8.

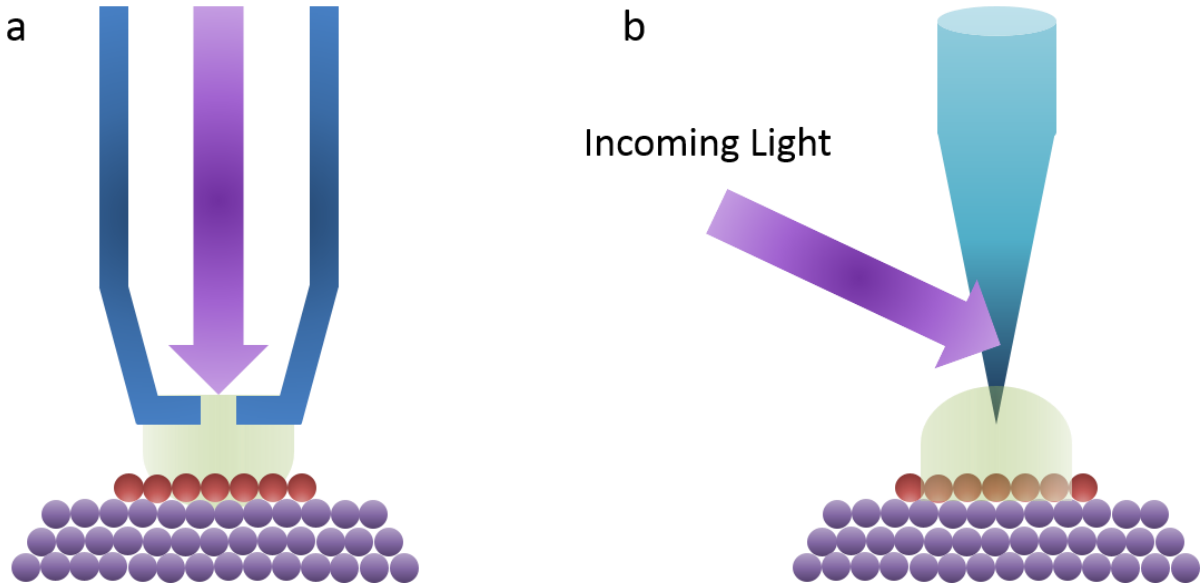

Figure 1.8. Working principle of a) aperture SNOM and b) apertureless SNOM

Several optical spectroscopy techniques have been coupled with near-field AFM to provide high-resolution sample characterization such as Raman, IR, and fluorescence spectroscopy.[140-141] In addition, near-field AFM can be coupled to laser desorption and ablation .[142]

1.3.1 Near-field Spectroscopy

The SNOM or the tip-enhanced techniques has been used for chemical identification.[143-145] Several tip-enhanced spectroscopic approaches have been developed by coupling with Raman spectroscopy,[146-149] infrared,[150-153] and fluorescence[154-155] for material characterization or chemical mapping of a variety of samples of inorganic, polymer, and biological materials.

The idea of coupling Raman spectroscopy to scanning probe microscopy was introduced in 1985.[156] In 2000, tip-enhanced Raman spectroscopy (TERS) was demonstrated.[157-160] TERS is

widely used for chemical identification at molecular resolution.[149] Many efforts have been undertaken to improve the Raman scattering enhancement in the past several decades, which have made TERS a high resolution imaging technique to study the chemical distributions in a sample.[149] TERS is particularly suitable for graphitic materials such as carbon nanotubes and graphene.[161-163] Moreover, TERS is widely used for biological systems such as proteins, collagen, bacterial and viruses, DNA, and RNA.[164-166] For example, TERS has been used for sequencing single stranded RNA.[167]

AFM can also be coupled with fluorescence spectroscopy, which is called tip-enhanced fluorescence (TEF). The enhancement of TEF makes it possible to measure excitation and emission at the nanometer scale. TEF microscopy has been used for one-photon fluorescence images with a resolution below 10 nm[155] and can be coupled with tapping mode AFM to simultaneously obtain the topography and fluorescence mapping of a surface.[168] TEF has been used for chemical identification for a variety of materials such as semiconductors, thin organic films, and carbon nanotubes.[169-171]

IR absorption spectroscopy can be used for chemical identification and structural studies.[172] When AFM is coupled to IR spectroscopy, two techniques with high spatial resolution result. IR scattering scanning near-field microscopy (IR s-SNOM) and AFM-IR.[173] A schematic of these two approaches is depicted in Figure 1.9.

IR s-SNOM is based on the working principle of s-SNOM shown in Figure 1.9a. IR s-SNOM uses an interferometer that measures the amplitude and phase change of the scattered light when the AFM tip is in proximate to the sample within the near-field regime. These changes can be recorded as a function of the refraction index of the local complex, which can be used for chemical identification. The phase and amplitude of the scattered light are not simple functions of absorption,

which means the spectra from IR s-SNOM cannot be directly compared to conventional far-field IR absorption spectra.[173] Another challenge of IR s-SNOM is that the signal is typically much lower than the scattered background.[174] IR s-SNOM has been reported for characterization of various sample species such as small molecule thin films,[175] graphene,[176-177] and biological materials.[178-179]

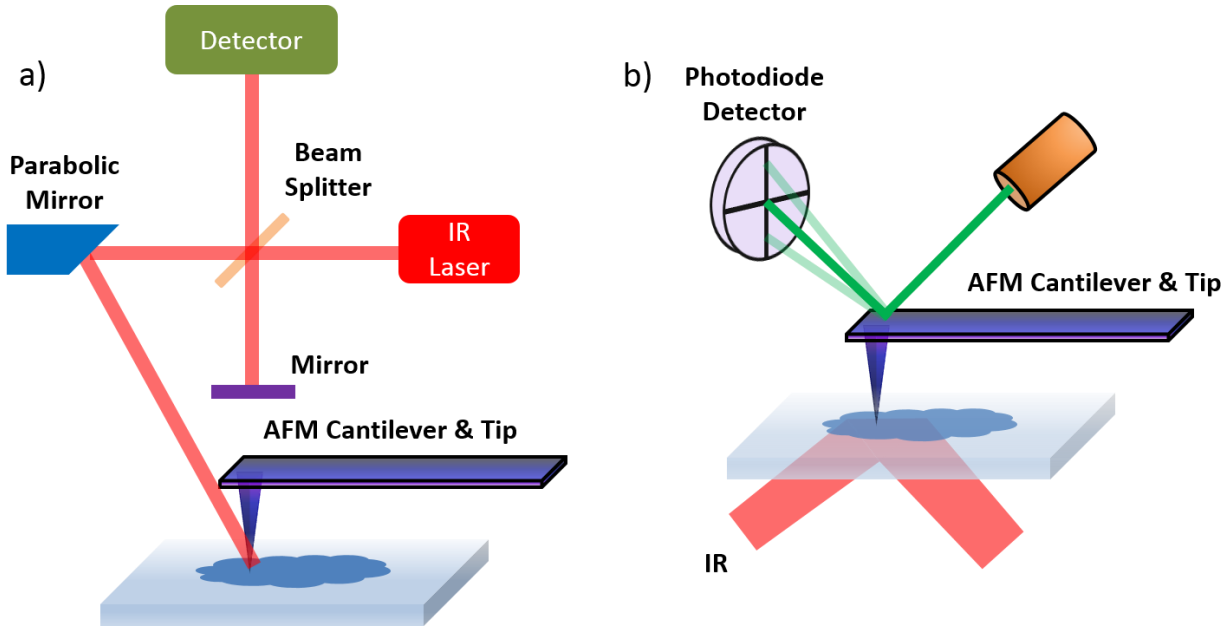

Figure 1.9. Schematics of a) IR s-SNOM and b) AFM-IR

The working principle of AFM-IR is different from IR s-SNOM. In AFM-IR, the AFM cantilever works as a near-field detector for the measurement of the IR absorption of the surface.[151-152] A schematic of AFM-IR is shown in Figure 1.9b. A wavelength tunable pulsed IR laser is used to illuminate sample typically through an optical transparent prism at the total internal reflection angle. The AFM tip is operated in contact with the surface to measure the localized thermal expansion of the surface due to IR absorption, which results in changes to cantilever oscillation.

As discussed in Section 1.2.1, the oscillation change of the cantilever is transduced into laser deflection, which is detected by the photodiode. In most cases, the oscillation amplitude is directly proportional to the amount of light absorbed.[180] Thus, a local IR absorption spectrum can be generated as a function of the cantilever oscillation amplitude change, which is directly comparable to the conventional far-field IR absorption spectra. The spatial resolution of AFM-IR is independent of the incident IR laser beam size, but dependent on the AFM tip radius, which allows sample analysis at the nanometer scale.[151] AFM-IR was recently reported for chemical identification and species mapping of polymers,[152] quantum dots,[181-182] semiconductors,[183] pharmaceuticals,[184-185] and biological materials.[186-187]

1.3.2 Near-field Laser Ablation

Both a-SNOM and s-SNOM can be coupled with pulsed lasers for laser desorption and ablation.[188-189] Laser-induced desorption and ablation can both result in particle removal from surfaces while desorption isolates individual atoms, molecules, or ions.[190] In near-field laser ablation, the laser interaction between the tip and surface may result in sample removal at sub-micrometer resolution, which can be used for nano-fabrication on the surface to create nanometer sized patterns.[191] Near-field laser ablation has been used for sample extraction, which has the potential for further separation and purification of the extracted sample. In addition, the ablated materials can be analyzed by other highly sensitive instruments, which can provide additional chemical and structural information.[192]

Nanomachining

The ability to fabricate structures and devices at the nanometer scale has drawn much attention in the field of nanoscience and nanotechnology. As an alternative to photolithography, AFM near-field laser ablation is capable of surface modification for a variety of samples such as photoresists,

photosensitive polymers, and metals.[191] For example, a 543 nm He-Ne pulsed laser was directed through an aperture SNOM metalized probe to nano-fabricate a feature on a poly(DR1-MMA) photosensitive polymer surface with a resolution of 100 nm.[193] Apertureless AFM near-field laser ablation has been employed for nanomachining of metal surfaces.[194-195] For instance, an 800 nm femtosecond pulsed laser was used for nano-patterning letters and curves on a gold surface at a resolution of 10 nm.[194]

AFM Near-field Ablation with Mass Spectrometry

Mass spectrometry (MS) is one of the most powerful techniques for chemical identification and quantification of complex samples.[196-200] A mass spectrometer is used to determine the mass of charged atoms or molecules based on the mass to charge ratio (*m/z*), which can generate a mass spectrum.[201-202] In addition, fragmentation of ions can be used for structure determination.[203] Sample analysis by mass spectrometry includes extraction, ionization, and detection. If the sample can be extracted and ionized, the mass spectrum from an array of positions can be combined and a mapping of each selected *m/z* can be generated. This approach is called imaging mass spectrometry (IMS) which also provides chemical identification.[204-206] High spatially resolvation sampling and ionization methods are desired to provide more accurate and precise mapping in IMS.[207]

Two of the conventional extraction methods for IMS utilize a focused ion beam or pulsed laser to bombard or irradiate the material. The former approach is called secondary ion mass spectrometry (SIMS), which has sub-micrometer spatial resolution.[208-209] However, SIMS requires high vacuum and is only suitable for atoms, small molecules, or low molecular weight biomolecules (< 1500 Da), since it is a hard ionization method which can fragment large molecules.[210-211] Laser desorption and ablation can sample large biomolecules under ambient

conditions for IMS.[212] However, the laser spot size is diffraction limited. Therefore, ambient high spatial resolution sampling is a challenge for IMS.

Proximal probe thermal desorption under ambient conditions coupled with mass spectrometry analysis was reported in 2010.[213] In this approach, a probe tip with a diameter of 1.6 mm was placed in contact with the surface and heated to 350 ℃ for thermal desorption of analytes from a thin film chromatography plate. The desorbed material was ionized by electrospray (ESI) and atmospheric pressure chemical ionization (APCI) and then sent to the mass spectrometer for identification.[213] An AFM tip was later used for proximal probe thermal desorption of a caffeine thin film. The tip was heated to 350 ℃ and a sampling resolution ~250 nm was achieved.[214] However, since the heated probe temperature is around 350 ℃, the application is limited to relatively low mass species, which can be vaporized by heating.[215]

Near-field laser ablation sampling with a-SNOM under vacuum was first employed with mass spectrometry in 1998.[216] In this approach, acetylcholine and dihydroxybenzoic acid were ablated by a 337 nm nitrogen pulsed laser through a SNOM aperture with a resolution ~1 μm and detected by a time-of-flight (TOF) mass spectrometer. The first use of a-SNOM sampling under ambient conditions coupled with MS analysis was reported in 2001.[217] A 355 nm pulsed laser was directed through an approximately 170 nm diameter aperture of a SNOM probe to ablate a bis(triazenes) thin film in the near-field regime. In this work, the near-field ablation formed a crater of 200 nm diameter with 20 nm in depth on the surface with a volume of 60,000 nm^3 where an estimated 1.7 amol of sample was ejected. A heated 20 cm long capillary with an inner diameter of 20 μm was connected to an electron ionization (EI) source and the other end of the capillary was placed close (< 5 μm) to the SNOM probe to aspirate the ablated material into a quadrupole mass spectrometer. Individual ablated bis(triazenes) were detected by MS.[217] To achieve higher sensitivity, an ion trap

time of flight (IT-TOF) mass spectrometer was employed for the detection of the ablated material.[218-219]

Apertureless AFM near-field laser ablation sampling coupled to mass spectrometry has been demonstrated.[220-221] For example, an AFM was coupled to a quadrupole ion trap mass spectrometer for detection of ablated rhodamine 6G.[221] In this approach, a 532 nm nanosecond pulsed laser was focused onto a gold coated AFM tip, which created craters 150 nm diameter with 3 nm depth on an indium tin oxide (ITO) coated glass coverslip.[189] The ablated material was aspirated into a capillary, which was connected to an ion trap spectrometer. Both the topography acquired by AFM scanning and mass spectrometry chemical imaging of the rhodamine 6G thin film with the spatial resolution of 2 μm were obtained.[221]

Apertureless tip-enhanced laser ablation was coupled with inductively coupled plasma mass spectrometry (ICP-MS) to acquire the elemental distribution of the ablated material.[222-225] A sharp silver needle with a diameter of ~ 150 nm was placed 200 nm above the surface and a 532 nm laser was used for tip-enhanced laser ablation at ~150 nm resolution. Soft samples such as plants and gel were ablated under ambient condition.[223] The ablated material was transferred into an ICP-MS by an argon carrier gas. Further investigations of the tip diameter and tip-to-sample distance were carried out with a gold thin film.[226]

Apertureless tip-enhanced laser ablation sample transfer for off-line matrix assisted laser desorption/ionization (MALDI) MS was demonstrated previously.[207, 227] The off-line sampling approach benefits from additional separation and purification steps for the extracted materials. In this approach, the laser was directed onto a gold coated AFM tip which was ~ 10 nm above the surface. A metal ribbon was placed 300 μm above the surface and 100 μm horizontally from the AFM tip. Lasers with wavelengths of 355 and 532 nm were used for sampling intact small and

large biomolecules with the molecular weights up to ~6000 Da (insulin).[227] In addition, the wavelength of 1064 nm was employed for lipid removal from a rat brain tissue section.[207] The captured material was then dissolved and deposited on a MALDI target with a matrix for MALDI analysis. The transfer efficiency of this approach for rhodamine 6G was 3 %.[227]

1.4 Research Objective

The objective of this research was to develop a tip-enhanced laser ablation system for sample ablation and capture. The mechanism behind this approach was investigated. The application of the TELA system was applied to genomic material ablation and capture.

The instrumentation is described in detail in Chapter 2, which includes two main parts: the AFM and the laser system. The wavelength dependence of the TELA system was evaluated and is discussed in Chapter 3. In this work, the laser wavelength was tuned in the visible and near-IR range to investigate ablation at different wavelengths. Two different sample types were selected for the wavelength dependence studies. The ablation efficiency of each wavelength was evaluated based on the volume of the ablated crater on the surface. Application of the TELA system for sampling DNA with a 532 nm laser is discussed in Chapter 4. The captured DNA was amplified by PCR and nested-PCR.

CHAPTER 2. INSTRUMENTATION

This chapter contains brief description of the instruments used in this research. Tip-enhanced laser ablation is a technique based on the coupling of an AFM instrument with a laser system. The details of the AFM instrument and lasers used in this research are discussed.

2.1 Atomic Force Microscopy

There are two main purposes for the AFM system used in the work described below. First, AFM is used obtain surface images, which helps locate the target of interest for tip-enhanced laser ablation. The other use of the AFM is to place a conductive AFM tip above the surface for laser ablation. AFM working principles are discussed in Chapter 1.

AFM System

The AFM system is a modified Anasys (Santa Barbra, CA, USA) afm+ with a sample stage modified for laser access. A photograph of the AFM system is shown in Figure 2.1 and a photograph of the AFM head and the tip is shown in Figure 2.2. A bright field 10× optical microscope with resolution of approximately 1.5 μm is used to view the AFM cantilever with the probe. A red diode laser is directed onto the back of the cantilever and is reflected onto a quadrant photodiode detector to monitor the cantilever movement. The stage has a motorized XYZ stage for coarse control and a piezoelectric XYZ stage for precise control of scans. The motorized stage has an 8 × 8 mm range and 1 μm resolution whereas the piezoelectric stage has a resolution of 1 nm.

A surface image can be generated using contact, non-contact, and tapping modes discussed in Section 1.2.1 down to 10 nm resolution, which depends on the radius of the AFM tip used for imaging. The system allows acquisition of AFM images with a XY scan range at 100×100 μm and Z measuring range over 7 μm. The AFM system can also perform thermal analysis in nanoTA

mode[228] in which a resistively heated thermal probe is placed in contact with the surface and heated up to approximately 400 ℃. During the temperature ramp, the deflection of the cantilever is monitored to measure the local thermal properties of the material.

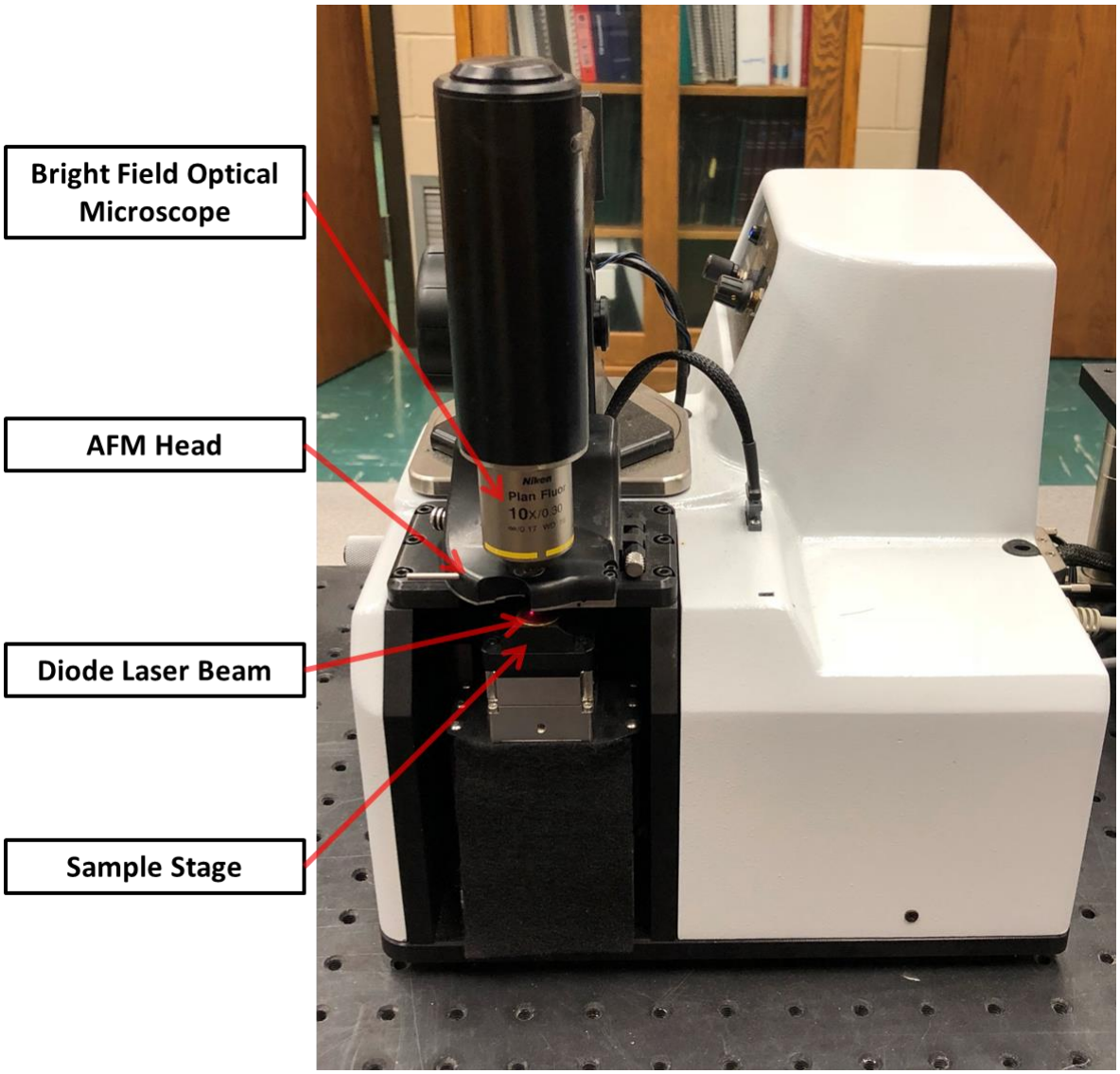

Figure 2.1. Photograph of the AFM system used for tip-enhanced laser ablation

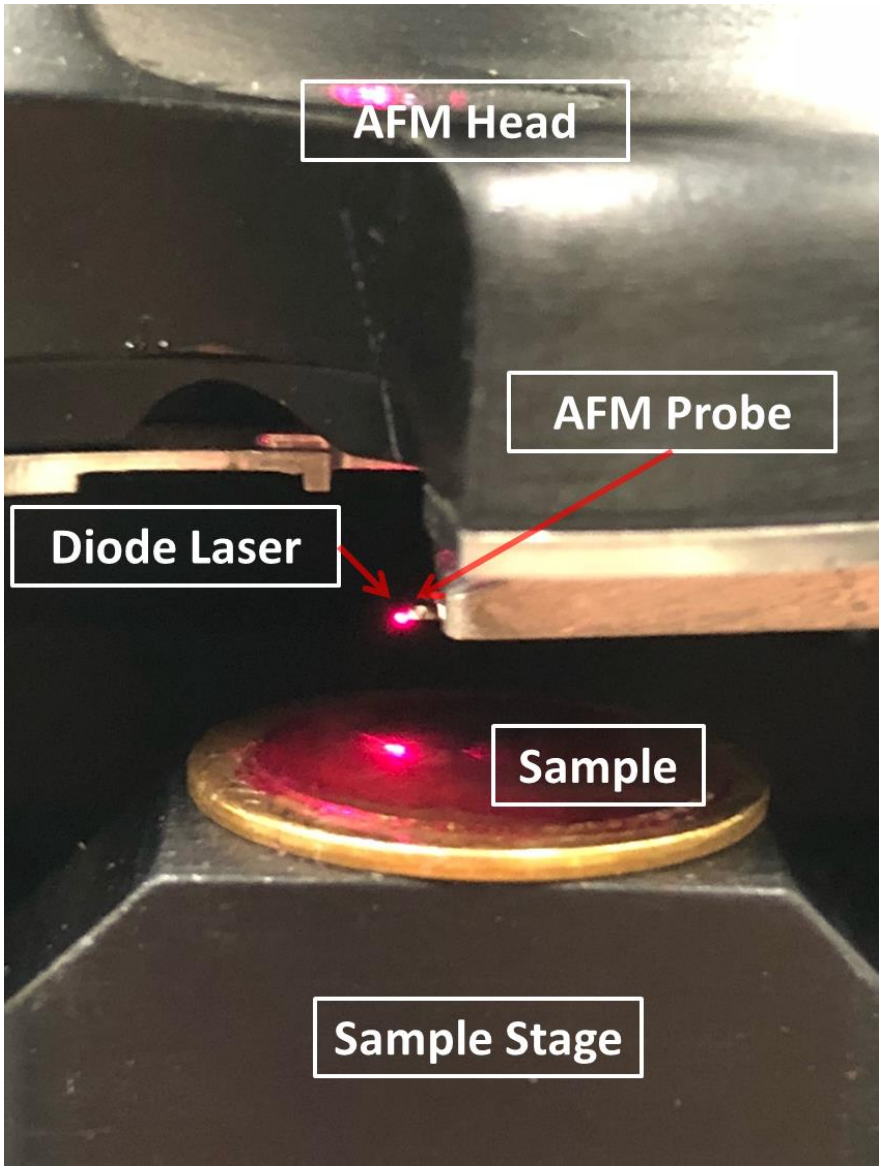

Figure 2.2. Photograph of the AFM head, probe, and sample stage

AFM Probes

The AFM probes used in the research described below are gold-coated silicon tips (ACCESS-NC-GG, Applied Nanostructures, Mountain View, CA, USA). These probes are manufactured from low resistivity (0.010-0.025 Ω/cm) n-type antimony doped single crystal silicon in the shape

of a triangular pyramid. The probe cantilever is 140 µm long, 50 µm wide, and 5 µm thick. The configuration of the tip is depicted in Figure 2.3. The tips are between 14 to 16 µm tall and the apex half-cone angle of the tip is 15^0. The center axis of the probe is tilted tip at an angle of 28^0 with respect to the cantilever normal axis. This design allows direct optical line of sight to the tip for laser irradiation. The silicon has a radius of 6 nm and a 35 nm thick gold vapor deposition coating gives a tip radius of 40 nm. The spring constant and resonant frequency are 60 N/m and 300 kHz, respectively.

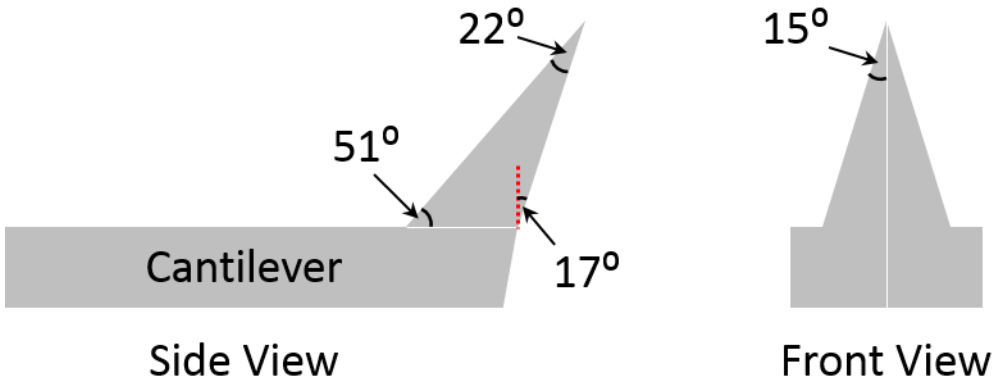

Figure 2.3. Configurations of the AFM tip

2.2 Lasers

Nd:YAG Laser

The Minilite I laser (Continuum, San Jose, CA, USA) is a 532 nm frequency doubled Nd:YAG laser and the configuration is depicted in Figure 2.4. This laser is pulsed with a width of 5 ns. The maximum energy output of the laser is 100 mJ with a repetition rate up to 15 Hz.

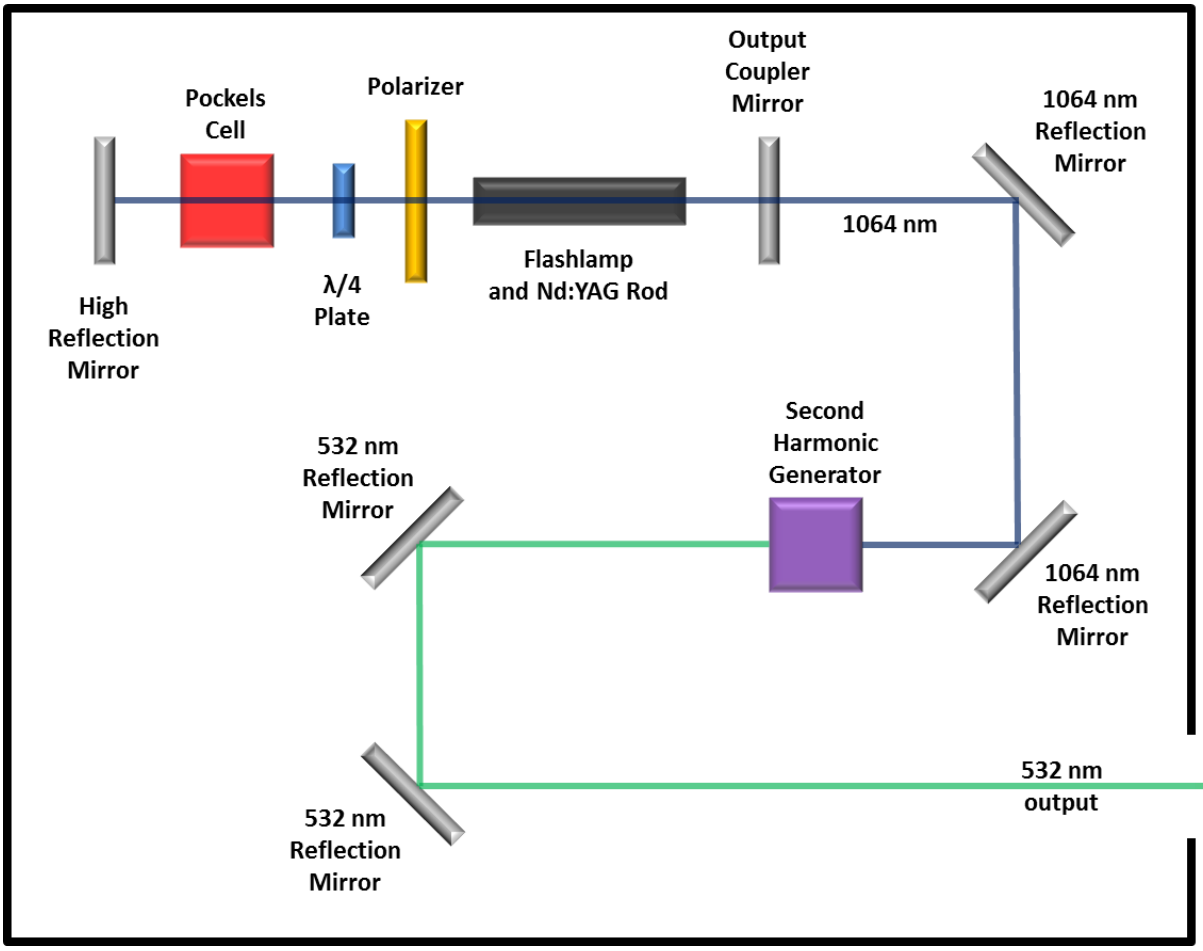

Figure 2.4. Schematic of the Nd:YAG laser

Optical Parametric Oscillator Laser

The optical parametric oscillator (OPO) laser system is a wavelength tunable system (Opolette HE 335 LD, OPOTEK, Carlsbad, CA, USA). The pump laser is a 355 nm Nd:YAG third harmonic laser. The non-linear crystal used to generate the signal and idler output is made of the barium boron oxide (BBO). The BBO crystal is mounted on a motorized stage, which is controlled by software for rotation. Both signal (410-710 nm) and idler (710-2400 nm) wavelengths can be used as the output of the OPO. This system has a wavelength tuning range of 410-2400 nm, which covers part of the visible and near-IR range with an accuracy of 1 nm. The pulse width of the

output laser is 7 ns, and the maximum repetition rate is 20 Hz. The wavelength tuning curve is shown in Figure 2.5 and the maximum output energy is 9.4 mJ at 530 nm.

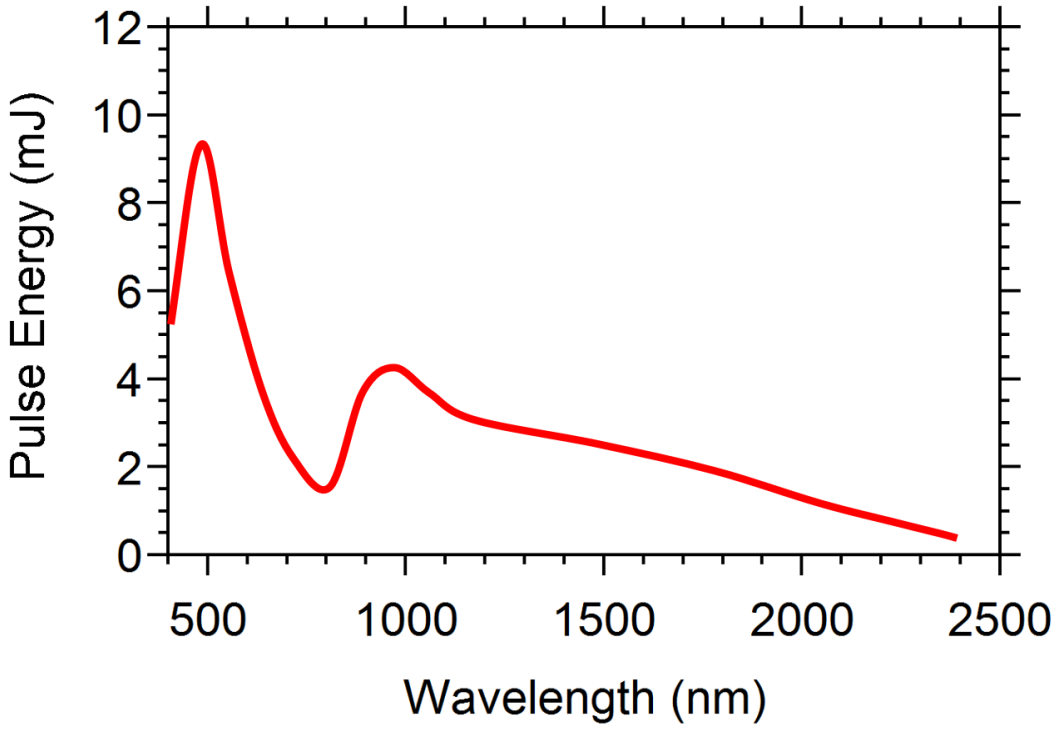

Figure 2.5. OPO tuning curve

2.3 Tip-enhanced Laser Ablation

A photograph of the tip-enhanced laser ablation configuration is shown in Figure 2.6. The system is mounted on a vibration isolation table (TMC, Peabody, MA, USA), minimizes AFM imaging artifacts caused by vibrational noise. The laser beam is steered by two silver-coated broadband mirrors and focused 1 cm beyond the AFM tip using a 25 cm CaF_2 lens. The laser is directed at an angle of 10º with respect to the table surface and 45º to the axis of the cantilever.

The polarization of the laser was adjusted using a half wave plate. The laser output was attenuated with a Glan-Thompson polarizing prism.

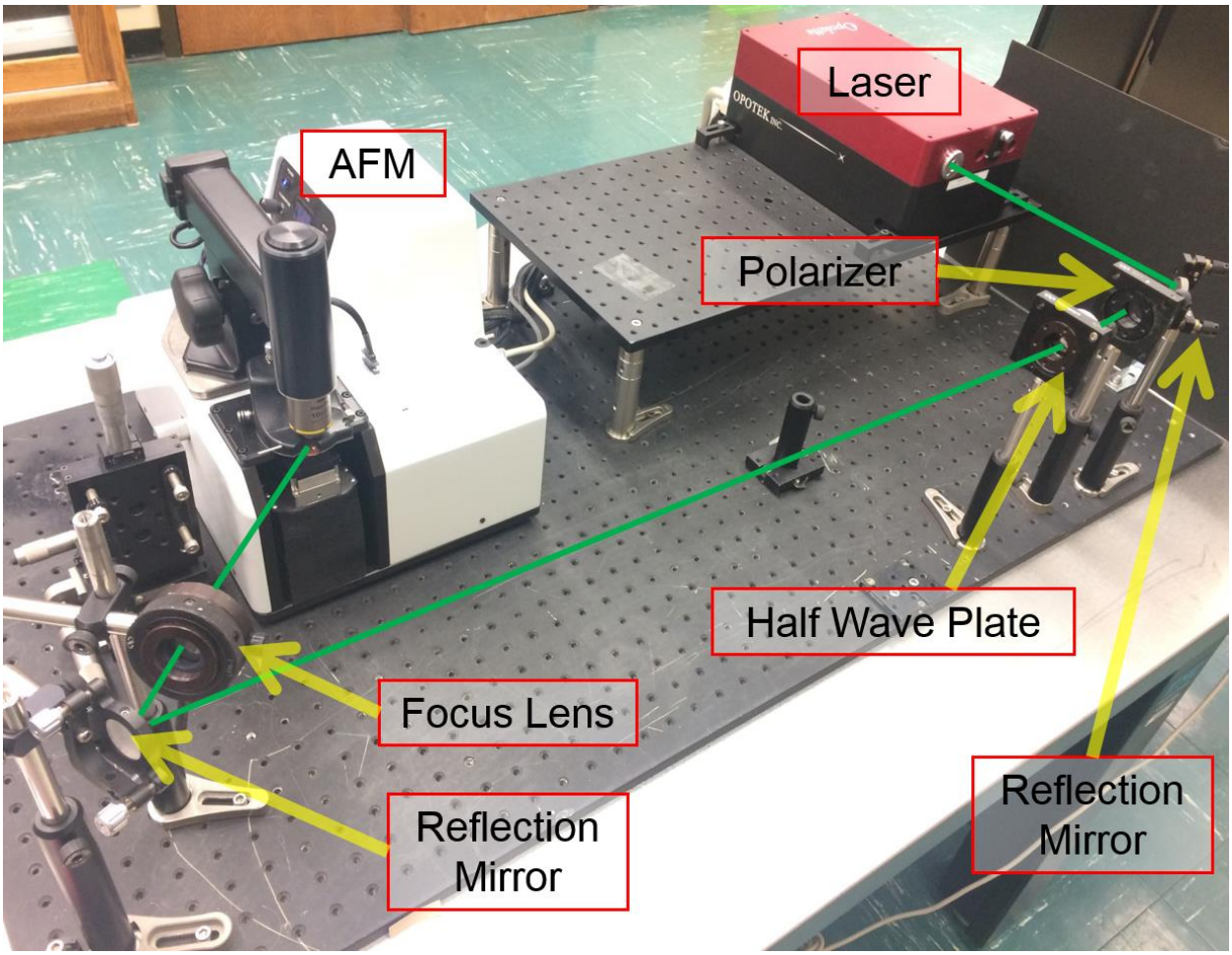

Figure 2.6. Photograph of the tip-enhanced laser ablation system

Samples used in the experiments were prepared by deposition on a glass cover slip, which was affixed to a 1.5 cm diameter 2 mm thick round metal plate with a double-sided tape. The plate was mounted on the AFM sample stage for imaging and ablation. The AFM images reported below were obtained in tapping mode. For ablation, the target of interest was selected and the tip was brought above the target ~ 10 nm. The AFM was operated in tapping mode during laser ablation.

An interval of 1 s between laser shots was used to irradiate the tip. Craters formed on the surface by tip-enhanced laser ablation were imaged in AFM tapping mode. For capture of the ablated material, a 300 μm wide silver ribbon was placed 300 μm above the surface and 100 μm away from the AFM cantilever.

CHAPTER 3. MECHANISTIC STUDIES OF TIP-ENHANCED LASER ABLATION*

The role of laser wavelength in AFM-TELA was studied and is discussed in this chapter. The wavelength tunable OPO was used to irradiate a gold-coated silicon AFM probe held 15 nm above the surfaces of anthracene, rhodamine B, methylene blue, and IR 797 which have different maximal optical absorption. The absorption of laser energy by the tip at 532 nm is sufficiently high to result in melting of the gold coating and increases the diameter of the tip from 100 nm to approximately 1 μm. The ablation crater volume was measured and found to have a maximum at 500 nm and an approximately linear drop to 800 nm. Craters could not be produced in the near-IR range of 800-1200 nm. The crater size is not dependent on the optical absorption of the surface and the mechanism of ablation is postulated to be the result of a ballistic effect or direct thermal transfer through the tip in contact with the surface.

3.1 Introduction

The combination of AFM with atomic and molecular spectroscopy results in a powerful tool for chemical analysis.[144-145, 229] Both aperture and apertureless SNOM were developed for chemical identification with high spatial resolution due to the near-field effect.[141, 230-232] Both aperture and apertureless SNOM are used for fluorescence,[166] TERS,[146, 166, 233] IR[151, 173, 234] and electroluminescence spectroscopy.[235] These tip-enhanced spectroscopy methods bring the size scale for chemical analysis into the range below 100 nm.

---

* Some portions of the work reported in this chapter previously appeared as Cao. F.; Donnarumma, F.; Murray, K. K., Wavelength Dependent Atomic Force Microscope Tip-enhanced Laser Ablation, published in the *Applied Surface Science*.[261] Reprinted by permission of Elsevier.

Tip enhancement can also be used for chemical sampling and material modification below 100 nm.[236] Laser ablation can be accomplished using aperture systems to couple nanosecond,[237-239] picosecond,[217] or femtosecond[240-243] pulse width lasers. Apertureless laser ablation has been demonstrated with nanosecond lasers.[189, 227, 244] The ablated material was characterized using mass spectrometry[207, 217-218, 245-246] as well as optical emission spectroscopy.[247-248]

The mechanism of near-field laser ablation may result from thermal expansion of the tip, ballistic ablation, or photothermal ablation.[142, 238-239] Evidence for thermal expansion of an aperture tip leading to surface indentations has not been found.[238] Direct heat transfer from the tip to the surface at atmospheric pressure is believed to be inefficient; a more probable mechanism is ballistic ablation in which molecules adsorbed on the tip or atoms from the tip coating are ejected and impinge on the sample causing sputtering of the material below. Ballistic heating was postulated as the mechanism of material removal from van der Waals solids with relatively low enthalpy of sublimation such as anthracene.[239] Ablation of materials with higher sublimation enthalpy such as the chloride salt rhodamine dye is more consistent with a photothermal mechanism in which the laser energy is absorbed by the substrate and converted to vibrational energy that leads to ablation.[238] With the photothermal mechanism, the wavelength dependence of the ablation tracks the molecular absorption of the substrate thin film.

In this chapter, a study of the wavelength dependence of apertureless tip-enhanced laser ablation of anthracene and three organic dyes is presented. The efficiency of laser ablation was studied using the volume and size of craters produced on surfaces with the optical parametric oscillator (OPO) laser, which allowed wavelength tuning in the 450-1200 nm range, covering the visible and near-infrared spectrum. The results were used to elucidate the mechanism of tip-enhanced laser ablation.

3.2 Experimental

The tip-enhanced laser ablation system configuration described in Chapter 2 was used for the experiments described in this section. The AFM was operated in tapping mode both for imaging as well as tip-enhanced laser ablation. The amplitude sensitivity of the tip was 6-7 nm/V and an amplitude set point of 1 V was selected to keep the tip oscillating between 0 and 15 nm from the surface during ablation. A Glan-Thompson polarizer was used to adjust the laser energy. The energy was set to 300 μJ/pulse for anthracene, 100 μJ/pulse for rhodamine B, and 150 μJ/pulse for methylene blue and IR 797 organic dyes ablation. Each crater was obtained from 3 laser shots with a 1 s delay between each shot. Three dimensional images were constructed from the AFM data using custom software written in LabVIEW (National Instruments, Austin, TX, USA), which was also used to calculate crater and rim volumes.

The AFM probes were imaged by scanning electron microscopy (Quanta 3D FEG FIG/SEM, FEI, Hillsboro, Oregon, USA) and energy dispersive X-ray (EDX) spectroscopy was used to determine the elemental composition of the probe surface.

Thin films of pure compounds were used as test surfaces for the tip-enhanced laser ablation. Anthracene (99%; Sigma Aldrich, St. Louis, MO, USA) was dissolved in dichloromethane (99.9%; Sigma Aldrich) at a concentration of 1 mg/mL. Rhodamine B (Fluka, St. Louis, MO, USA), methylene blue (Sigma-Aldrich), and IR 797 chloride (80 % dye content, Sigma-Aldrich) were prepared in methanol (LC-MS grade, Sigma-Aldrich) at a concentration of 1 mg/mL. The films were formed by depositing 3 μL of the solution on a glass cover slip and allowing the solvent to evaporate. The thickness of the films was estimated to be around 1 μm. Absorption spectra of each organic dye solution at a concentration of 10 μg/mL in methanol were obtained with an ultraviolet-

visible spectrophotometer (Cary 50 Bio, Varian, Palo Alto, CA, USA) at a scanning range from 400 to 1100 nm using a scanning speed of 600 nm/min.

3.3 Anthracene Ablation

The effect of laser irradiation on the AFM tip was evaluated using scanning electron microscopy (SEM). Figure 3.1 shows a SEM image of an AFM tip before and after laser irradiation

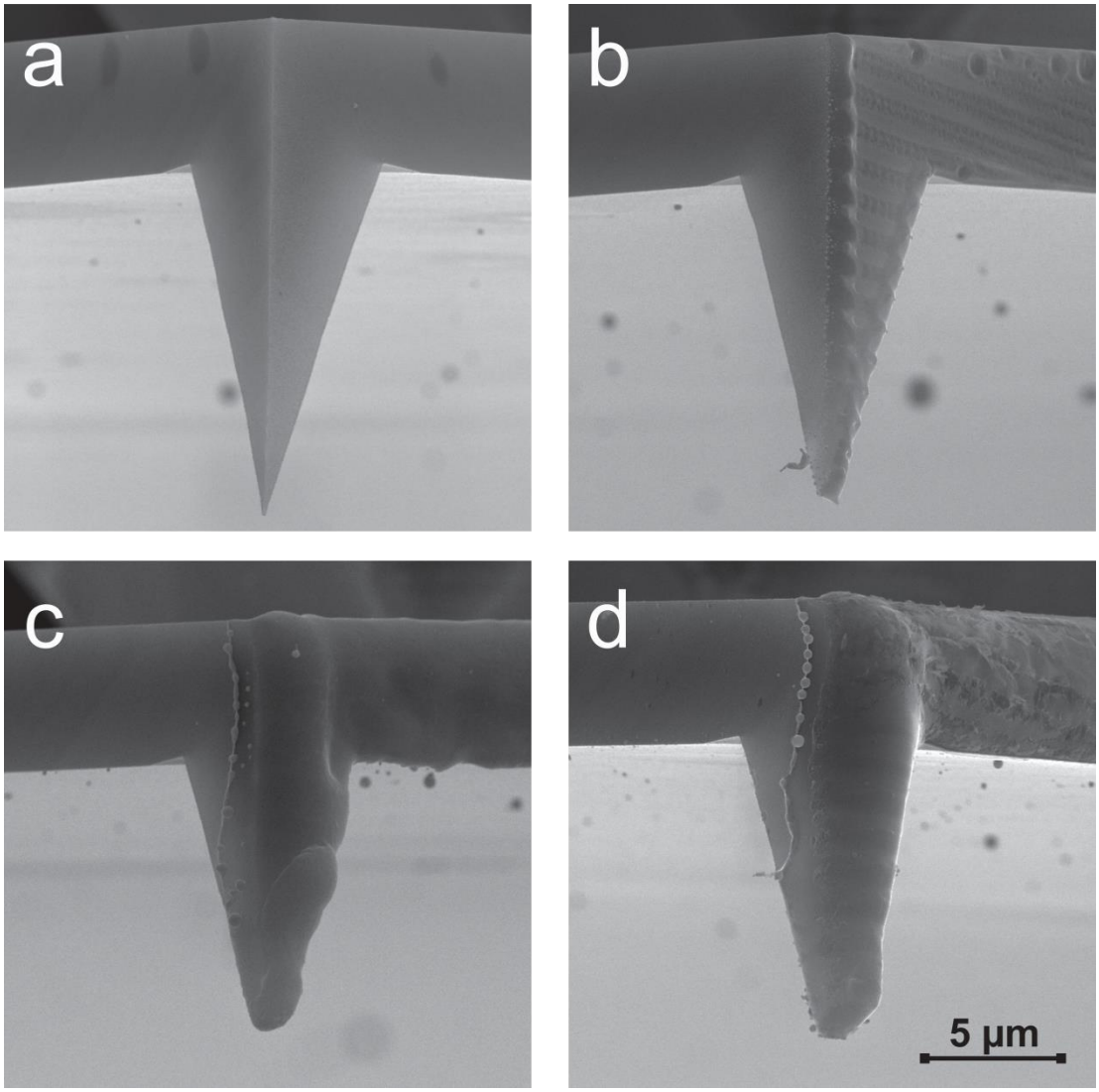

Figure 3.1. Atomic force microscope tips imaged by scanning electron microscopy a) new tip, b) tip after one laser shot, c) ten laser shots, and c) 1000 laser shots.

at a wavelength of 532 nm and fluence of 4 kJ/m^2. The diameter of a tip at its apex prior to irradiation is around 100 nm (Figure 3.1a), which is consistent with the manufacturer specified diameter of 80-90 nm. The images in Figure 3.1b-d depict a probe tip irradiated with a single laser shot, 10 shots, and 1000 laser shots, respectively. The tips often fracture and are unusable after several thousand laser shots. In these images, the surface of the tip that was exposed to the laser is on the right and this surface appears to be modified to the greatest extent by the laser. After a single laser shot, the tip diameter was 800 nm at its apex (Figure 3.1b) and after 10 laser shots, the diameter was approximately 1 µm (Figure 3.1c). Additional laser shots did not significantly increase the diameter; for example, after 1000 shots (Figure 3.1d) the tip diameter remained approximately 1 µm. There are some surface ripples observed on some of the irradiated tips, for example in Figure 3.1b, that appear to be laser induced periodic surface structures.[249] Such structures are often observed on surfaces irradiated with ps or fs laser pulses, but can also be observed with ns laser pulses.[250] The structures observed in Figure 3.1b have a spacing of approximately 500 nm and are oriented perpendicular to the laser polarization, suggesting that these are near-subwavelength ripples.[251]

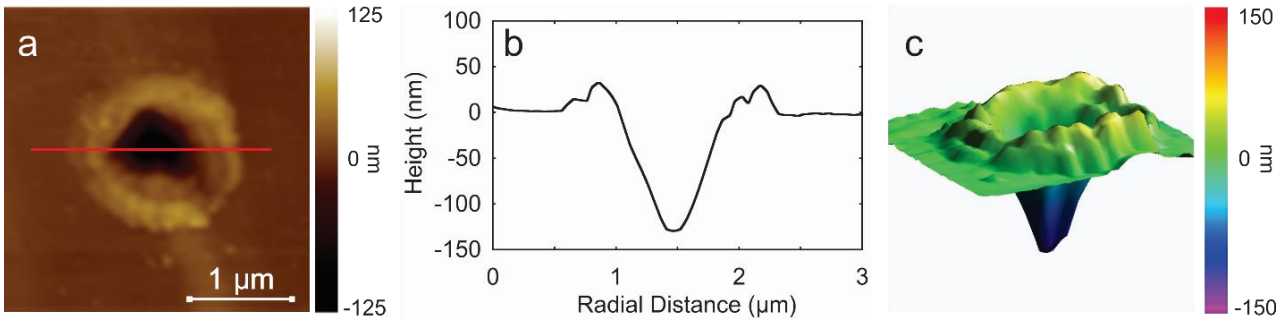

Figure 3.2. Laser ablation crater in anthracene obtained at 532 nm wavelength a) AFM image, b) profile, and c) three-dimensional plot.

An AFM image and corresponding contour plots for a representative crater formed on anthracene by tip-enhanced laser ablation are shown in Figure 3.2. The laser wavelength was 532 nm and the fluence was 4 kJ/m^2. Figure 3.2a depicts an AFM image obtained in tapping mode using a tip that was irradiated with several hundred laser shots and therefore is expected to have a tip diameter of approximately 1 μm. The depth profile of the crater along the red line shown in Figure 3.2a is depicted in Figure 3.2b and a 3-D representation of the crater is shown in Figure 3.2c. This crater has a measured depth of 130 nm, diameter of approximately 1 μm, and a somewhat triangular shape that may reflect the triangular pyramid shape of the AFM tip. There is a rim around the crater that is 20 to 40 nm higher than the surrounding surface and may have been formed by melting and resolidification of the anthracene.

The rim material could be removed from the crater after repeated AFM scans in tapping mode. Figure 3.3 depicts tapping mode AFM images of an anthracene crater formed by 3 laser shots at

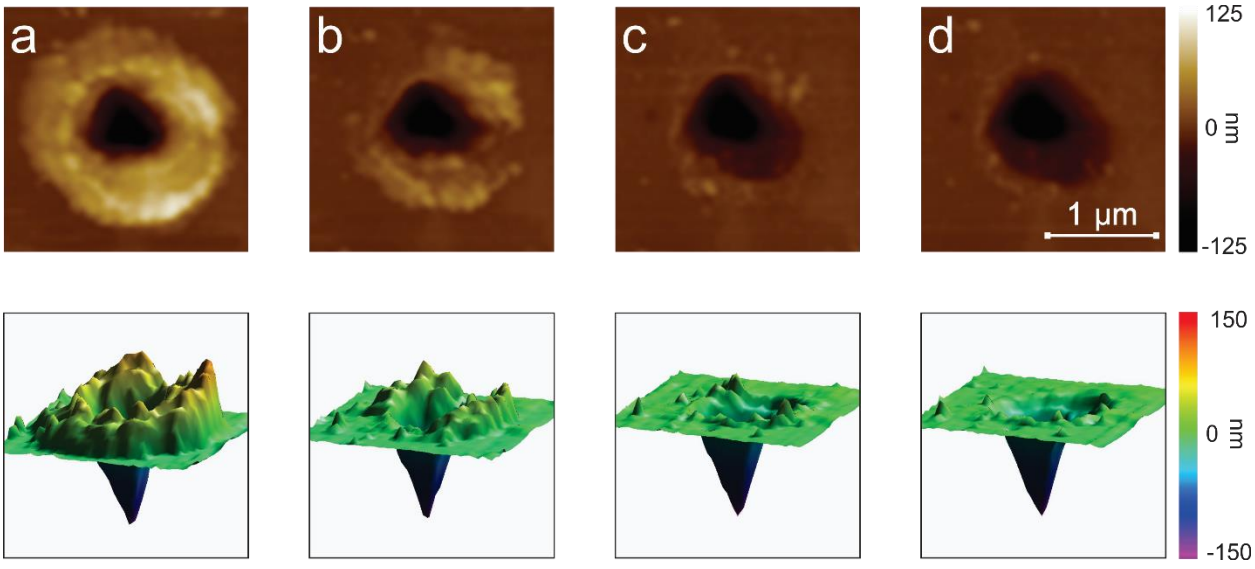

Figure 3.3. AFM images of laser ablation craters in anthracene at 532 nm: a) first scan, b) second scan c) third scan, d) fourth scan.

532 nm and 4 kJ/m^2 fluence. Figure 3.3a was obtained directly after ablation and Figures 3.3b–d depict the second, third, and fourth scans of the same crater. In Figure 3.3a, the volume of the crater below the level of the surrounding material was 0.03 μm^3 whereas the volume of the rim was 0.1 μm^3, three times larger than the crater. The large volume of the crater rim, combined with the apparent ease with which it is removed, suggests that the rim material is less dense than the underlying film. An AFM phase image of the crater (Figure 3.4) is consistent with softer and less dense rim material. Subsequent scans of the crater led to measured crater volumes of 0.03, 0.04, and 0.05 μm^3 and rim volumes of 0.02, 0.003, and 0.001 μm^3 (Figures 3.3b–d). The measured crater depth with respect to the surrounding material was 140 nm after the first scan, 150 nm in the second scan, and 160 nm in the third and fourth scans. Similar micrometer scale tip-enhanced patterning was observed on silicon surfaces irradiated with an infrared fiber laser and was attributed to laser-induced thermal oxidation.[252] In consideration of the effect described above, the

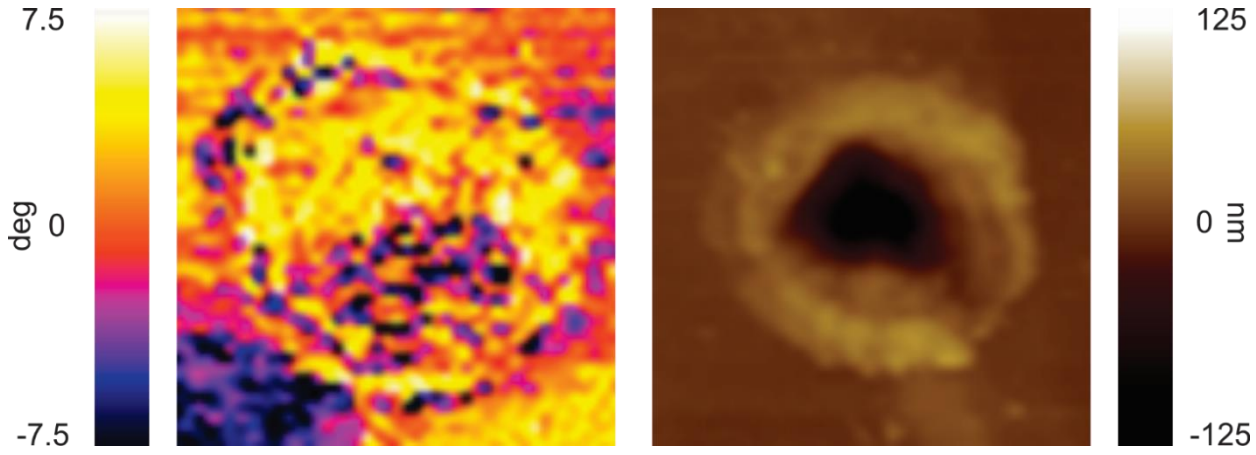

Figure 3.4. Phase (left) and topography (right) image of a tip-enhanced laser ablated anthracene crater.

crater volume measurements for all the remaining experiments were obtained from the third AFM scan images.

Ablation craters on anthracene thin films were obtained with a range of wavelengths in the visible and near-IR region. Figure 3.5 shows AFM images of craters in an anthracene thin film obtained at wavelengths between 450 and 700 nm in steps of 50 nm. The corresponding contour plot is displayed below the AFM image. The laser fluence was 4 kJ/m^2 at all wavelengths. The crater volume corresponding to the images shown in Figure 3.5 is plotted as a function of wavelength in Figure 3.6. The crater volume produced by a specific AFM probe at a particular wavelength is reproducible, but there is a variation from probe to probe. However, in all cases, the maximum crater volume was observed near 500 nm wavelength and crater formation was found to be relatively efficient in the wavelength range from 450 to 600 nm. Craters were not observed between 800 and 1200 nm. Figure 3.7 shows a plot of crater volume as function of wavelength for a different AFM tip. The crater volume is smaller than that depicted in Figure 3.5, but the trend is similar.

Previous studies have suggested that the dominant mechanisms for aperture tip-enhanced ablation are either photothermal or ballistic heating.[238] The wavelength dependence of the crater size depicted in Figure 3.6 is not consistent with a photothermal mechanism in which the tip enhances photon absorption by the substrate. The absorption maximum of anthracene is below 250 nm in the UV; the absorption in the 400 to 1200 nm of the visible and near IR is negligible.[253] The trend in Figure 3-6 is more consistent with the ballistic heating mechanism that was suggested for aperture mode desorption of anthracene.[239] Here, the gold from the tip or adsorbed water or other compounds is desorbed from the laser-heated tip and impinges on the anthracene surface to eject secondary material. With the apertureless tip operated in tapping mode there is an additional

possibility of heating the tip and melting by contact with the anthracene film. The tip is heated to the melting point of gold, which is around 1200 K for gold nanoparticles,[254] thus the tip may transfer thermal energy directly to the anthracene by contact. There also may be an additional contribution through convective heat transfer through the air.[255]

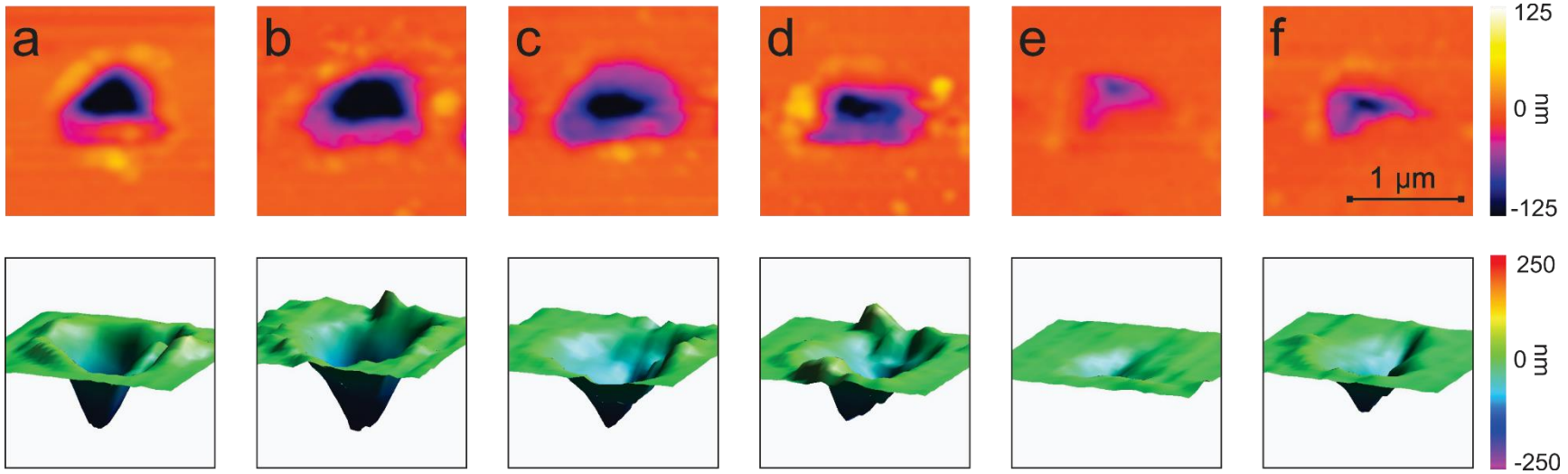

Figure 3.5. AFM topography and 3-D view of anthracene craters with laser wavelength at a) 450, b) 500, c) 550, d) 600, e) 650, and f) 700 nm

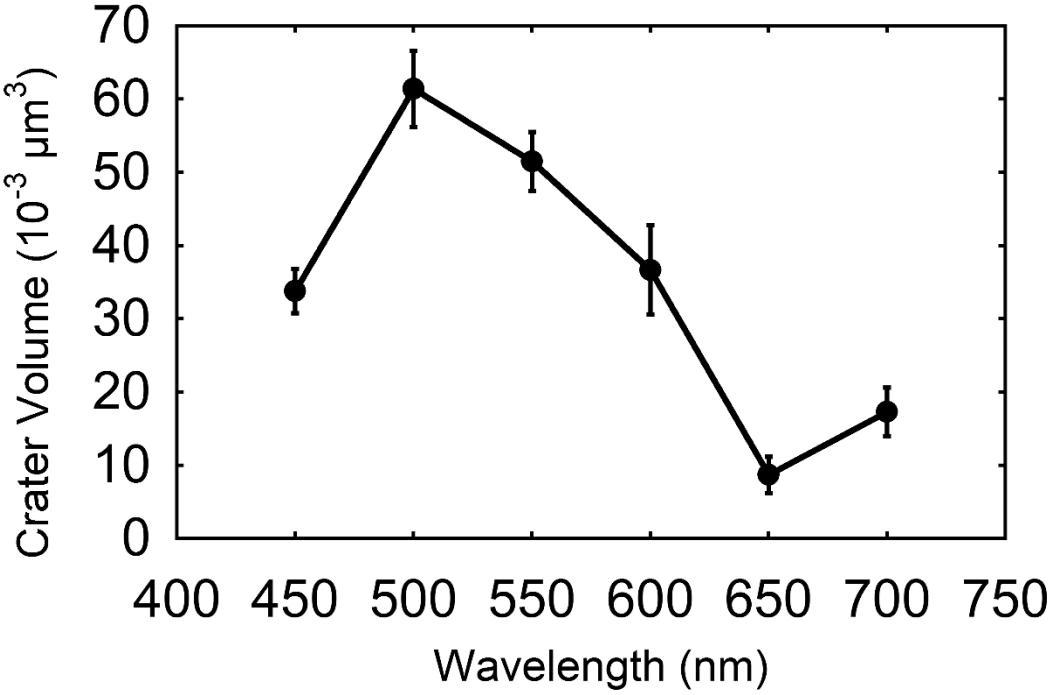

Figure 3.6. Laser ablation crater volume in anthracene as a function of wavelength.

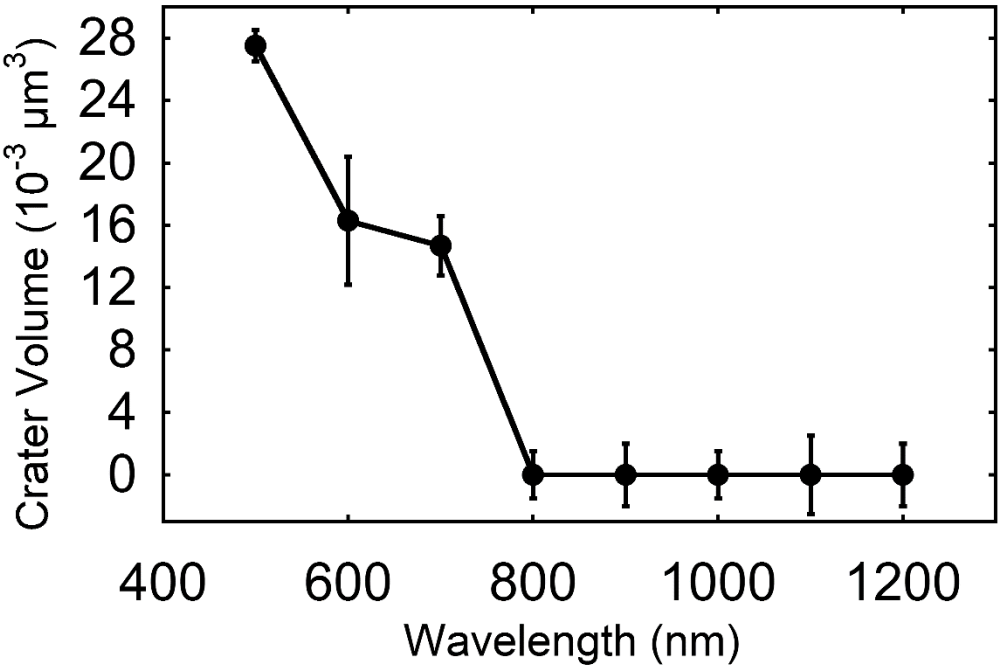

Figure 3.7. Anthracene crater volume plotted against wavelength from 500 nm to 1200 nm with a 100 nm step.

All of these heat transfer mechanisms are consistent with the formation of the crater rim on the anthracene surface. The absorption of gold in the visible and near-IR results from the plasmon resonance and is dependent on the size and shape of the AFM tip as well as the dielectric properties of surrounding medium.[256] For gold thin film, the plasmon resonance is strongly related to the thickness of the film.[257] For gold coating on silica nanoparticles, it was found that the resonance is dependent on the fractional surface coverage and tends to shift to the red on increased fractional coating.[258] The wavelength response that we observe is consistent with absorption of the laser energy by the thin gold film on the AFM tip and suggests that strong enhancement may be achievable with a thinner or even partial coating of gold on the tip.

The anthracene crater appears to be formed by laser heating of the tip followed by ballistic heat transfer and/or heating, either by contact of the tip with the surface or by convective heat transfer. The absorption of laser energy by the tip is consistent with plasmon absorption of the thin film of gold on the AFM tip. However, for aperture SNOM near-field ablation of rhodamine B, the mechanism was suggested to be an optical absorption of the material.[238] Therefore, three organic dyes was used in the work described below for further exploration of the mechanism of TELA.

3.4 Organic Dye Ablation

Tip-enhanced laser ablation of IR 797 chloride, rhodamine B, and methylene blue thin films was evaluated in the wavelength range from visible to near-IR. The surface was imaged in tapping mode in order to select a flat surface for tip-enhanced laser ablation. The laser energy was adjusted to avoid far-field ablation. Topographic and 3-D images of IR 797, rhodamine B, and methylene blue craters are depicted in Figure 3.8, 3.9, and 3.10, respectively. Around the craters from all the samples a rim was observed, which is believed to be formed by melting and resolidification or

laser induced surface foaming.[259-260] At wavelengths from 450 to 600 nm, the average height of the rim for IR 797, rhodamine B, and methylene blue was 105 nm, 60 nm, and 80 nm, respectively. The rim height difference may be due to the different melting points of IR 797 (MP ~120 ℃), rhodamine B (MP ~210 ℃), and methylene blue (MP ~190 ℃), with a lower melting point resulting in more melted material. A ripple structure was observed at wavelengths of 450-550 nm for rhodamine B, for example at the up-right corner of the crater shown in Figure 3.9. Larger scale AFM images of this structure are shown in Figure 3.11 and were observed over an area of 20 × 20 μm. The distance between the features was approximately 300 nm. This structure was only observed on rhodamine B film at wavelengths of 450-550 nm.

The volume of the organic dye craters was obtained to evaluate the tip-enhanced laser ablation efficiency. The wavelength was tuned from 450 to 800 with 50 nm steps. The mean depth and volume of each crater is shown in Table 3.1. In all cases, no craters were observed in the near-IR wavelength region whereas in the visible wavelength range, the maximum crater volume was observed near 500 nm wavelength and crater formation was found to be relatively efficient from 450 to 550 nm.

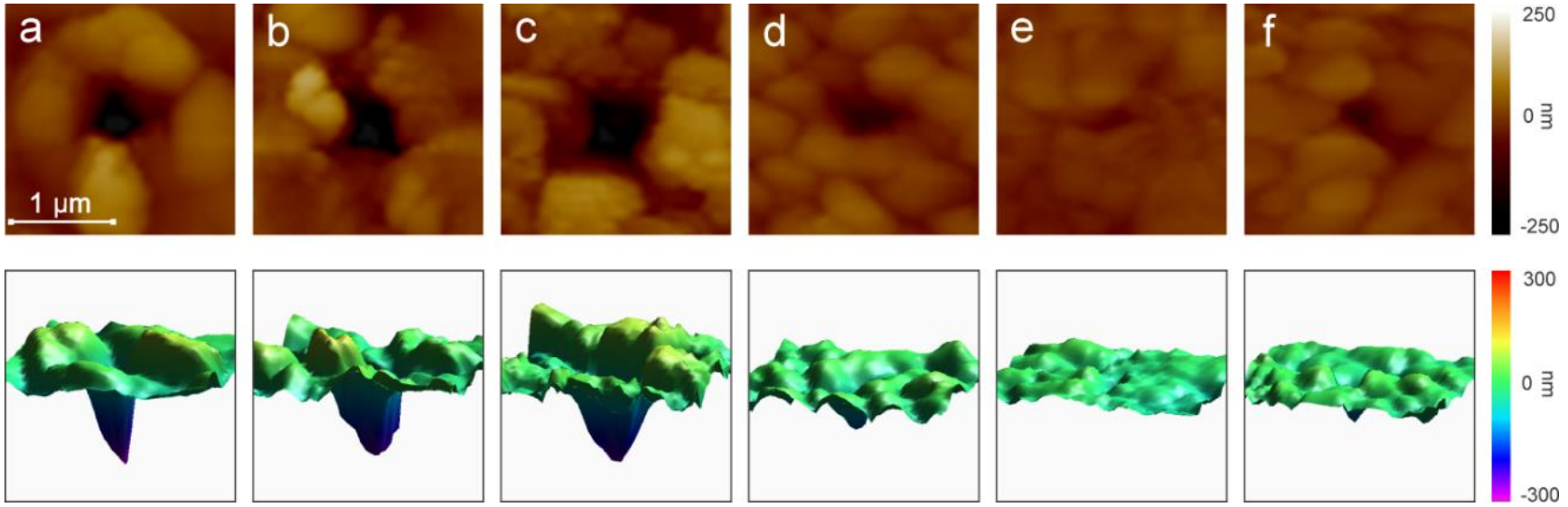

Figure 3.8. AFM topography and 3-D view of IR 797 craters with laser wavelength at a) 450, b) 500, c) 550, d) 600, e) 650, and f) 700 nm.

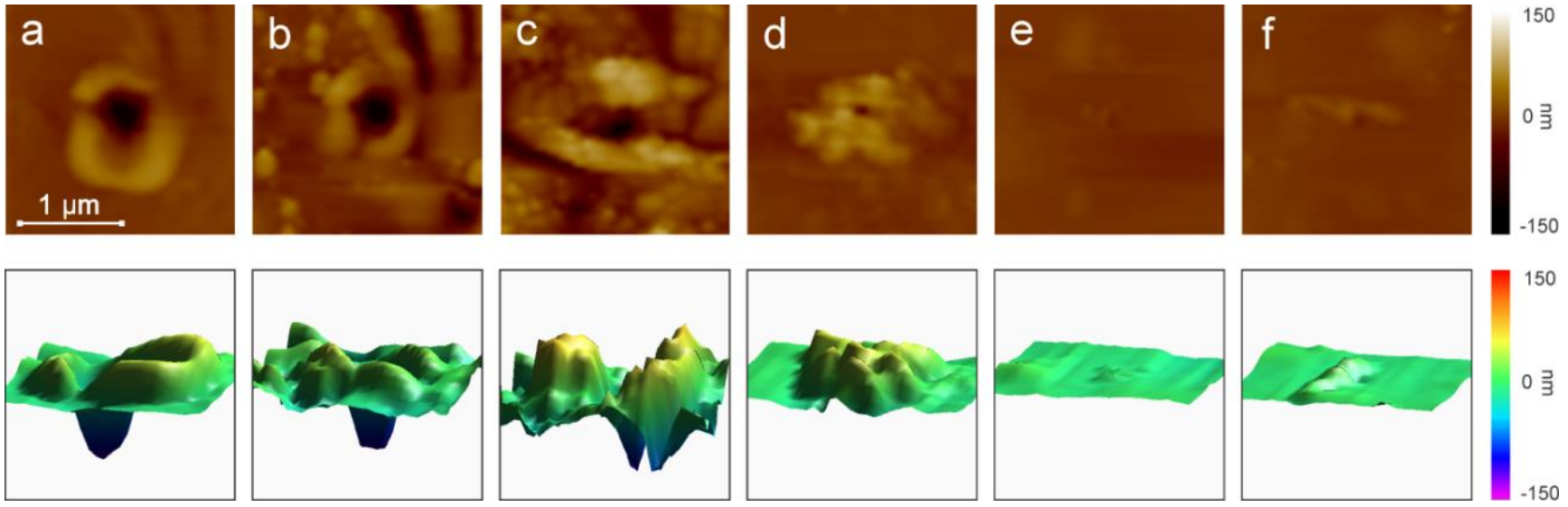

Figure 3.9. AFM topography and 3-D view of rhodamine B craters with laser wavelength at a) 450, b) 500, c) 550, d) 600, e) 650, and f) 700 nm.

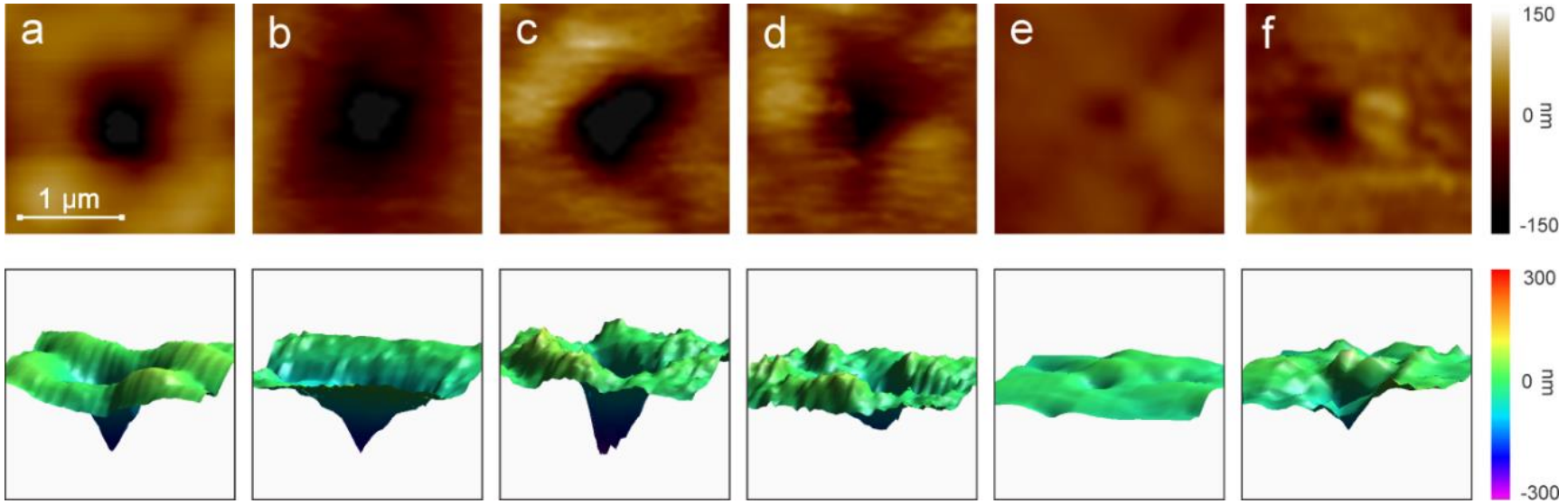

Figure 3.10. AFM topography and 3-D view of methylene blue craters with laser wavelength at a) 450, b) 500, c) 550, d) 600, e) 650, and f) 700 nm.

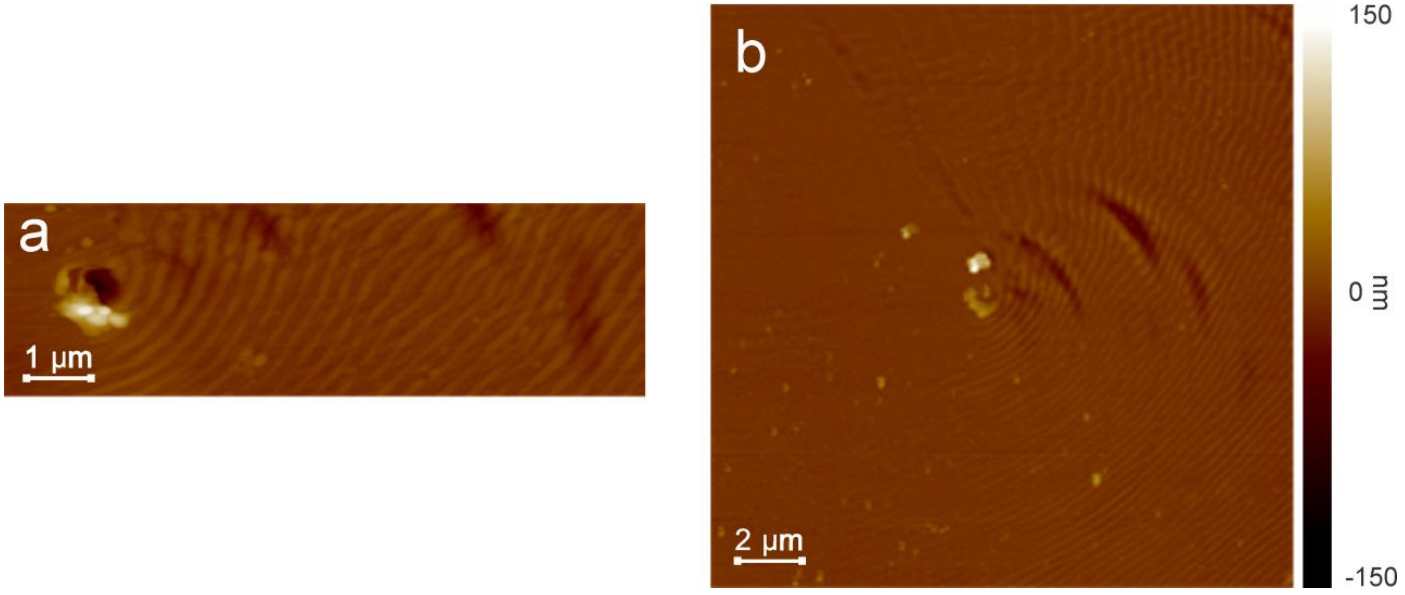

Figure 3.11. Images of ripple structures after tip-enhanced laser ablation on rhodamine B thin film with laser wavelength of 500 nm at energy of 100 µJ after 1 shot with image size of a) 3×10 µm and b) 20×20 µm.

Table 3.1. Mean depth and volume of ablation craters obtained at different wavelengths by tip-enhanced laser ablation

Wavelength (nm)	Crater volume (μm^3)		
	Rhodamine B	Methylene Blue	IR-797
450	14	60	42
500	16	150	55
550	10	130	54
600	1.7	40	25
650	0.5	10	9
700	0.4	20	13

Wavelength (nm)	Crater depth (nm)		
	Rhodamine B	Methylene Blue	IR-797
450	110	200	270
500	110	220	220
550	110	310	260
600	56	120	160
650	17	54	71
700	14	130	140

The wavelength dependence of tip-enhanced laser ablation was evaluated by plotting the calculated crater volume corresponding to Figure 3.8, 3.9, and 3.10 as a function of wavelength (solid circle with black line) with the optical absorbance (solid square with grey line) in Figure 3.12 for rhodamine B (a), methylene blue (b), and IR 797 chloride (c), respectively. Absorption of each sample was measured in the wavelength range from 400 to 1100 nm. Baseline subtraction was performed using the absorption of methanol solvent. The absorption maximum for rhodamine B solution was around 550 nm and low absorption was observed in the range of 600-800 nm. The absorption of the methylene blue has a maximum at 650 nm and low absorption between 400 and 550 nm and 700 and 800 nm. IR 797 chloride displayed a broad absorption compared to the other

dyes. Two main absorption peaks were observed for IR 797, with the absorption maximum around 800 nm and a second peak around 680 nm whereas low absorption was observed below 600 nm.

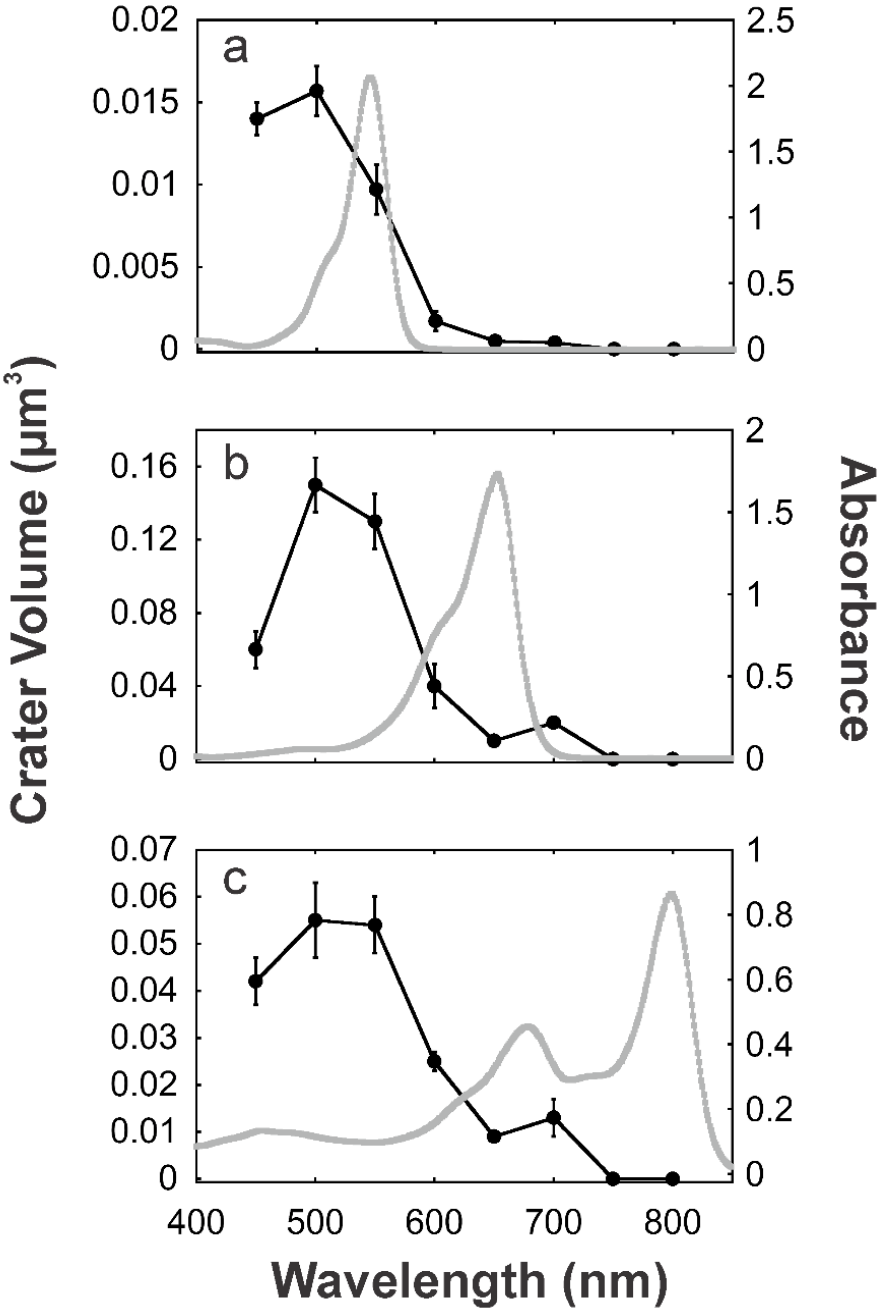

Figure 3.12. Tip-enhanced laser ablation crater volume (black line) and dye absorbance (grey line) as a function of visible and near-IR wavelength for a) rhodamine B, b) methylene blue, and c) IR 797.

The above data offer additional insights into the mechanism of tip-enhanced laser ablation. The thermal expansion of the probe was previously considered among the possible crater formation mechanisms and it was excluded for aperture SNOM laser ablation.[238] However, thermal expansion of the gold coated silicon AFM tip used in this work may contribute to the overall ablation crater formation. The tip thermal expansion was calculated assuming gold expanding against a rhodamine surface. The length of the AFM tip is approximately 15 μm and the thermal expansion coefficient of gold is 14×10^{-6} K^{-1} at 293 K. A previous report showed that the gold coating of the AFM tip melts during 532 nm irradiation,[261] which implies the temperature of the tip reaches the melting point of gold (1337 K). Thus, the length thermal expansion of the tip can be calculated to be approximately 200 nm. The AFM tip has an average spring constant of 60 N/m and the additional energy applied to the sample surface due to the thermal expansion of the gold coated tip can be calculated to be ~1.2 pJ. The crater volume of the rhodamine B sample at 500 nm is 0.016 μm^3, which corresponds to ~40 amol. The molar heat capacity of rhodamine B at 298 K is 700 $JK^{-1}mol^{-1}$,[262] and the 1.2 pJ energy applied onto the 40 amol rhodamine B due to tip thermal expansion would result in a temperature increase of 43 K, which is not enough to cause the melting or sublimation.

Crater formation by the force of the AFM tip due to thermal expansion was also evaluated. The force-displacement curve of the tip on a rhodamine B surface is shown in Figure 3.13. The drop in force after point A was due to the attractive force of the sample surface interacting with the AFM tip. The additional force applied to the sample due to the thermal expansion of the tip is about 12 μN based on the tip spring constant. If this force was sufficient to cause indentation, the plot would show a drop in force due to the relaxation of the bending cantilever, which was not observed. The rhodamine surface did not indent well past the 12 μN (point B in the plot) and no crater was

observed in an image obtained after the experiment, leading to the conclusion that the tip thermal expansion does not lead to surface indentation.

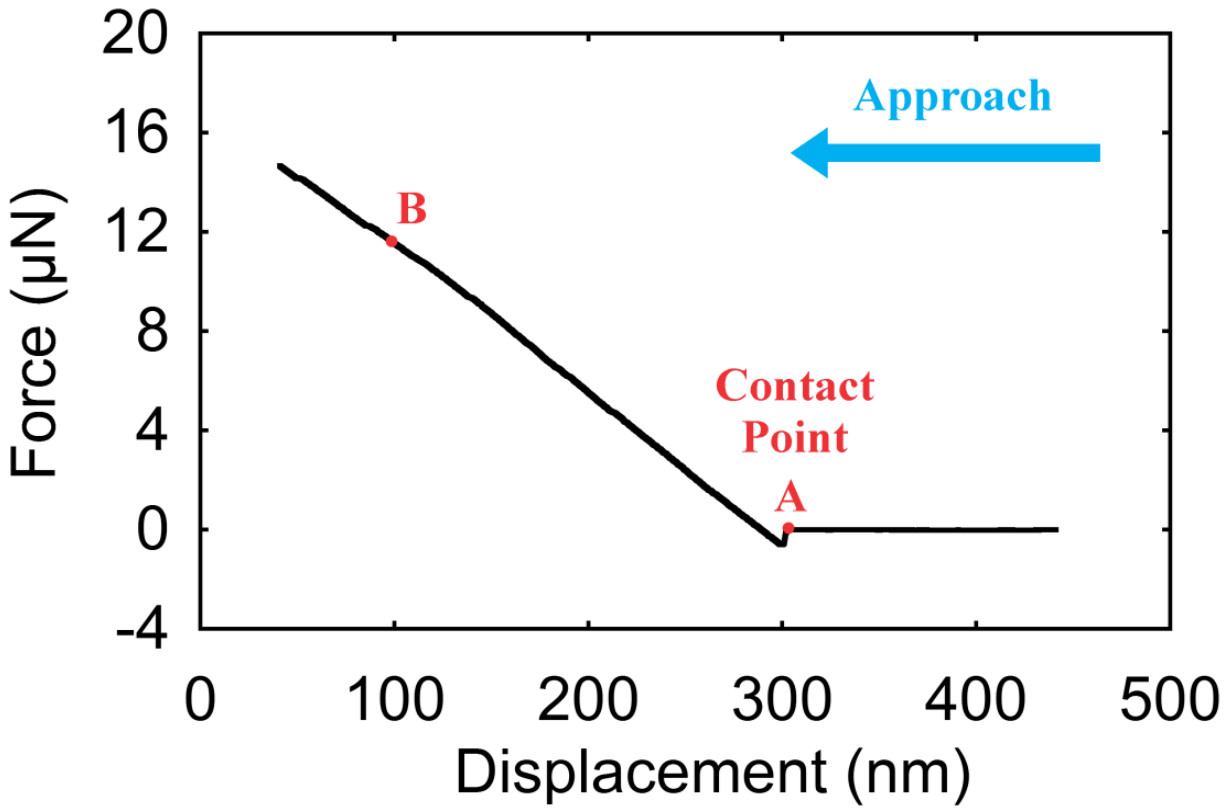

Figure 3.13. Force-displacement curve of the AFM tip approaching rhodamine B surface.

Previous studies suggested that the mechanism of aperture SNOM laser ablation involves either photothermal or ballistic effects.[263] If a photothermal mechanism is responsible, the absorption of the surface should affect the ablation process. The above results show that the absorption of the surface is not correlated with crater size in apertureless tip-enhanced laser ablation of organic dyes. The crater volume plotted against wavelength in Figure 3.12 for rhodamine B, methylene blue, and IR 797 are similar with the largest craters observed at around 500 nm. At the same time, the absorption spectra of the three dyes are quite different. Rhodamine

B has a maximum absorption around 550 nm. On the other hand, methylene blue and IR 797 had in relatively smaller craters at wavelengths close to their respective absorption maxima. These results suggest that a ballistic effect may be the main mechanism for apertureless tip-enhanced laser ablation of organic dyes and that photothermal effects linked to the nature of the surface are not required for ablation.

The results shown in Figure 3.12 are similar to those observed for anthracene wavelength dependent tip-enhanced laser ablation in this chapter. The largest craters were obtained at wavelengths near the plasmon resonance of gold is located. If it is assumed that the gold absorbs all of the incident laser energy, the kinetic energy of ejected gold atoms can be estimated. The melting point of rhodamine B is ~480 K and its molar heat capacity at room temperature is ~700 $JK^{-1}mol^{-1}$.[262] In order to melt the 40 amol of rhodamine B in the crater, an energy of 5 pJ is required. The velocity of gold atom plume is ~5000 m/s under vacuum.[264] To achieve the required energy of 5 pJ, a gold mass of 0.4 fg must be ejected from the tip surface at this velocity. The melted gold on the AFM tip can be approximated a 1 μm diameter hemi-sphere 10 nm above the surface. The crater diameter of rhodamine B is 500 nm. When the center of the crater and the gold sphere are aligned, a spherical cap surface area on the gold sphere can be considered as the source for generation of the atoms. This spherical cap surface area is 0.16 μm^2, which is equivalent to a 0.45 fg monolayer of gold atoms, which is in the same order of magnitude as the required mass. Thus, a mechanism where ejected gold atoms ablate material from the surface is plausible.

AFM was operated in tapping mode for tip-enhanced laser ablation. Because the gold coating on the tip melts, the tip at the melting point of gold is in contact with the surface. Therefore, heat transfer from the AFM tip to the sample surface by direct contact needs to be considered. The thermal conductivity of rhodamine B has not been reported in the literature; however, the thermal

conductivity for some nitric[265] and chloride salts[266] is reported to be ~0.5-1 $Wm^{-1}K^{-1}$ and this value has been used for the calculations below. The rhodamine crater at 500 nm has an area of 0.25 μm^2 and a depth of 110 nm and the energy required for melting the material inside the crater is 5 pJ (vide supra). Assuming the heat is completely transferred to the rhodamine B, the thermal diffusion time required to melt the rhodamine B at a depth of 110 nm is ~5 ns according to Fourier's law.[267] The tip oscillates at a frequency of 300 kHz. Defining the contact time of the tip with the sample surface as the time in which the tip-surface distance is < 1 nm, the contact time is ~160 ns per oscillation, which is 30 times longer than required for melting the crater. Therefore, crater formation due to direct heat transfer from the tip cannot be excluded.

3.5 Summary

In this chapter, the wavelength dependence of crater formation by tip-enhanced laser ablation in the visible and near-IR range was described. The wavelength for maximum crater size was around 500 nm and the crater volume decreased linearly between 500 and 800 nm regardless of the sample. No crater was observed in the near-IR range from 800 to 1200 nm in all cases. The crater formation is not dependent on the optical absorbance of the material as would be expected for photothermal ablation. The likely mechanisms for crater formation by TELA are ballistic ejection of gold atoms from the tip surface and heat transfer from the tip contact with the surface.

The ability to tune the crater size with wavelength suggests potential utility of the method for laser nanomachining of surfaces. Because the material removal is dependent on the wavelength, the size and volume of the crater on surface could be adjusted by tuning the wavelength of the incident laser beam.

The results suggest some potential improvements for tip-enhanced laser ablation sampling through more efficient energy absorption by the tip and by more efficient ballistic ablation

compared to direct contact heating. First, efficient absorption of energy by the tip at 500 nm is consistent with the plasmon resonance of a thin film (ca. 10 nm) or partially coated tip. This thin coating or partial coating of the tip may be induced by laser heating and melting or ablation of the gold on the tip surface (see Fig 3.1). A tip coating less than the initially 35 nm thick coating used in this study might allow lower laser energy to produce efficient ablation. Second, the use of a spherical particle AFM tip may be effective at providing more surface area for ballistic ejection of material. This could increase the amount of ballistic ejected material compared to the melted material that is not removed from the sample and therefore is not efficiently sampled. Microspheres have been used as AFM force measurement tips[268] and could provide greater surface area for ejection of material and enhanced heat transfer.

CHAPTER 4. TIP-ENHANCED LASER ABLATION AND CAPTURE OF DNA

The goal of the research described in this chapter was to utilize AFM tip-enhanced laser ablation to sample intact plasmid DNA for polymerase chain reaction (PCR) amplification. The wavelength of the incident laser was 532 nm, which is efficient for tip-enhanced laser ablation. A 7.1 kbp green fluorescent protein (GFP) plasmid DNA deposited on a glass coverslip was ablated and captured on a metal ribbon 300 μm above the surface. The ablation craters had diameters from 1-2 μm and an average value of 0.14 μm^3. PCR and nested PCR were employed for the amplification of the ablated DNA. The quantity of material from each ablation crater for PCR amplification was 20 ag. The sampling and amplification efficiency was estimated at 0.01 %.

4.1 Introduction

Atomic force microscopy (AFM) has been widely used in the study of nucleic acids and chromosomes due to its unique capabilities of imaging and characterization.[64-66] AFM has been used to image DNA and RNA molecules with nanometer spatial resolution.[64, 66-67] With AFM imaging, various structures and topologies of DNA and RNA can be observed for three-dimensional characterization of nucleic acids and their polymeric form, which can lead to a better understanding of their genomic function. High-speed AFM can facilitate direct visualization of dynamic structure changes and dynamic processes of DNA and RNA at high imaging rates.[72] AFM-based spectroscopic techniques such as TERS facilitate direct sequencing of single strand DNA and RNA.[166, 171, 269]

AFM can measure the mechanical characteristics of single molecules of DNA and RNA. When the AFM tip is placed in contact with a DNA or RNA, a single molecule can be attached to the AFM tip allowing measurement of the adhesive forces between complementary strands.[270] With

this approach, the elastic behavior of both single and double stranded DNA and RNA were measured by stretching the strands.[91-93] The pair binding strength between each nucleic acid base pair was measured by unzipping the double stranded DNA.[94]

TELA can be used for sampling material on the submicron scale[192] and was used for surface nanopatterning,[191] to create ions for mass spectrometry,[216, 271] ablate neutrals for post-ionization mass spectrometry,[217, 272] and ablate material for off-line mass spectrometry.[227] TELA is capable of removing peptides and proteins from a surface without fragmentation.[227]

In the work described in this chapter, TELA was used for ablation and capture of DNA. A 532 nm wavelength laser was used with a gold-coated AFM tip to ablate and capture plasmid DNA that was amplified by polymerase chain reaction (PCR) and nested PCR to evaluate the integrity. The transfer efficiency of the ablated DNA was estimated by comparison to known concentrations of the plasmid.

4.2 Experimental

The tip-enhanced laser ablation system configuration described in Chapter 2 was used for all the experiments for this section. The studies in Chapter 3 showed that the sharp tip of the probe is altered by interaction with the laser and the diameter of the tip after exposure to the pulsed laser is approximately 1 μm. The wavelength of the laser was set to 532 nm which is near the maximum for laser ablation efficiency while at the same time allowing comparison with studies using a frequency doubled Nd:YAG laser. The laser was mildly focused onto the target to avoid far field ablation and a pulse energy of 600 μJ was used for the experiments described below. A 25 × 500 μm silver ribbon was positioned 300 μm above the AFM tip to capture the ablated material. Three dimensional images were constructed from the AFM data using custom software written in LabVIEW, which was also used to calculate crater and rim volumes.

Green fluorescent protein (GFP) plasmid was cloned from pBABE GFP (Addgene plasmid #10668, Cambridge, MA, USA). Working solutions of the plasmid were prepared in nuclease-free molecular biology grade water (HyClone, Logan, UT, USA) at concentrations of 92 ng/μL and a volume of 2 μL was pipetted onto a glass coverslip. The sample was dried at room temperature before laser ablation. Ablation craters were obtained using 10 laser shots with a 1 s delay between each shot. The material captured on the ribbon was extracted into 20 μL of water and PCR amplification was performed using primer F1/R1 (Table 4.1) with a thermal cycler (iCycler, Bio-Rad, Hercules, CA, USA).

PCR amplification was carried out with a ReadyMix PCR Kit (KAPA Biosystems, Boston, MA, USA) which contains DNA polymerase in reaction buffer, dNTPs (0.2 mM of each dNTP), $MgCl_2$ (1.5 mM), and stabilizers. Each PCR reaction solution contained 0.6 μL of DNA template, 1.5 μL of F1/R1 primers (10 μM), and 7.9 μL of nuclease-free biology grade water to reach a final volume of 20 μL. PCR cycling comprised one initial denaturation cycle at 95 ℃ for 1 min, 9 cycles of polymerase activation at 95 ℃ for 1 min, 50 ℃ for 30 s, 72 ℃ for 20 s, followed by 30 cycles of amplification at 95 ℃ for 20 s, 50 ℃ for 30 s, and 72 ℃ for 20 s. Nested PCR amplification was carried out first with primer F2/R2 (Table 4.1) and the products from the first amplification were again amplified with primer F1/R1 using the same PCR procedure. Nested PCR included one cycle of initial denaturation at 95 ℃ for 1 min, 9 cycles of polymerase activation at 95 ℃ for 1 min, 50 ℃ for 30 s, 72 ℃ for 20 s, followed by 20 cycles of amplification at 95 ℃ for 20 s, 50 ℃ for 30 s, and 72 ℃ for 20 s. TAE buffer stock solution was prepared by using 40 mM tris-aminomethane (Bio-Rad) and 1 mM EDTA (Bio-Rad) with the pH adjusted to 8.5 using acetic acid (Fisher Scientific, Pittsburgh, PA, USA). PCR products were mixed with ethidium bromide (Invitrogen, Carlsbad, CA, USA) and electrophoretically separated in a 1.8 % agarose gel I (Fisher) for one hour at 80

volts in TAE buffer. Amplicon sizes were determined by comparison with a 100 bp molecular ruler (EZ Load, Bio-Rad). Gels were imaged with a gel imager (Gel Doc EZ Imager, Bio-Rad).

Table 4.1. Primer sequences

Primer	5'-3' Sequence	Product Size (bp)
F1	CCATCCTGGTCGAGCTGGAC	160
R1	TAGGTCAGGGTGGTCACGAG	
F2	ATGGTGAGCAAGGGCGAG	260
R2	GACTTGAAGAAGTCGTGCTG	

4.3 TELA for DNA

GFP plasmid was used to evaluate the efficiency of DNA ablation and capture and the integrity of the captured DNA using tip-enhanced laser ablation. A 2 µL volume of GFP plasmid in water at a concentration of 92 ng/µL was deposited on a glass cover slip and dried before the cover slip was mounted on the AFM sample stage. Tapping mode AFM images are shown in Figure 4.1. The features in Figure 4.1a are approximately 30 µm long and 500 nm in height and likely result from aggregation of the DNA on the cover slip that form when the solvent evaporates from the deposited droplet. The morphology of dried DNA deposits depended on the solvent and solution concentration.[273] For the solutions used in this study, the coarse morphology of the DNA deposit was a branched dendritic structure with 10 µm wide spines.

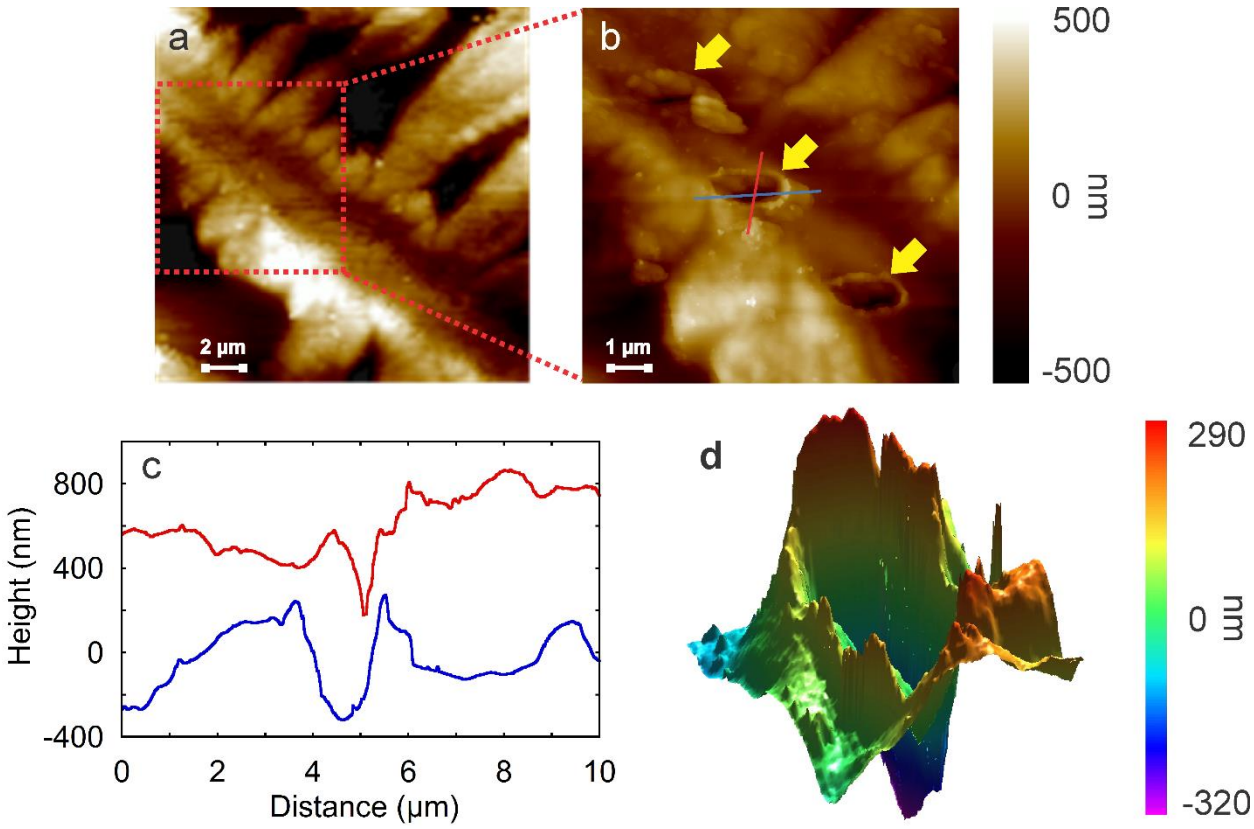

Figure 4.1. Topography of GFP plasmid a) before and b) after tip-enhanced laser ablation, c) depth profile along the red and blue line across the ablated crater, and d) three-dimensional plot of the crater.

Figure 4.1b shows an expanded AFM image of the region that was sampled by tip-enhanced laser ablation. Three spots were ablated on the surface and these are indicated with arrows in the image. Each of the ablation craters was formed by 10 laser shots and has a similar elliptical contour with the major axis perpendicular to the cantilever axis. The depth profile corresponding to the red and blue lines in Figure 4.1b is shown in Figure 4.1c. This crater has a depth of approximately 300 nm with a major axis of 1.7 µm and a minor axis of 1 µm and a volume of 0.16 μm^3. A crater rim 50-100 nm higher than the surrounding surface was observed for each spot. Crater formation was observed previously[261] and may be the result of melting and resolidification of the material

surrounding the crater. The depth profile before and after ablation is shown in Figure 4.2 and a three-dimensional representation of the crater is shown in Figure 4.1d. The dashed and solid lines represent the surface height before and after tip-enhanced laser ablation, respectively. A clear formation of the crater with a depth around 300 nm was observed after ablation.

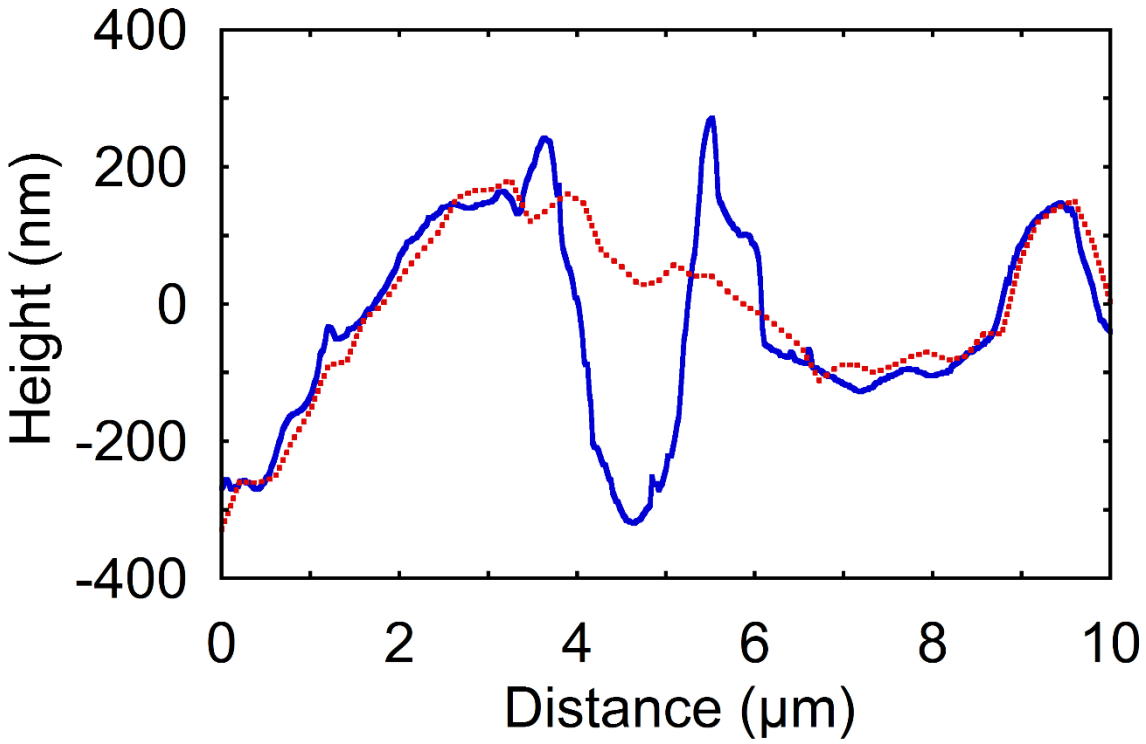

Figure 4.2. AFM topography of GFP sample surface before (dashed line) and after (solid line) tip-enhanced laser ablation

Plasmid DNA was collected from multiple spots of the GFP plasmid for PCR amplification. Material was ablated from ten spots with 10 laser shots per spot in a 20 × 20 μm region and collected on the metal ribbon above the AFM tip. A representative AFM image of an ablated region scanned after sampling is shown in Figure 4.3. The spots were ablated at 1 Hz repetition rate and had similar elliptical contours. The depth profile corresponding to the indicated line in Figure 4.3a

is shown in Figure 4.3b. The craters had an average depth of 208 ± 15 nm, a major axis of 1.5 ± 0.14 µm, and a minor axis of 0.6 ± 0.1 µm. The average volume was 0.14 μm^3 with a relative standard deviation of 12 %.

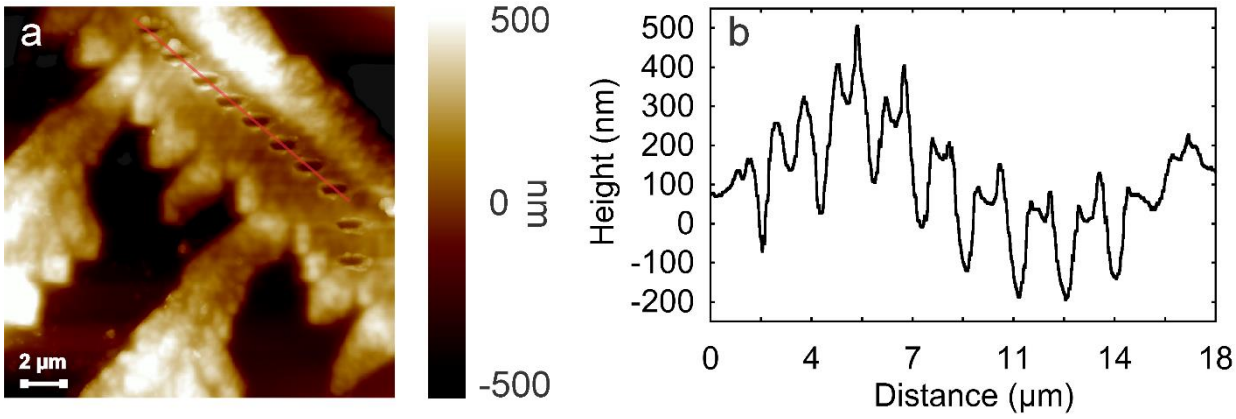

Figure 4.3. Topography (a) and depth profile (b) after ten spots were ablated from the GFP plasmid sample surface.

PCR amplification was performed on the collected material which was transferred into 20 µL water by depositing the ribbon in a 300 µL microcentrifuge tube and vortexing for 30 s. A 0.6 µL aliquot of each sample was added to the PCR reaction mixture. Primers F1 and R1 listed in Table 4.1 were used for the PCR amplification. A representative agarose electrophoresis gel of PCR amplified products is shown in Figure 4.4. Molecular weight markers with 100 bp per step were loaded on the center and flanking lanes (labelled L). Three samples from the three sets of ten ablated spots were amplified and loaded on the left half of the gel (Lanes B, C and D). Negative controls were created by running the amplification steps with water in place of plasmid DNA. A negative control run before the plasmid DNA is in Lane A and a second run after the plasmid DNA is in Lane E. The lanes on the right half of the gel were loaded with serial dilutions of the plasmid equivalent to 6000, 600, 60, 6, and 0.6 ag (Lanes F–J respectively). The amplification product for

the PCR reaction was a fragment 160 bp in length. The negative controls do not display any detectable band whereas the three lanes with the captured samples display bands at the expected 160 bp at the same position as the dilution series.

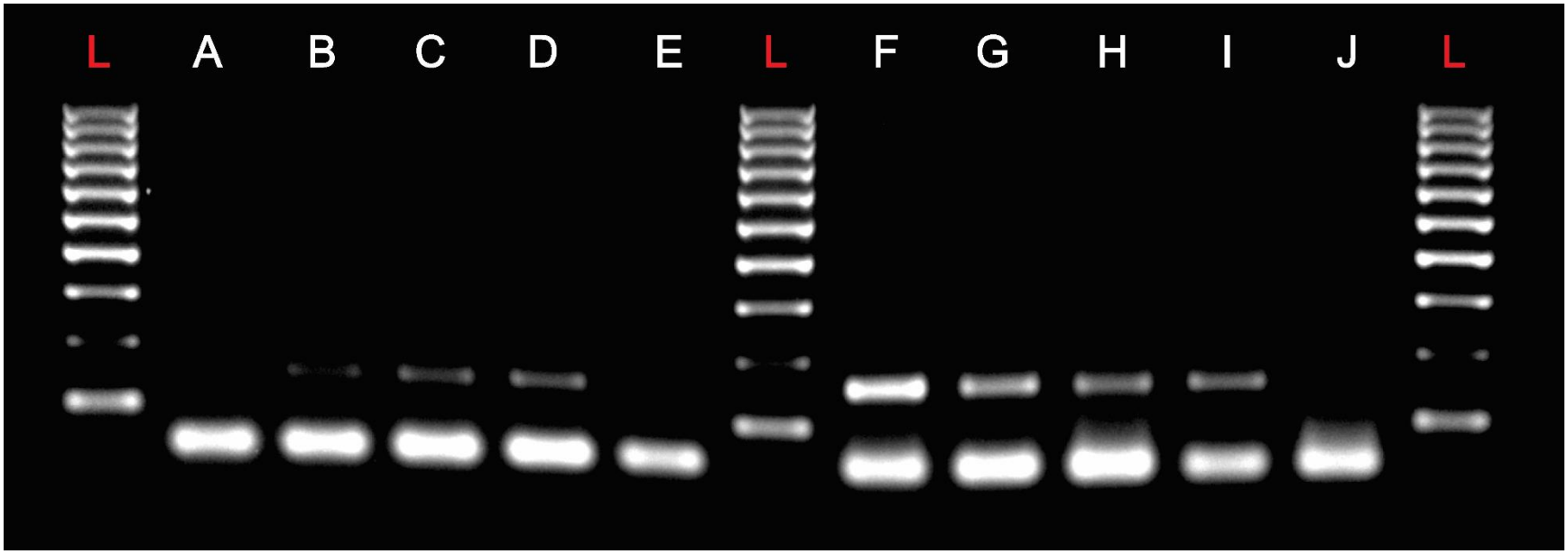

Figure 4.4. Electrophoresis gel of PCR products. Negative control before (Lane A) and after sampling (Lane E); Lanes B, C, and D correspond to three ablated and collected samples, Lanes F–J correspond to serial dilutions of GFP DNA with amounts 6000, 600, 60, 6, and 0.6 ag respectively, and Lane L is a 100 bp molecular weight ladder.

The band intensity for Lanes F-J in Figure 4.4 was integrated and a calibration curve was constructed (Figure 4.5). Using this calibration, the quantity of collected DNA for lanes B, C, and D corresponds to 2, 6 and 10 ag, respectively. Only 3 % of the captured material was used for PCR amplification, therefore, the total amount collected for each sample was 70, 200 and 320 ag, respectively. The quantity of DNA ablated and capture from each ablation spot was approximately 20 ± 13 ag/spot. Based on the calibration, the negative control corresponded to less than 0.3 ag. The average crater volume of 0.14 μm^3 which corresponds to 100 fg at 1.7 g/cm^3 DNA density.[274] The biomolecule transfer efficiency of was measured at 3 %,[227] suggesting that either transfer, extraction, or amplification of the DNA is two orders of magnitude less than anticipated.

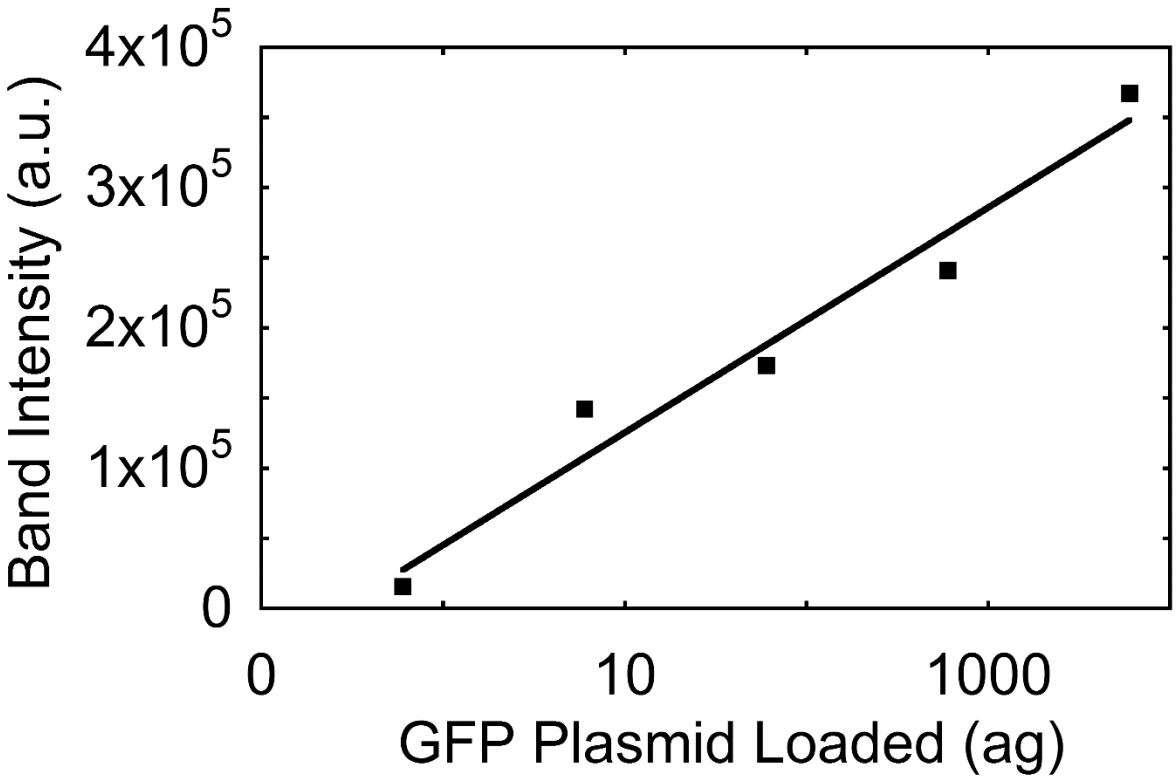

Figure 4.5. Calibration curve for GFP plasmid from the integrated gel band signal

The specificity of the ablated and captured plasmid DNA amplification step was assessed using nested PCR. Aliquots of captured DNA were first amplified using primers F2 and R2 (Table 4.1) with a product length of 260 bp. The resulting PCR products were amplified with primers F1 and R1 (Table 4.1) to generate a 160 bp product, which minimized the non-specific amplification of the captured DNA. An agarose gel electrophoresis separation of the nested PCR products is shown in Figure 4.6 with products from the captured samples in Lanes B, C, and D. Negative controls run before and after sample capture are in Lanes A and E, respectively. A 6 fg quantity of plasmid was loaded in Lane F as a positive control. A molecular weight ladder with 100 bp steps was in the two lanes labelled Lane L. A 160 bp band is visible in the 3 samples lanes (B, C, and D) and the positive control in Lane F. No band was observed in in the negative control Lanes A and E, confirming that

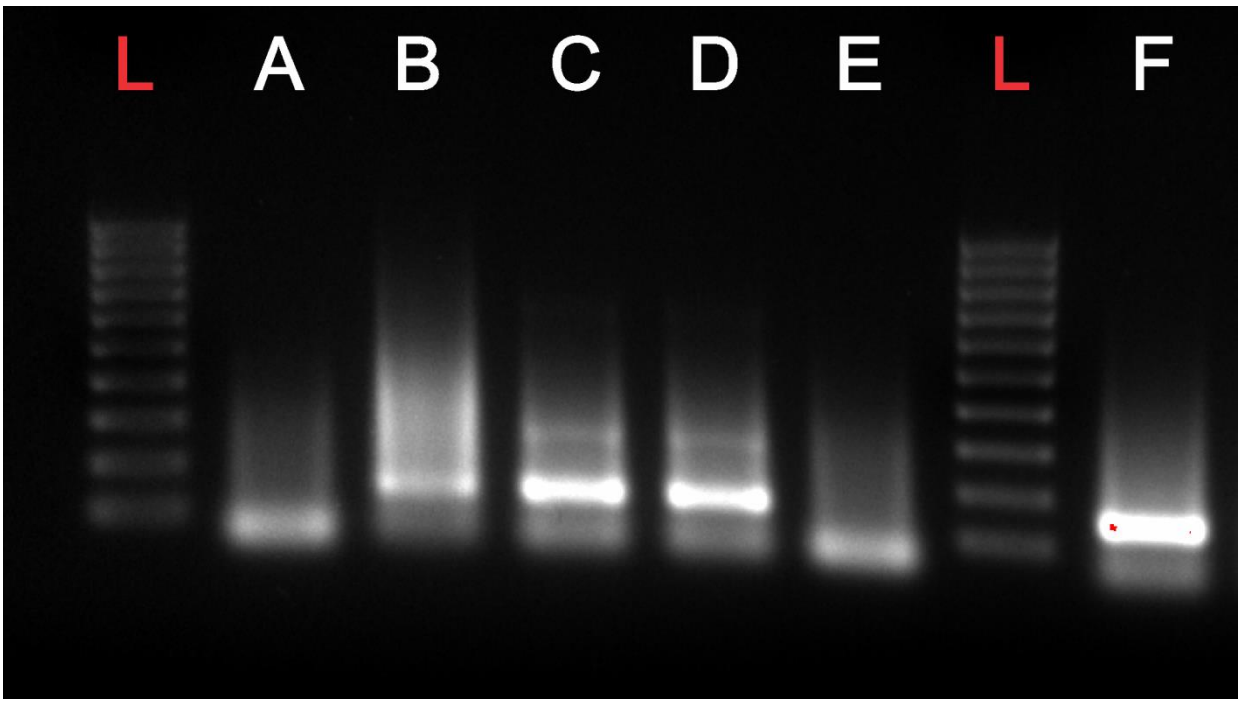

Figure 4.6. Electrophoresis gel of nested PCR products. Negative control A) before (Lane A) and after sampling (Lane E), Lanes B, C, D are replicate laser ablated and collected samples, Lane F is positive control, and Lane L is a 100 bp molecular weight ladder.

the tip-enhanced laser ablation collected material corresponds to GFP plasmid DNA. The intensity of the nested PCR bands in the ablated and captured samples is consistent with the quantity found in the PCR amplification.

The tip-enhanced laser ablation of plasmid DNA provided a sufficient quantity of intact material for PCR amplification experiments. This suggests that the ability to ablate and capture intact DNA using tip-enhanced laser ablation is comparable to that reported previously using far-field laser ablation.[275-278] For example, 600 bp dsDNA was ablated and captured intact using a 581 nm visible laser and a water-ice matrix.[275] Ablation and capture of intact 1000 bp single stranded DNA was achieved using a rhodamine 6G matrix and a 532 nm pulsed laser.[278] Pulsed 2.94 μm IR lasers were used to ablate and ionize intact 500 bp dsDNA[277] and ablate and capture a intact 3200 bp double-stranded DNA plasmid.[276]

The lower than anticipated quantity of DNA recovered and amplified may be due to several factors including inhomogeneous distribution of the DNA in the deposited sample, DNA fragmentation during the ablation process, DNA degradation on the surface, or inefficient extraction. The quantity of DNA recovered was estimated with the assumption that the sample deposit was homogeneous; however, if the ablated material was not as dense as assumed or if it was a mixture of DNA and non-DNA material, this could lead to a lower recovery. TELA sampling was achieved for proteins up to 5.7 kDa without fragmentation.[227] The mass of the analyte in this work is much higher (i.e. 7.1 kbp, equal to over 4.5 million Da), and fragmentation cannot be excluded. DNA degradation on the AFM target surface could arise from deoxy-ribonucleases or oxidation. Although the presence of deoxy-ribonucleases is unlikely, the plasmid DNA was exposed to ambient air for several hours, which may lead to oxidation. Whereas dry DNA is stable

at room temperature for weeks,[279-280] wet samples such as those used in this work can degrade.[279] Finally, inefficient extraction of DNA from the capture surface cannot be ruled out.

AFM imaging of genomic material and TELA sampling can be performed using the same tip with minimal carryover between sampling and imaging as evidenced by Lane E in Figure 4.4 and Figure 4.6 which corresponds to the negative control after sampling. Capture of DNA with an AFM tip was reported using a tweezer-type AFM probe to clamp and pick up chromosome fragments.[115] While the approach is effective at sampling DNA from a surface, it requires different tips for imaging and extraction. DNA sampling and imaging with a single tip can be achieved with adsorption,[281] although achieving reproducible results can be challenging.[282] Both the tweezer and adsorption approaches require direct contact between the sample and the AFM tip.

4.4 Summary

In this chapter, tip-enhanced laser ablation was demonstrated for DNA sampling followed by PCR and nested PCR amplification of the collected material. Sampling of a 7.1 kbp GFP DNA plasmid was achieved and amplification of fragments up to 260 bp was demonstrated. Craters with 1-2 μm in diameter and depth of 200 nm were obtained. No carryover of the sample was observed for DNA sampling by TELA. The sampling and amplification efficiency was estimated at 0.01%.

Whereas TELA can sample genomic material from volumes below 1 μm^3, improvement in transfer efficiency will be necessary for DNA sequencing which requires picogram quantities of DNA.[283-286] Future efforts will focus on improving the capturing step of TELA as well as testing integration with other AFM based DNA manipulation techniques.

CHAPTER 5. CONCLUSIONS AND FUTURE DIRECTIONS

In this dissertation, atomic force microscopy tip-enhanced laser ablation (AFM TELA) was described. An OPO wavelength tunable laser was directed onto a gold-coated AFM tip, which was held close to a surface to generate tip-enhanced laser ablation for ambient sample removal with a sampling size at the sub-micrometer level. The wavelength dependence of TELA was studied, which was used to elucidate the mechanisms behind this approach. TELA was applied to DNA ablation and capture for amplification.

The wavelength dependence of TELA for an anthracene thin film is described in Chapter 3. The wavelength was tuned from 450 to 1200 nm to cover both visible and near-IR region, where the absorbance of anthracene is low. The volume of the crater formed by TELA was largest at 500 nm and no crater formation was observed in the near-IR region of 800-1200 nm. The trend of crater formation with wavelengths was found to be consistent with the absorption of the gold on the AFM tip. The mechanism of TELA for anthracene ablation may be due to a ballistic effect, where the gold or molecules adsorbed on the AFM tip are ejected and hit the surface causing heating and ejection of the surface material. In addition, since the AFM tip was operated in tapping mode, heat transfer through direct contact between the probe and the surface may also occur.

The wavelength dependence of TELA system was also investigated with three organic dyes, which have different optical absorption and relative high sublimation enthalpy, as discussed in Chapter 3. Three dyes, rhodamine B, methylene blue, and IR 797 chloride with different absorption maxima in the visible and near-IR were studied in the wavelength range from 450 to 800 nm. In all cases, the maximum volume of the crater was around 500-550 nm and no crater formed in the near-IR region. The crater formation does not track the absorption spectra except for rhodamine B, which absorbs well around 550 nm. Instead, the results for all three organic dyes were consistent

with the plasmon absorption of the gold AFM tip, which agrees with the result found for anthracene. Therefore, the mechanism of TELA of organic dyes is likely a ballistic effect or thermal transfer through the tip in contact with the surface.

TELA sampling and capture was employed for a 7.1 kbp GFP DNA sample, which is described in Chapter 4. The DNA plasmid was ablated at 532 nm with a sampling volume around 0.14 μm^3 and captured on a metal ribbon with no carryover observed. Both PCR and nested-PCR amplification were employed for the captured DNA and strands up to 260 bp were observed. The quantity of the transferred plasmid DNA form each ablation crater was 20 ag. The transfer and amplification efficiency was estimated to be around 0.01 %.

One of the future directions of this research will focus on improving the transfer efficiency of the TELA system by using a droplet instead of the metal ribbon. The composition of the droplet can be adjusted to suit the polarity of the target material, where better capture efficiency may be achieved for TELA sample transfer. Figure 5.1 represents a configuration of droplet capture for TELA system. The capillary has an O.D. and I.D. of 360 µm and 50 µm, respectively. A droplet with a diameter of approximately 400 µm has a volume of 35 nL was delivered to the cleaved capillary. The pumping speed of the solution must be adjusted to compensate for the evaporation of the droplet under ambient conditions. Another challenging of this approach is the dilution of the captured material.

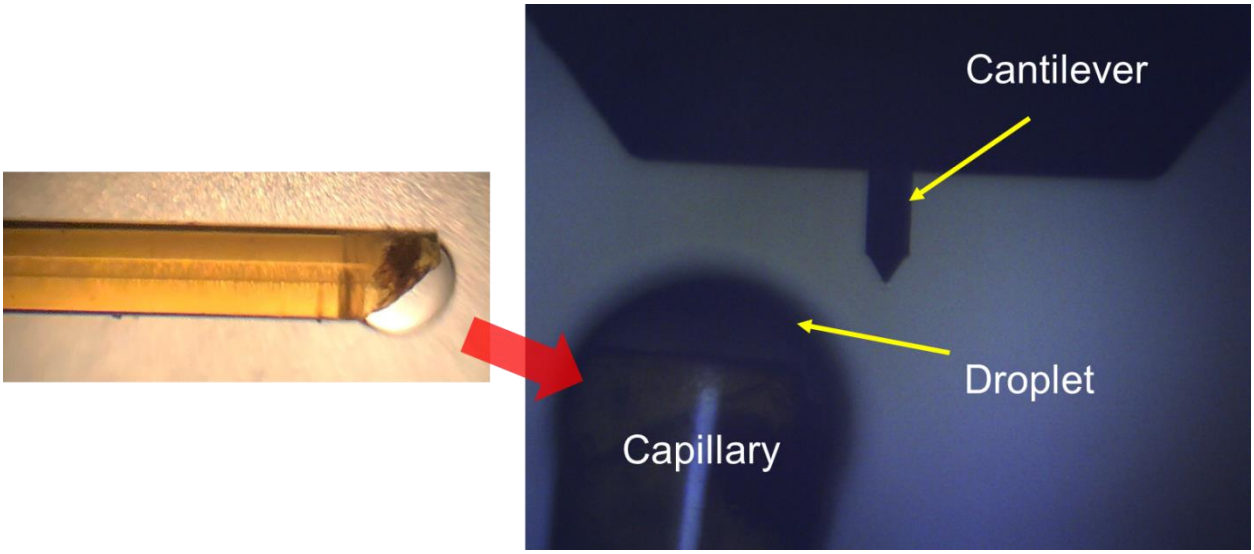

Figure 5.1. Scheme of droplet capture for tip-enhanced laser ablation

A second future direction will focus on sampling genomic material from single cells or tissue samples with TELA. Biological samples are typically analyzed in bulk and the collected data are averaged assuming homogeneity of the cellular material. However, heterogeneity of individual cells is an important factor in proteomics, lipidomics, metabolomics, and genomics at the single cell level.[287-290] In particular, analysis of DNA and RNA at the single cell level can provide new perspectives and advances to the understanding of biological ecosystems and organisms.[287, 291-292] Conventional single cell analysis requires single cell sorting and isolation where the spatial information of individual cells is missing.[287] Laser capture microdissection (LCM) can keep the spatial information of cells for single cell sampling[293-294] at a resolution of 3-5 µm.[295] With the ability of 1 µm sampling size demonstrated, TELA can be a potential ambient sampling tool for precise extraction of genomic material directly from tissue sections for further PCR amplification or single cell sequencing.

A third future direction will focus on employing TELA for nanomachining. Since the size of the crater formation is most likely dependent on the absorption of the AFM tip instead of the material, nano-machining in different sizes for different surfaces could be achieved by tuning the wavelength of the laser. Figure 5.2 shows the preliminary data of nanomachining by TELA on a silicon wafer. The wavelength was tuned to 500 nm with laser energy of 150 μJ. The crater formation from left to right was obtained with 10, 20, and 30 laser shots. The diameter of the craters was measured to be less than 200 nm. TELA may be an additional potential tool for nanomachining among tip-based nanofabrication methods.[191]

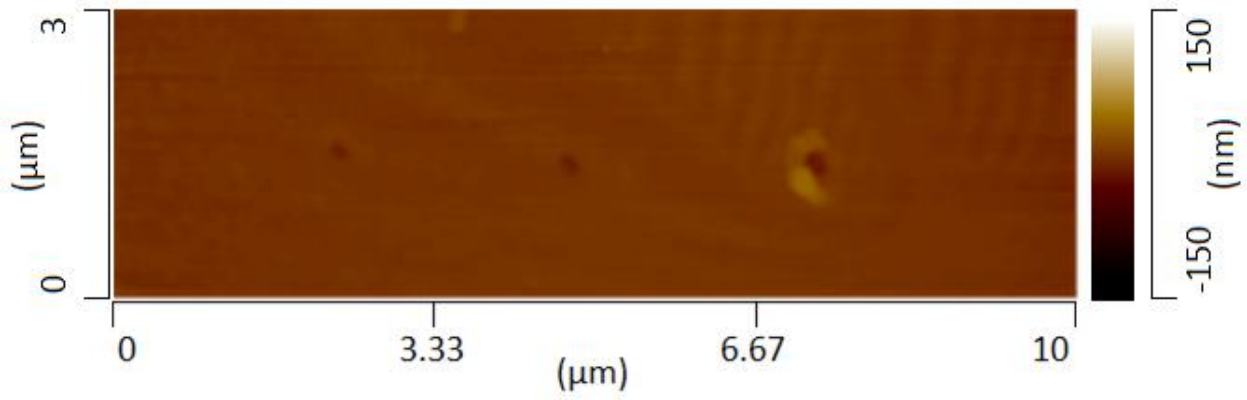

Figure 5.2. Silicon wafer ablation by tip-enhanced laser ablation at 500 nm

REFERENCES

1. Rohrer, H., The Nanoworld: Chances and Challenges. *Microelectron. Eng.* **1996,** *32*, 5-14.

2. Feynman, R. P., There's Plenty of Room at the Bottom. *Feynman and Computation: Exploring the Limits of Computers* **1959**.

3. Rohrer, H., The Nanometer Age: Challenge and Chance. *Microelectron. Eng.* **1995,** *27*, 3-15.

4. Appell, D., Nanotechnology: Wired for Success. Nature Publishing Group: 2002.

5. Heath, J. R.; Kuekes, P. J.; Snider, G. S.; Williams, R. S., A Defect-tolerant Computer Architecture: Opportunities for Nanotechnology. *Science* **1998,** *280*, 1716-1721.

6. Mamalis, A. G., Recent Advances in Nanotechnology. *J. Mater. Process. Technol.* **2007,** *181*, 52-58.

7. Mathur, N., Nanotechnology: Beyond the Silicon Roadmap. *Nature* **2002,** *419*, 573.

8. Balzani, V.; Credi, A.; Venturi, M., Molecular Devices and Machines. *Nano Today* **2007,** *2*, 18-25.

9. Gan, Z.; Cao, Y.; Evans, R. A.; Gu, M., Three-dimensional Deep Sub-diffraction Optical Beam Lithography with 9 nm Feature Size. *Nat. Commun.* **2013,** *4*, 2061.

10. Kozawa, T.; Yoshida, Y.; Uesaka, M.; Tagawa, S., Radiation-induced Acid Generation Reactions in Chemically Amplified Resists for Electron Beam and X-ray Lithography. *Jpn. J. Appl. Phys.* **1992,** *31*, 4301.

11. Mack, C., *Fundamental Principles of Optical Lithography: The Science of Microfabrication*. John Wiley & Sons: **2008**.

12. Tseng, A. A.; Chen, K.; Chen, C. D.; Ma, K. J., Electron Beam Lithography in Nanoscale Fabrication: Recent Development. *IEEE Trans. Electron. Packag. Manuf.* **2003,** *26*, 141-149.

13. Vieu, C.; Carcenac, F.; Pepin, A.; Chen, Y.; Mejias, M.; Lebib, A.; Manin-Ferlazzo, L.; Couraud, L.; Launois, H., Electron Beam Lithography: Resolution Limits and Applications. *Appl. Surf. Sci.* **2000,** *164*, 111-117.

14. Watt, F.; Bettiol, A. A.; Van Kan, J. A.; Teo, E. J.; Breese, M. B. H., Ion Beam Lithography and Nanofabrication: A Review. *Int. J. Nanosci.* **2005,** *4*, 269-286.

15. Bottomley, L. A., Scanning Probe Microscopy. *Anal. Chem.* **1998,** *70*, 425-476.

16. Meyer, E.; Hug, H. J.; Bennewitz, R., *Scanning Probe Microscopy: The Lab on A Tip*. Springer Science & Business Media: **2013**.

17. Salapaka, S. M.; Salapaka, M. V., Scanning Probe Microscopy. *IEEE Control Syst.* **2008,** *28*, 65-83.

18. Reimers, J. R., *Computational Methods for Large Systems: Electronic Structure Approaches for Biotechnology and Nanotechnology*. John Wiley & Sons: **2011**.

19. Srivastava, D.; Menon, M.; Cho, K., Computational Nanotechnology with Carbon Nanotubes and Fullerenes. *Comput. Sci. Eng.* **2001,** *3*, 42-55.

20. Tsukerman, I., *Computational Methods for Nanoscale Applications: Particles, Plasmons and Waves*. Springer Science & Business Media: **2007**.

21. Hammer, N. I.; Emrick, T.; Barnes, M. D., Quantum Dots Coordinated with Conjugated Organic Ligands: New Nanomaterials with Novel Photophysics. *Nanoscale Res. Lett.* **2007,** *2*, 282.

22. Stura, E.; Nicolini, C., New Nanomaterials for Light Weight Lithium Batteries. *Anal. Chim. Acta* **2006,** *568*, 57-64.

23. Wang, X.; Liu, Y.; Qiu, W.; Zhu, D., Immobilization of Tetra-tert-butylphthalocyanines on Carbon Nanotubes: A First Step Towards the Development of New Nanomaterials. *J. Mater. Chem.* **2002,** *12*, 1636-1639.

24. Binnig, G.; Quate, C. F.; Gerber, C., Atomic Force Microscope. *Phys. Rev. Lett.* **1986,** *56*, 930.

25. Goldstein, J. I.; Newbury, D. E.; Michael, J. R.; Ritchie, N. W. M.; Scott, J. H. J.; Joy, D. C., *Scanning Electron Microscopy and X-ray Microanalysis*. Springer: **2017**.

26. Williams, D. B.; Carter, C. B., The Transmission Electron Microscope. In *Transmission electron microscopy*, Springer: **1996**; pp 3-17.

27. Eaton, P.; West, P., *Atomic Force Microscopy*. Oxford University Press: **2010**.

28. Blanchard, C. R., Atomic Force Microscopy. *Chem. Educ.* **1996,** *1*, 1-8.

29. Binnig, G.; Rohrer, H.; Gerber, C.; Weibel, E., Surface Studies by Scanning Tunneling Microscopy. *Phys. Rev. Lett.* **1982,** *49*, 57.

30. Binnig, G.; Rohrer, H., Scanning Tunneling Microscopy. *Surf. Sci.* **1983,** *126*, 236-244.

31. Jalili, N.; Laxminarayana, K., A Review of Atomic Force Microscopy Imaging Systems: Application to Molecular Metrology and Biological Sciences. *Mechatronics* **2004,** *14*, 907-945.

32. Lin, C.-J.; Yang, S.-R., Precise Positioning of Piezo-actuated Stages Using Hysteresis-observer Based Control. *Mechatronics* **2006,** *16*, 417-426.

33. Baró, A. M.; Reifenberger, R. G., *Atomic Force Microscopy in Liquid: Biological Applications*. John Wiley & Sons: **2012**.

34. Giessibl, F. J., Advances in Atomic Force Microscopy. *Rev. Mod. Phys.* **2003,** *75*, 949.

35. Magonov, S. N.; Whangbo, M.-H., *Surface Analysis with STM and AFM: Experimental and Theoretical Aspects of Image Analysis*. John Wiley & Sons: **2008**.

36. Hanley, S. J.; Gray, D. G., *Atomic Force Microscopy*. CRC Press, Inc. Boca Raton, Fl: **1995**.

37. Cuenot, S.; Frétigny, C.; Demoustier-Champagne, S.; Nysten, B., Surface Tension Effect on the Mechanical Properties of Nanomaterials Measured by Atomic Force Microscopy. *Phys. Rev. B* **2004,** *69*, 165410.

38. Jing, G. Y.; Duan, H. L.; Sun, X. M.; Zhang, Z. S.; Xu, J.; Li, Y. D.; Wang, J. X.; Yu, D. P., Surface Effects on Elastic Properties of Silver Nanowires: Contact Atomic-Force Microscopy. *Phys. Rev. B* **2006,** *73*, 235409.

39. Kis, A. s.; Mihailovic, D.; Remskar, M.; Mrzel, A.; Jesih, A.; Piwonski, I.; Kulik, A. J.; Benoît, W.; Forró, L. s., Shear and Young's Moduli of MoS2 Nanotube Ropes. *Adv. Mater.* **2003,** *15*, 733-736.

40. Hansma, H. G.; Laney, D. E.; Bezanilla, M.; Sinsheimer, R. L.; Hansma, P. K., Applications for Atomic Force Microscopy of DNA. *Biophys. J.* **1995,** *68*, 1672-1677.

41. Liu, H.; Wen, J.; Xiao, Y.; Liu, J.; Hopyan, S.; Radisic, M.; Simmons, C. A.; Sun, Y., In situ mechanical characterization of the cell nucleus by atomic force microscopy. *ACS nano* **2014,** *8*, 3821-3828.

42. Haase, K.; Pelling, A. E., Investigating Cell Mechanics with Atomic Force Microscopy. *J. Royal Soc. Interface* **2015,** *12*, 20140970.

43. Giessibl, F. J.; Bielefeldt, H.; Hembacher, S.; Mannhart, J., Calculation of the Optimal Imaging Parameters for Frequency Modulation Atomic Force Microscopy. *Appl. Surf. Sci.* **1999,** *140*, 352-357.

44. Giessibl, F. J., Atomic Resolution on Si (111)-(7× 7) by Noncontact Atomic Force Microscopy with A Force Sensor Based on A Quartz Tuning Fork. *Appl. Phys. Lett.* **2000,** *76*, 1470-1472.

45. Kitamura, S.-i.; Iwatsuki, M., Observation of 7× 7 reconstructed structure on the silicon (111) surface using ultrahigh vacuum noncontact atomic force microscopy. *Japanese journal of applied physics* **1995,** *34*, L145.

46. Uchihashi, T.; Sugawara, Y.; Tsukamoto, T.; Ohta, M.; Morita, S.; Suzuki, M., Role of A Covalent Bonding Interaction in Noncontact-mode Atomic-Force Microscopy on Si (111) 7× 7. *Phys. Rev. B* **1997,** *56*, 9834.

47. Bowen, W. R.; Hilal, N.; Lovitt, R. W.; Williams, P. M., Visualisation of An Ultrafiltration Membrane by Non-contact Atomic Force Microscopy at Single Pore Resolution. *J. Membr. Sci.* **1996,** *110*, 229-232.

48. Singh, S.; Khulbe, K. C.; Matsuura, T.; Ramamurthy, P., Membrane Characterization by Solute Transport and Atomic Force Microscopy. *J. Membr. Sci.* **1998,** *142*, 111-127.

49. Maeda, Y.; Matsumoto, T.; Kawai, T., Observation of Single-and Double-stranded DNA Using Non-contact Atomic Force Microscopy. *Appl. Surf. Sci.* **1999,** *140*, 400-405.

50. Braet, F.; de Zanger, R.; Seynaeve, C.; Baekeland, M.; Wisse, E., A Comparative Atomic Force Microscopy Study on Living Skin Fibroblasts and Liver Endothelial Cells. *Microscopy* **2001,** *50*, 283-290.

51. Garcıa, R.; Perez, R., Dynamic Atomic Force Microscopy Methods. *Surf. Sci. Rep.* **2002,** *47*, 197-301.

52. Ho, H.; West, P., Optimizing AC-mode Atomic Force Microscope Imaging. *Scanning: J. Scanning Microsc.* **1996,** *18*, 339-343.

53. Giessibl, F. J.; Hembacher, S.; Bielefeldt, H.; Mannhart, J., Subatomic Features on the Silicon (111)-(7× 7) Surface Observed by Atomic Force Microscopy. *Science* **2000,** *289*, 422-425.

54. Drolle, E.; Hane, F.; Lee, B.; Leonenko, Z., Atomic Force Microscopy to Study Molecular Mechanisms of Amyloid Fibril Formation and Toxicity in Alzheimer's Disease. *Drug Metab. Rev.* **2014,** *46*, 207-223.

55. Hilal, N.; Al-Zoubi, H.; Darwish, N. A.; Mohamma, A. W.; Arabi, M. A., A Comprehensive Review of Nanofiltration Membranes: Treatment, Pretreatment, Modelling, and Atomic Force Microscopy. *Desalination* **2004,** *170*, 281-308.

56. Johnson, D.; Hilal, N., Characterisation and Quantification of Membrane Surface Properties Using Atomic Force Microscopy: A Comprehensive Review. *Desalination* **2015,** *356*, 149-164.

57. Dufrêne, Y. F.; Ando, T.; Garcia, R.; Alsteens, D.; Martinez-Martin, D.; Engel, A.; Gerber, C.; Müller, D. J., Imaging Modes of Atomic Force Microscopy for Application in Molecular and Cell Biology. *Nat. Nanotechnol.* **2017,** *12*, 295.

58. Pillet, F.; Chopinet, L.; Formosa, C.; Dague, É., Atomic Force Microscopy and Pharmacology: From Microbiology to Cancerology. *Biochim. Biophys. Acta, Gen. Subj.* **2014,** *1840*, 1028-1050.

59. Dufrêne, Y. F., Atomic Force Microscopy, A Powerful Tool in Microbiology. *J. Bacteriol.* **2002,** *184*, 5205-5213.

60. Giessibl, F. J., Atomic Resolution of the Silicon (111)-(7x7) Surface by Atomic Force Microscopy. *Science* **1995,** *267*, 68-71.

61. Kaneko, K., Determination of Pore Size and Pore Size Distribution: 1. Adsorbents and Catalysts. *J. Membr. Sci.* **1994,** *96*, 59-89.

62. Khayet, M.; Feng, C. Y.; Khulbe, K. C.; Matsuura, T., Preparation and Characterization of Polyvinylidene Fluoride Hollow Fiber Membranes for Ultrafiltration. *Polymer* **2002,** *43*, 3879-3890.

63. Kochkodan, V.; Johnson, D. J.; Hilal, N., Polymeric Membranes: Surface Modification for Minimizing (Bio) Colloidal Fouling. *Adv. Colloid Interface Sci.* **2014,** *206*, 116-140.

64. Francis, L. W.; Lewis, P. D.; Wright, C. J.; Conlan, R. S., Atomic force microscopy comes of age. *Biol. Cell* **2010,** *102*, 133-143.

65. Kalle, W.; Strappe, P., Atomic force microscopy on chromosomes, chromatin and DNA: a review. *Micron* **2012,** *43*, 1224-1231.

66. Lyubchenko, Y. L.; Shlyakhtenko, L. S., AFM for analysis of structure and dynamics of DNA and protein–DNA complexes. *Methods* **2009,** *47*, 206-213.

67. Lyubchenko, Y. L.; Shlyakhtenko, L. S.; Ando, T., Imaging of Nucleic Acids with Atomic Force Microscopy. *Methods* **2011,** *54*, 274-283.

68. Leung, C.; Bestembayeva, A.; Thorogate, R.; Stinson, J.; Pyne, A.; Marcovich, C.; Yang, J.; Drechsler, U.; Despont, M.; Jankowski, T., Atomic Force Microscopy with Nanoscale Cantilevers Resolves Different Structural Conformations of the DNA Double Helix. *Nano Lett.* **2012,** *12*, 3846-3850.

69. Lyubchenko, Y. L.; Shlyakhtenko, L. S., Visualization of Supercoiled DNA with Atomic Force Microscopy In situ. *Proc. Nat. Acad. Sci.* **1997,** *94*, 496-501.

70. Hansma, H. G.; Oroudjev, E.; Baudrey, S.; Jaeger, L., TectoRNA and 'Kissing-loop'RNA: Atomic Force Microscopy of Self-assembling RNA Structures. *J. Microsc.* **2003,** *212*, 273-279.

71. Grooth, B. G. D.; Putman, C. A. J., High-resolution Imaging of Chromosome-related Structures by Atomic Force Microscopy. *J. Microsc.* **1992,** *168*, 239-247.

72. Ando, T., High-speed Atomic Force Microscopy Coming of Age. *Nanotechnology* **2012,** *23*, 062001.

73. Gutsmann, T.; Fantner, G. E.; Kindt, J. H.; Venturoni, M.; Danielsen, S.; Hansma, P. K., Force Spectroscopy of Collagen Fibers to Investigate Their Mechanical Properties and Structural Organization. *Biophys. J.* **2004,** *86*, 3186-3193.

74. De Oliveira, R. R. L.; Albuquerque, D. A. C.; Cruz, T. G. S.; Yamaji, F. M.; Leite, F. L., Measurement of the Nanoscale Roughness by Atomic Force Microscopy: Basic Principles and Applications. In *Atomic force microscopy-imaging, measuring and manipulating surfaces at the atomic scale*, InTech: **2012**.

75. Edward, T. Y., Nanoscale Characterization of Semiconductor Materials and Devices Using Scanning Probe Techniques. *Mater. Sci. Eng. R Rep.* **1996,** *17*, 147-206.

76. Koh, J.; Lu, Y.; Wronski, C. R.; Kuang, Y.; Collins, R. W.; Tsong, T. T.; Strausser, Y. E., Correlation of Real Time Spectroellipsometry and Atomic Force Microscopy Measurements of Surface Roughness on Amorphous Semiconductor Thin Films. *Appl. Phys. Lett.* **1996,** *69*, 1297-1299.

77. Cacciafesta, P.; Hallam, K. R.; Oyedepo, C. A.; Humphris, A. D. L.; Miles, M. J.; Jandt, K. D., Characterization of Ultraflat Titanium Oxide Surfaces. *Chem. Mater.* **2002,** *14*, 777-789.

78. Cai, K.; Müller, M.; Bossert, J.; Rechtenbach, A.; Jandt, K. D., Surface Structure and Composition of Flat Titanium Thin Films As A Function of Film Thickness and Evaporation Rate. *Appl. Surf. Sci.* **2005,** *250*, 252-267.

79. Shellenberger, K.; Logan, B. E., Effect of Molecular Scale Roughness of Glass Beads on Colloidal and Bacterial Deposition. *Environ. Sci. Technol.* **2002,** *36*, 184-189.

80. Tholt, B.; Miranda-Júnior, W. G.; Prioli, R.; Thompson, J.; Oda, M., Surface Roughness in Cramics with Different Finishing Techniques Using Atomic Force Microscope and Profilometer. *Oper. Dent.* **2006,** *31*, 442-449.

81. Bowen, W. R.; Doneva, T. A., Atomic Force Microscopy Studies of Membranes: Effect of Surface Roughness on Double-layer Interactions and Particle Adhesion. *J. Colloid Interface Sci.* **2000,** *229*, 544-549.

82. Miller, J. D.; Veeramasuneni, S.; Drelich, J.; Yalamanchili, M. R.; Yamauchi, G., Effect of Roughness As Determined by Atomic Force Microscopy on the Wetting Properties of PTFE Thin Films. *Polym. Eng. Sci.* **1996,** *36*, 1849-1855.

83. Walther, F.; Heckl, W. M.; Stark, R. W., Evaluation of Nanoscale Roughness Measurements on A Plasma Treated SU-8 Polymer Surface by Atomic Force Microscopy. *Appl. Surf. Sci.* **2008,** *254*, 7290-7295.

84. Girasole, M.; Pompeo, G.; Cricenti, A.; Congiu-Castellano, A.; Andreola, F.; Serafino, A.; Frazer, B. H.; Boumis, G.; Amiconi, G., Roughness of the Plasma Membrane As An Independent Morphological Parameter to Study RBCs: A Quantitative Atomic Force Microscopy Investigation. *Biochim. Biophys. Acta, Biomembr.* **2007,** *1768*, 1268-1276.

85. Girasole, M.; Pompeo, G.; Cricenti, A.; Longo, G.; Boumis, G.; Bellelli, A.; Amiconi, S., The How, When, and Why of the Aging Signals Appearing on the Human Erythrocyte Membrane: An Atomic Force Microscopy Study of Surface Roughness. *Nanomedicine* **2010,** *6*, 760-768.

86. Hues, S. M.; Draper, C. F.; Colton, R. J., Measurement of Nanomechanical Properties of Metals Using the Atomic Force Microscope. *J. Vac. Sci. Technol. B Microelectron. Nanometer Struct. Process. Meas. Phenom.* **1994,** *12*, 2211-2214.

87. Bischel, M. S.; Vanlandingham, M. R.; Eduljee, R. F.; Gillespie, J. W.; Schultz, J. M., On the Use of Nanoscale Indentation with the AFM in the Identification of Phases in Blends of Linear Low Density Polyethylene and High Density Polyethylene. *J. Mater. Sci.* **2000,** *35*, 221-228.

88. Kuznetsova, T. G.; Starodubtseva, M. N.; Yegorenkov, N. I.; Chizhik, S. A.; Zhdanov, R. I., Atomic Force Microscopy Probing of Cell Elasticity. *Micron* **2007,** *38*, 824-833.

89. Vinckier, A.; Semenza, G., Measuring Elasticity of Biological Materials by Atomic Force Microscopy. *FEBS Lett.* **1998,** *430*, 12-16.

90. Borgia, A.; Williams, P. M.; Clarke, J., Single-molecule Studies of Protein Folding. *Annu. Rev. Biochem.* **2008,** *77*, 101-125.

91. Bustamante, C.; Smith, S. B.; Liphardt, J.; Smith, D., Single-molecule Studies of DNA Mechanics. *Curr. Opin. Struct. Biol.* **2000,** *10*, 279-285.

92. Scholl, Z. N.; Li, Q.; Marszalek, P. E., Single Molecule Mechanical Manipulation for Studying Biological Properties of Proteins, DNA, and Sugars. *Wiley Interdiscip. Rev. Nanomed. Nanobiotechnol.* **2014,** *6*, 211-229.

93. Herrero-Galán, E.; Fuentes-Perez, M. E.; Carrasco, C.; Valpuesta, J. M.; Carrascosa, J. L.; Moreno-Herrero, F.; Arias-Gonzalez, J. R., Mechanical Identities of RNA and DNA Double Helices Unveiled at the Single-molecule Level. *J. Am. Chem. Soc.* **2012,** *135*, 122-131.

94. Rief, M.; Clausen-Schaumann, H.; Gaub, H. E., Sequence-dependent Mechanics of Single DNA Molecules. *Nat. Struct. Mol. Biol.* **1999,** *6*, 346.

95. Santos, N. C.; Castanho, M. A. R. B., An Overview of the Biophysical Applications of Atomic Force Microscopy. *Biophys. Chem.* **2004,** *107*, 133-149.

96. Thalhammer, S.; Stark, R. W.; Müller, S.; Wienberg, J.; Heckl, W. M., The Atomic Force Microscope As A New Microdissecting Tool for the Generation of Genetic Probes. *J. Struct. Biol.* **1997,** *119*, 232-237.

97. Xie, X. N.; Chung, H. J.; Sow, C. H.; Wee, A. T. S., Nanoscale Materials Patterning and Engineering by Atomic Force Microscopy Nanolithography. *Mater. Sci. Eng. R Rep.* **2006,** *54*, 1-48.

98. Geisler, B.; Noll, F.; Hampp, N., Nanodissection and Noncontact Imaging of Plasmid DNA with An Atomic Force Microscope. *Scanning* **2000,** *22*, 7-11.

99. Hansma, H. G.; Vesenka, J.; Siegerist, C.; Kelderman, G.; Morrett, H.; Sinsheimer, R. L.; Elings, V.; Bustamante, C.; Hansma, P. K., Reproducible Imaging and Dissection of Plasmid DNA Under Liquid with The Atomic Force Microscope. *Science* **1992,** *256*, 1180-1184.

100. Henderson, E., Imaging and Nanodissection of Individual Supercoiled Plasmids by Atomic Force Microscopy. *Nucleic Acids Res.* **1992,** *20*, 445-447.

101. Saito, M.; Nakagawa, K.; Yamanaka, K.; Takamura, Y.; Hashiguchi, G.; Tamiya, E., A New Design of Knife-edged AFM Probe for Chromosome Precision Manipulating. *Sensors and Actuators A: Physical* **2006,** *130*, 616-624.

102. Kim, D.-H.; Koo, J.-Y.; Kim, J.-J., Cutting of Multiwalled Carbon Nanotubes by A Negative Voltage Tip of An Atomic Force Microscope: A Possible Mechanism. *Phys. Rev. B* **2003,** *68*, 113406.

103. Park, J.-Y.; Yaish, Y.; Brink, M.; Rosenblatt, S.; McEuen, P. L., Electrical Cutting and Nicking of Carbon Nanotubes Using An Atomic Force Microscope. *Appl. Phys. Lett.* **2002,** *80*, 4446-4448.

104. Decossas, S.; Patrone, L.; Bonnot, A. M.; Comin, F.; Derivaz, M.; Barski, A.; Chevrier, J., Nanomanipulation by Atomic Force Microscopy of Carbon Nanotubes on A Nanostructured Surface. *Surf. Sci.* **2003,** *543*, 57-62.

105. Harel, E.; Meltzer, S. E.; Requicha, A. A. G.; Thompson, M. E.; Koel, B. E., Fabrication of Polystyrene Latex Nanostructures by Nanomanipulation and Thermal Processing. *Nano Lett.* **2005,** *5*, 2624-2629.

106. Hsieh, S.; Meltzer, S.; Wang, C. R. C.; Requicha, A. A. G.; Thompson, M. E.; Koel, B. E., Imaging and Manipulation of Gold Nanorods with An Atomic Force Microscope. *J. Phys. Chem. B* **2002,** *106*, 231-234.

107. Junno, T.; Deppert, K.; Montelius, L.; Samuelson, L., Controlled Manipulation of Nanoparticles with An Atomic Force Microscope. *Appl. Phys. Lett.* **1995,** *66*, 3627-3629.

108. Falvo, M. R.; Taylor Ii, R. M.; Helser, A.; Chi, V.; Brooks Jr, F. P.; Washburn, S.; Superfine, R., Nanometre-scale Rolling and Sliding of Carbon Nanotubes. *Nature* **1999,** *397*, 236.

109. Chan, H.-Y.; Xi, N.; Zhang, J.; Li, G. In *A Deterministic Process for Fabrication and Assembly of Single Carbon Nanotube Based Devices*, 5th IEEE Conference on Nanotechnology, IEEE: **2005**; pp 713-716.

110. Meltzer, S.; Resch, R.; Koel, B. E.; Thompson, M. E.; Madhukar, A.; Requicha, A. A. G.; Will, P., Fabrication of Nanostructures by Hydroxylamine Seeding of Gold Nanoparticle Templates. *Langmuir* **2001,** *17*, 1713-1718.

111. Lü, J. H., Nanomanipulation of Extended Single-DNA Molecules on Modified Mica Surfaces Using the Atomic Force Microscopy. *Colloids Surf. B Biointerfaces* **2004,** *39*, 177-180.

112. An, H.; Huang, J.; Lü, M.; Li, X.; Lü, J.; Li, H.; Zhang, Y.; Li, M.; Hu, J., Single-base Resolution and Long-coverage Sequencing Based on Single-molecule Nanomanipulation. *Nanotechnology* **2007,** *18*, 225101.

113. Lü, J.-h.; Li, H.-k.; An, H.-j.; Wang, G.-h.; Wang, Y.; Li, M.-q.; Zhang, Y.; Hu, J., Positioning Isolation and Biochemical Analysis of Single DNA Molecules Based on Nanomanipulation and Single-molecule PCR. *J. Am. Chem. Soc.* **2004,** *126*, 11136-11137.

114. Xu, X.-M.; Ikai, A., Recovery and Amplification of Plasmid DNA with Atomic Force Microscopy and the Polymerase Chain Reaction. *Anal. Chim. Acta* **1998,** *361*, 1-7.

115. Yamanaka, K.; Saito, M.; Shichiri, M.; Sugiyama, S.; Takamura, Y.; Hashiguchi, G.; Tamiya, E., AFM picking-up manipulation of the metaphase chromosome fragment by using the tweezers-type probe. *Ultramicroscopy* **2008,** *108*, 847-854.

116. Xie, H.; Haliyo, D. S.; Régnier, S., A Versatile Atomic Force Microscope for Three-dimensional Nanomanipulation and Nanoassembly. *Nanotechnology* **2009,** *20*, 215301.

117. Parot, P.; Dufrêne, Y. F.; Hinterdorfer, P.; Le Grimellec, C.; Navajas, D.; Pellequer, J. L.; Scheuring, S., Past, Present and Future of Atomic Force Microscopy in Life Sciences and Medicine. *J. Mol. Recognit.* **2007,** *20*, 418-431.

118. Tang, Q.; Shi, S.-Q.; Zhou, L., Nanofabrication with Atomic Force Microscopy. *J. Nanosci. Nanotechnol* **2004,** *4*, 948-963.

119. DeRose, J. A.; Revel, J. P., Examination of Atomic (Scanning) Force Microscopy Probe Tips with the Transmission Electron Microscope. *Microsc. Microanal.* **1997,** *3*, 203-213.

120. Abdelhady, H. G.; Allen, S.; Ebbens, S. J.; Madden, C.; Patel, N.; Roberts, C. J.; Zhang, J., Towards Nanoscale Metrology for Biomolecular Imaging by Atomic Force Microscopy. *Nanotechnology* **2005,** *16*, 966.

121. Vallieres, K.; Chevallier, P.; Sarra-Bournet, C.; Turgeon, S.; Laroche, G., AFM Imaging of Immobilized Fibronectin: Does the Surface Conjugation Scheme Affect the Protein Orientation/Conformation? *Langmuir* **2007,** *23*, 9745-9751.

122. Chen, Y.; Cai, J.; Liu, M.; Zeng, G.; Feng, Q.; Chen, Z., Research on Double-probe, Double-and Triple-tip Effects During Atomic Force Microscopy Scanning. *Scanning: J. Scanning Microsc.* **2004,** *26*, 155-161.

123. Taatjes, D. J.; Quinn, A. S.; Lewis, M. R.; Bovill, E. G., Quality Assessment of Atomic Force Microscopy Probes by Scanning Electron Microscopy: Correlation of Tip Structure with Rendered Images. *Microsc. Res. Tech.* **1999,** *44*, 312-326.

124. Gross, L.; Mohn, F.; Moll, N.; Liljeroth, P.; Meyer, G., The Chemical Structure of A Molecule Resolved by Atomic Force Microscopy. *Science* **2009,** *325*, 1110-1114.

125. Boneschanscher, M. P.; Van Der Lit, J.; Sun, Z.; Swart, I.; Liljeroth, P.; Vanmaekelbergh, D., Quantitative Atomic Resolution Force Imaging on Epitaxial Graphene with Reactive and Nonreactive AFM Probes. *ACS Nano* **2012,** *6*, 10216-10221.

126. Chiutu, C.; Sweetman, A. M.; Lakin, A. J.; Stannard, A.; Jarvis, S.; Kantorovich, L.; Dunn, J. L.; Moriarty, P., Precise Orientation of A Single C 60 Molecule on the Tip of A Scanning Probe Microscope. *Phys. Rev. Lett.* **2012,** *108*, 268302.

127. Pawlak, R.; Kawai, S.; Fremy, S.; Glatzel, T.; Meyer, E., Atomic-scale Mechanical Properties of Orientated C60 Molecules Revealed by Noncontact Atomic Force Microscopy. *ACS Nano* **2011,** *5*, 6349-6354.

128. Zenobi, R., Analytical Tools for the Nano World. *Anal. Bioanal. Chem.* **2008,** *390*, 215-221.

129. Tamayo, J.; Garcia, R., Deformation, Contact time, and Phase Contrast in Tapping Mode Scanning Force Microscopy. *Langmuir* **1996,** *12*, 4430-4435.

130. Garcia, R.; Gómez, C. J.; Martinez, N. F.; Patil, S.; Dietz, C.; Magerle, R., Identification of Nanoscale Dissipation Processes by Dynamic Atomic Force Microscopy. *Phys. Rev. Lett.* **2006,** *97*, 016103.

131. Hartmann, U., Magnetic Force Microscopy. *Annu. Rev. Mater. Sci.* **1999,** *29*, 53-87.

132. Nonnenmacher, M.; o'Boyle, M. P.; Wickramasinghe, H. K., Kelvin Probe Force Microscopy. *Appl. Phys. Lett.* **1991,** *58*, 2921-2923.

133. Price, D. M.; Reading, M.; Hammiche, A.; Pollock, H. M., Micro-thermal Analysis: Scanning Thermal Microscopy and Localised Thermal Analysis. *Int. J. Pharm.* **1999,** *192*, 85-96.

134. Lipson, A.; Lipson, S. G.; Lipson, H., *Optical Physics*. Cambridge University Press: 2010.

135. Synge, E., A Suggested Method for Extending Microscopic Resolution into the Ultra-microscopic Region. *Lond. Edinb. Dubl. Phil. Mag.* **1928,** *6*, 356-362.

136. Pohl, D. W.; Denk, W.; Lanz, M., Optical Stethoscopy: Image Recording with Resolution λ/20. *Appl. Phys. Lett.* **1984,** *44*, 651-653.

137. Lewis, A.; Isaacson, M.; Harootunian, A.; Muray, A., Development of A 500 Å Spatial Resolution Light Microscope: I. Light Is Efficiently Transmitted Through λ/16 Diameter Apertures. *Ultramicroscopy* **1984,** *13*, 227-231.

138. Dunn, R. C., Near-field Scanning Optical Microscopy. *Chem. Rev.* **1999,** *99*, 2891-2928.

139. Martin, Y. C.; Hamann, H. F.; Wickramasinghe, H. K., Strength of the Electric Field in Apertureless Near-field Optical Microscopy. *J. Appl. Phys.* **2001,** *89*, 5774-5778.

140. Hartschuh, A., Tip-enhanced Near-field Optical Microscopy. *Angew. Chem., Int. Ed.* **2008,** *47*, 8178-8191.

141. Mauser, N.; Hartschuh, A., Tip-enhanced Near-field Optical Microscopy. *Chem. Soc. Rev.* **2014,** *43*, 1248-1262.

142. Tseng, A. A., Recent developments in nanofabrication using scanning near-field optical microscope lithography. *Opt. Laser Technol.* **2007,** *39*, 514-526.

143. Elfick, A. P. D.; Downes, A. R.; Mouras, R., Development of Tip-enhanced Optical Spectroscopy for Biological Applications: A Review. *Anal. Bioanal. Chem.* **2010,** *396*, 45-52.

144. Novotny, L., The history of near-field optics. *Prog. Optics* **2007,** *50*, 137.

145. Rasmussen, A.; Deckert, V., New dimension in nano-imaging: breaking through the diffraction limit with scanning near-field optical microscopy. *Anal. Bioanal. Chem.* **2005,** *381*, 165-172.

146. Pettinger, B.; Schambach, P.; Villagómez, C. J.; Scott, N., Tip-enhanced Raman Spectroscopy: Near-fields Acting on A Few Molecules. *Annual review of physical chemistry* **2012,** *63*, 379-399.

147. Schmid, T.; Opilik, L.; Blum, C.; Zenobi, R., Nanoscale Chemical Imaging Using Tip-enhanced Raman Spectroscopy: A Critical Review. *Angew. Chem., Int. Ed.* **2013,** *52*, 5940-5954.

148. Sonntag, M. D.; Pozzi, E. A.; Jiang, N.; Hersam, M. C.; Van Duyne, R. P., Recent Advances in Tip-enhanced Raman Spectroscopy. *J. Phys. Chem. Lett.* **2014,** *5*, 3125-3130.

149. Zhang, Z.; Sheng, S.; Wang, R.; Sun, M., Tip-enhanced Raman Spectroscopy. *Anal. Chem.* **2016,** *88*, 9328-9346.

150. Amrania, H.; Drummond, L.; Coombes, R. C.; Shousha, S.; Woodley-Barker, L.; Weir, K.; Hart, W.; Carter, I.; Phillips, C. C., New IR Imaging Modalities for Cancer Detection and for Intra-cell Chemical Mapping with A Sub-diffraction Mid-IR s-SNOM. *Faraday Discuss.* **2016,** *187*, 539-553.

151. Dazzi, A.; Prater, C. B., AFM-IR: Technology and Applications in Nanoscale Infrared Spectroscopy and Chemical Imaging. *Chem. Rev.* **2016,** *117*, 5146-5173.

152. Dazzi, A.; Prater, C. B.; Hu, Q.; Chase, D. B.; Rabolt, J. F.; Marcott, C., AFM-IR: combining atomic force microscopy and infrared spectroscopy for nanoscale chemical characterization. *Appl. Spectrosc.* **2012,** *66*, 1365-1384.

153. Dazzi, A.; Saunier, J.; Kjoller, K.; Yagoubi, N., Resonance Enhanced AFM-IR: A New Powerful Way to Characterize Blooming on Polymers Used in Medical Devices. *Int. J. Pharm.* **2015,** *484*, 109-114.

154. Fort, E.; Grésillon, S., Surface Enhanced Fluorescence. *J. Phys. D: Appl. Phys.* **2007,** *41*, 013001.

155. Gerton, J. M.; Wade, L. A.; Lessard, G. A.; Ma, Z.; Quake, S. R., Tip-enhanced Fluorescence Microscopy at 10 Nanometer Resolution. *Phys. Rev. Lett.* **2004,** *93*, 180801.

156. Wessel, J., Surface-enhanced Optical Microscopy. *J. Opt. Soc. Am. B* **1985,** *2*, 1538-1541.

157. Anderson, M. S., Locally Enhanced Raman Spectroscopy with An Atomic Force Microscope. *Appl. Phys. Lett.* **2000,** *76*, 3130-3132.

158. Hayazawa, N.; Inouye, Y.; Sekkat, Z.; Kawata, S., Metallized Tip Amplification of Near-field Raman Scattering. *Opt. Commun.* **2000,** *183*, 333-336.

159. Pettinger, B.; Picardi, G.; Schuster, R.; Ertl, G., Surface Enhanced Raman Spectroscopy: Towards Single Molecular Spectroscopy. *Electrochemistry* **2000,** *68*, 942-949.

160. Stöckle, R. M.; Suh, Y. D.; Deckert, V.; Zenobi, R., Nanoscale Chemical Analysis by Tip-enhanced Raman Spectroscopy. *Chem. Phys. Lett.* **2000,** *318*, 131-136.

161. Anderson, N.; Hartschuh, A.; Cronin, S.; Novotny, L., Nanoscale Vibrational Analysis of Single-walled Carbon Nanotubes. *J. Am. Chem. Soc.* **2005,** *127*, 2533-2537.

162. Chen, C.; Hayazawa, N.; Kawata, S., A 1.7 nm Resolution Chemical Analysis of Carbon Nanotubes by Tip-enhanced Raman Imaging in the Ambient. *Nat. Commun.* **2014,** *5*, 3312.

163. Stadler, J.; Schmid, T.; Zenobi, R., Nanoscale Chemical Imaging of Single-layer Graphene. *ACS Nano* **2011,** *5*, 8442-8448.

164. Lucas, M.; Riedo, E., Invited Review Article: Combining Scanning Probe Microscopy with Optical Spectroscopy for Applications in Biology and Materials Science. *Rev. Sci. Instrum.* **2012,** *83*, 061101.

165. Wood, B. R.; Asghari-Khiavi, M.; Bailo, E.; McNaughton, D.; Deckert, V., Detection of Nano-oxidation Sites on the Surface of Hemoglobin Crystals Using Tip-enhanced Raman Scattering. *Nano Lett.* **2012,** *12*, 1555-1560.

166. Yeo, B.-S.; Stadler, J.; Schmid, T.; Zenobi, R.; Zhang, W., Tip-enhanced Raman Spectroscopy–Its status, Challenges and Future Directions. *Chem. Phys. Lett.* **2009,** *472*, 1-13.

167. Bailo, E.; Deckert, V., Tip-enhanced Raman spectroscopy of single RNA strands: towards a novel direct-sequencing method. *Angew. Chem. Int. Ed.* **2008,** *47*, 1658-1661.

168. Hu, D.; Micic, M.; Klymyshyn, N.; Suh, Y. D.; Lu, H. P., Correlated Topographic and Spectroscopic Imaging Beyond Diffraction Limit by Atomic Force Microscopy Metallic Tip-enhanced Near-field Fluorescence Lifetime Microscopy. *Rev. Sci. Instrum.* **2003,** *74*, 3347-3355.

169. Böhmler, M.; Wang, Z.; Myalitsin, A.; Mews, A.; Hartschuh, A., Optical Imaging of CdSe Nanowires with Nanoscale Resolution. *Angew. Chem., Int. Ed.* **2011,** *50*, 11536-11538.

170. Zhang, D.; Heinemeyer, U.; Stanciu, C.; Sackrow, M.; Braun, K.; Hennemann, L. E.; Wang, X.; Scholz, R.; Schreiber, F.; Meixner, A. J., Nanoscale Spectroscopic Imaging of Organic Semiconductor Films by Plasmon-polariton Coupling. *Phys. Rev. Lett.* **2010,** *104*, 056601.

171. Qian, H.; Araujo, P. T.; Georgi, C.; Gokus, T.; Hartmann, N.; Green, A. A.; Jorio, A.; Hersam, M. C.; Novotny, L.; Hartschuh, A., Visualizing the local optical response of semiconducting carbon nanotubes to DNA-wrapping. *Nano Lett.* **2008,** *8*, 2706-2711.

172. Fernandez, D. C.; Bhargava, R.; Hewitt, S. M.; Levin, I. W., Infrared Spectroscopic Imaging for Histopathologic Recognition. *Nat. Biotechnol.* **2005,** *23*, 469.

173. Centrone, A., Infrared imaging and spectroscopy beyond the diffraction limit. *Annu. Rev. Anal. Chem.* **2015,** *8*, 101-126.

174. De Angelis, F.; Das, G.; Candeloro, P.; Patrini, M.; Galli, M.; Bek, A.; Lazzarino, M.; Maksymov, I.; Liberale, C.; Andreani, L. C., Nanoscale Chemical Mapping Using Three-dimensional Adiabatic Compression of Surface Plasmon Polaritons. *Nat. Nanotechnol.* **2010,** *5*, 67.

175. Westermeier, C.; Cernescu, A.; Amarie, S.; Liewald, C.; Keilmann, F.; Nickel, B., Sub-micron Phase Coexistence in Small-molecule Organic Thin Films Revealed by Infrared Nano-imaging. *Nat. Commun.* **2014,** *5*, 4101.

176. Chen, J.; Nesterov, M. L.; Nikitin, A. Y.; Thongrattanasiri, S.; Alonso-González, P.; Slipchenko, T. M.; Speck, F.; Ostler, M.; Seyller, T.; Crassee, I., Strong Plasmon Reflection at Nanometer-size Gaps in Monolayer Graphene on SiC. *Nano Lett.* **2013,** *13*, 6210-6215.

177. Fei, Z.; Rodin, A. S.; Gannett, W.; Dai, S.; Regan, W.; Wagner, M.; Liu, M. K.; McLeod, A. S.; Dominguez, G.; Thiemens, M., Electronic and Plasmonic Phenomena at Graphene Grain Boundaries. *Nat. Nanotechnol.* **2013,** *8*, 821.

178. Amenabar, I.; Poly, S.; Nuansing, W.; Hubrich, E. H.; Govyadinov, A. A.; Huth, F.; Krutokhvostov, R.; Zhang, L.; Knez, M.; Heberle, J., Structural Analysis and Mapping of Individual Protein Complexes by Infrared Nanospectroscopy. *Nat. Commun.* **2013,** *4*, 2890.

179. Berweger, S.; Nguyen, D. M.; Muller, E. A.; Bechtel, H. A.; Perkins, T. T.; Raschke, M. B., Nano-chemical Infrared Imaging of Membrane Proteins in Lipid Bilayers. *J. Am. Chem. Soc.* **2013,** *135*, 18292-18295.

180. Dazzi, A.; Glotin, F.; Carminati, R., Theory of Infrared Nanospectroscopy by Photothermal Induced Resonance. *J. Appl. Phys.* **2010,** *107*, 124519.

181. Houel, J.; Sauvage, S.; Boucaud, P.; Dazzi, A.; Prazeres, R.; Glotin, F.; Ortéga, J.-M.; Miard, A.; Lemaître, A., Ultraweak-absorption Microscopy of A Single Semiconductor Quantum Dot in the Midinfrared Range. *Phys. Rev. Lett.* **2007,** *99*, 217404.

182. Sauvage, S.; Driss, A.; Réveret, F.; Boucaud, P.; Dazzi, A.; Prazeres, R.; Glotin, F.; Ortéga, J. M.; Miard, A.; Halioua, Y., Homogeneous Broadening of the S to P Transition in

InGaAs/GaAs Quantum Dots Measured by Infrared Absorption Imaging with Nanoscale Resolution. *Phys. Rev. B* **2011,** *83*, 035302.

183. Lo, M. K. F.; Dazzi, A.; Marcott, C. A.; Dillon, E.; Hu, Q.; Kjoller, K.; Prater, C. B.; King, S. W., Nanoscale Chemical-Mechanical Characterization of Nanoelectronic Low-k Dielectric/Cu Interconnects. *ECS J. Solid State Sci. Technol.* **2016,** *5*, P3018-P3024.

184. Li, N.; Taylor, L. S., Nanoscale Infrared, Thermal, and Mechanical Characterization of Telaprevir–polymer Miscibility in Amorphous Solid Dispersions Prepared by Solvent Evaporation. *Mol. Pharm.* **2016,** *13*, 1123-1136.

185. Van Eerdenbrugh, B.; Lo, M.; Kjoller, K.; Marcott, C.; Taylor, L. S., Nanoscale Mid-infrared Evaluation of the Miscibility Behavior of Blends of Dextran or Maltodextrin with Poly (vinylpyrrolidone). *Mol. Pharm.* **2012,** *9*, 1459-1469.

186. Baldassarre, L.; Giliberti, V.; Rosa, A.; Ortolani, M.; Bonamore, A.; Baiocco, P.; Kjoller, K.; Calvani, P.; Nucara, A., Mapping the Amide I Absorption in Single Bacteria and Mammalian Cells with Resonant Infrared Nanospectroscopy. *Nanotechnology* **2016,** *27*, 075101.

187. Janik, E.; Bednarska, J.; Zubik, M.; Puzio, M.; Luchowski, R.; Grudzinski, W.; Mazur, R.; Garstka, M.; Maksymiec, W.; Kulik, A., Molecular Architecture of Plant Thylakoids Under Physiological and Light Stress Conditions: A Study of Lipid–light-harvesting Complex II Model Membranes. *Plant Cell* **2013,** tpc-113.

188. Schmid, T.; Schmitz, T. A.; Setz, P. D.; Yeo, B.-S.; Zhang, W.; Zenobi, R., Methods for Molecular Nanoanalysis. *Chimia* **2006,** *60*, 783-788.

189. Meyer, K. A.; Ovchinnikova, O.; Ng, K.; Goeringer, D. E., Development of a scanning surface probe for nanoscale tip-enhanced desorption/ablation. *Rev. Sci. Instrum.* **2008,** *79*, 123710.

190. Miller, J. C.; Haglund, R. F., *Laser Ablation and Desorption*. Elsevier: **1998**; Vol. 30.

191. Hu, H.; Kim, H. J.; Somnath, S., Tip-based nanofabrication for scalable manufacturing. *Micromachines* **2017,** *8*, 90.

192. Cleveland, D.; Michel, R. G., A review of near-field laser ablation for high-resolution nanoscale surface analysis. *Appl. Spectrosc. Rev.* **2008,** *43*, 93-110.

193. Davy, S.; Spajer, M., Near field optics: Snapshot of the field emitted by a nanosource using a photosensitive polymer. *Appl. Phys. Lett.* **1996,** *69*, 3306-3308.

194. Chimmalgi, A.; Choi, T. Y.; Grigoropoulos, C. P.; Komvopoulos, K., Femtosecond laser aperturless near-field nanomachining of metals assisted by scanning probe microscopy. *Appl. Phys. Lett.* **2003,** *82*, 1146-1148.

195. Kirsanov, A.; Kiselev, A.; Stepanov, A.; Polushkin, N., Femtosecond laser-induced nanofabrication in the near-field of atomic force microscope tip. *J. Appl. Phys.* **2003,** *94*, 6822-6826.

196. Adams, R. P.; Sparkman, O. D., Review of Identification of Essential Oil Components by Gas Chromatography/Mass Spectrometry. *J. Am. Soc. Mass Spectrom.* **2007,** *18*, 803-806.

197. Aebersold, R.; Mann, M., Mass Spectrometry-based Proteomics. *Nature* **2003,** *422*, 198.

198. Benson, S.; Lennard, C.; Maynard, P.; Roux, C., Forensic Applications of Isotope Ratio Mass Spectrometry—A Review. *Forensic Sci. Int.* **2006,** *157*, 1-22.

199. Domon, B.; Aebersold, R., Mass Spectrometry and Protein Analysis. *Science* **2006,** *312*, 212-217.

200. Takats, Z.; Wiseman, J. M.; Cooks, R. G., Ambient Mass Spectrometry Using Desorption Electrospray Ionization (DESI): Instrumentation, Mechanisms and Applications in Forensics, Chemistry, and Biology. *J. Mass Spectrom.* **2005,** *40*, 1261-1275.

201. De Hoffmann, E., Mass Spectrometry. *Kirk-Othmer Encyclopedia of Chemical Technology* **2000**.

202. El-Aneed, A.; Cohen, A.; Banoub, J., Mass Spectrometry, Review of the Basics: Electrospray, MALDI, and Commonly Used Mass Analyzers. *Appl. Spectrosc. Rev.* **2009,** *44*, 210-230.

203. Nesvizhskii, A. I.; Keller, A.; Kolker, E.; Aebersold, R., A Statistical Model for Identifying Proteins by Tandem Mass Spectrometry. *Anal. Chem.* **2003,** *75*, 4646-4658.

204. Norris, J. L.; Caprioli, R. M., Analysis of Tissue Specimens by Matrix-assisted Laser Desorption/Ionization Imaging Mass Spectrometry in Biological and Clinical Research. *Chem. Rev.* **2013,** *113*, 2309-2342.

205. Seeley, E. H.; Caprioli, R. M., MALDI Imaging Mass Spectrometry of Human Tissue: Method Challenges and Clinical Perspectives. *Trends Biotechnol.* **2011,** *29*, 136-143.

206. Stoeckli, M.; Chaurand, P.; Hallahan, D. E.; Caprioli, R. M., Imaging Mass Spectrometry: A New Technology for the Analysis of Protein Expression in Mammalian Tissues. *Nat. Med.* **2001,** *7*, 493.

207. Murray, K. K.; Seneviratne, C. A.; Ghorai, S., High resolution laser mass spectrometry bioimaging. *Methods* **2016,** *104*, 118-126.

208. Fletcher, J. S.; Vickerman, J. C., Secondary Ion Mass Spectrometry: Characterizing Complex Samples in Two and Three Dimensions. *Anal. Chem.* **2012,** *85*, 610-639.

209. Bich, C.; Touboul, D.; Brunelle, A., Cluster TOF-SIMS Imaging As A Tool for Micrometric Histology of Lipids in Tissue. *Mass Spectrom. Rev.* **2014,** *33*, 442-451.

210. Vickerman, J. C., Molecular Imaging and Depth Profiling by Mass Spectrometry—SIMS, MALDI or DESI? *Analyst* **2011,** *136*, 2199-2217.

211. Vickerman, J. C.; Winograd, N., SIMS—A Precursor and Partner to Contemporary Mass Spectrometry. *Int. J. Mass Spectrom.* **2015,** *377*, 568-579.

212. Venter, A.; Nefliu, M.; Cooks, R. G., Ambient Desorption Ionization Mass Spectrometry. *Trends Anal. Chem.* **2008,** *27*, 284-290.

213. Ovchinnikova, O. S.; Van Berkel, G. J., Thin-layer Chromatography and Mass Spectrometry Coupled Using Proximal Probe Thermal Desorption with Electrospray or Atmospheric Pressure Chemical Ionization. *Rapid Commun. Mass Spectrom.* **2010,** *24*, 1721-1729.

214. Ovchinnikova, O. S.; Nikiforov, M. P.; Bradshaw, J. A.; Jesse, S.; Van Berkel, G. J., Combined Atomic Force Microscope-based Topographical Imaging and Nanometer-scale Resolved Proximal Probe Thermal Desorption/Electrospray Ionization–Mass Spectrometry. *ACS Nano* **2011,** *5*, 5526-5531.

215. de Koning, S.; Janssen, H.-G.; Udo, A. T., Modern Methods of Sample Preparation for GC Analysis. *Chromatographia* **2009,** *69*, 33.

216. Kossakovski, D. A.; O'Connor, S. D.; Widmer, M.; Baldeschwieler, J. D.; Beauchamp, J. L., Spatially resolved chemical analysis with an NSOM-based laser desorption microprobe. *Ultramicroscopy* **1998,** *71*, 111-115.

217. Stöckle, R.; Setz, P.; Deckert, V.; Lippert, T.; Wokaun, A.; Zenobi, R., Nanoscale atmospheric pressure laser ablation-mass spectrometry. *Anal. Chem.* **2001,** *73*, 1399-1402.

218. Schmitz, T. A.; Gamez, G.; Setz, P. D.; Zhu, L.; Zenobi, R., Towards nanoscale molecular analysis at atmospheric pressure by a near-field laser ablation ion trap/time-of-flight mass spectrometer. *Anal. Chem.* **2008,** *80*, 6537-6544.

219. Setz, P. D.; Schmitz, T. A.; Zenobi, R., Design and performance of an atmospheric pressure sampling interface for ion-trap/time-of-flight mass spectrometry. *Rev. Sci. Instrum.* **2006,** *77*, 024101.

220. Liang, Z.; Zhang, S.; Li, X.; Wang, T.; Huang, Y.; Hang, W.; Yang, Z.; Li, J.; Tian, Z., Tip-enhanced Ablation and Ionization Mass Spectrometry for Nanoscale Chemical Analysis. *Sci. Adv.* **2017,** *3*, eaaq1059.

221. Bradshaw, J. A.; Ovchinnikova, O. S.; Meyer, K. A.; Goeringer, D. E., Combined chemical and topographic imaging at atmospheric pressure via microprobe laser desorption/ionization mass spectrometry–atomic force microscopy. *Rapid Communications in Mass Spectrometry: An International Journal Devoted to the Rapid Dissemination of Up-to-the-Minute Research in Mass Spectrometry* **2009,** *23*, 3781-3786.

222. Becker, J. S.; Becker, J. S.; Zoriy, M. V.; Dobrowolska, J.; Matusch, A., Imaging Mass Spectrometry in Biological Tissues by Laser Ablation Inductively Coupled Plasma Mass Spectrometry. *Eur. J. Mass Spectrom.* **2007,** *13*, 1-6.

223. Becker, J. S.; Gorbunoff, A.; Zoriy, M.; Izmer, A.; Kayser, M., Evidence of Near-field Laser Ablation Inductively Coupled Plasma Mass Spectrometry (NF-LA-ICP-MS) at Nanometre Scale for Elemental and Isotopic Analysis on Gels and Biological Samples. *J. Anal. At. Spectrom.* **2006,** *21*, 19-25.

224. Wu, B.; Becker, J. S., Imaging of Elements and Molecules in Biological Tissues and Cells in the Low-Micrometer and Nanometer Range. *Int. J. Mass Spectrom.* **2011,** *307*, 112-122.

225. Zoriy, M. V.; Becker, J. S., Near-field Laser Ablation Inductively Coupled Plasma Mass Spectrometry: A Novel Elemental Analytical Technique at the Nanometer Scale. *Rapid Commun. Mass Spectrom.* **2009,** *23*, 23-30.

226. Zoriy, M. V.; Kayser, M.; Becker, J. S., Possibility of Nano-local Element Analysis by Near-field Laser Ablation Inductively Coupled Plasma Mass Spectrometry (LA-ICP-MS): New Experimental Arrangement and First Application. *Int. J. Mass Spectrom.* **2008,** *273*, 151-155.

227. Ghorai, S.; Seneviratne, C. A.; Murray, K. K., Tip-Enhanced Laser Ablation Sample Transfer for Biomolecule Mass Spectrometry. *J. Am. Soc. Mass Spectrom.* **2015,** *26*, 63-70.

228. Sahagian, K.; Kjoller, K.; Shetty, R. In *Rapid Determination of Cure Rate and Direct Identification of Spatial Variations in Cross Link Density*, **2011**; Society for Imaging Science and Technology: pp 409-410.

229. Bazylewski, P.; Ezugwu, S.; Fanchini, G., A Review of Three-Dimensional Scanning Near-Field Optical Microscopy (3D-SNOM) and Its Applications in Nanoscale Light Management. *Appl. Sci.* **2017,** *7*, 973.

230. Hecht, B.; Sick, B.; Wild, U. P.; Deckert, V.; Zenobi, R.; Martin, O. J.; Pohl, D. W., Scanning near-field optical microscopy with aperture probes: Fundamentals and applications. *J. Chem. Phys.* **2000,** *112*, 7761-7774.

231. Zenhausern, F.; O'boyle, M.; Wickramasinghe, H., Apertureless near-field optical microscope. *Appl. Phys. Lett.* **1994,** *65*, 1623-1625.

232. Anderson, N.; Bouhelier, A.; Novotny, L., Near-field photonics: tip-enhanced microscopy and spectroscopy on the nanoscale. *J. Opt. A: Pure Appl. Op.* **2006,** *8*, S227.

233. Verma, P., Tip-enhanced Raman spectroscopy: technique and recent advances. *Chem. Rev.* **2017,** *117*, 6447-6466.

234. Dazzi, A.; Prater, C. B.; Hu, Q.; Chase, D. B.; Rabolt, J. F.; Marcott, C., AFM–IR: combining atomic force microscopy and infrared spectroscopy for nanoscale chemical characterization. *Appl. Spectrosc.* **2012,** *66*, 1365-1384.

235. Kuhnke, K.; Grosse, C.; Merino, P.; Kern, K., Atomic-Scale Imaging and Spectroscopy of Electroluminescence at Molecular Interfaces. *Chem. Rev.* **2017,** *117*, 5174-5222.

236. Makarov, G. N., Laser applications in nanotechnology: nanofabrication using laser ablation and laser nanolithography. *Phys.-Usp.* **2013,** *56*, 643.

237. Zeisel, D.; Nettesheim, S.; Dutoit, B.; Zenobi, R., Pulsed laser-induced desorption and optical imaging on a nanometer scale with scanning near-field microscopy using chemically etched fiber tips. *Appl. Phys. Lett.* **1996,** *68*, 2491-2492.

238. Dutoit, B.; Zeisel, D.; Deckert, V.; Zenobi, R., Laser-induced ablation through nanometer-sized tip apertures: Mechanistic aspects. *J. Phys. Chem. B* **1997,** *101*, 6955-6959.

239. Zeisel, D.; Dutoit, B.; Deckert, V.; Roth, T.; Zenobi, R., Optical spectroscopy and laser desorption on a nanometer scale. *Anal. Chem.* **1997,** *69*, 749-754.

240. Lieberman, K.; Shani, Y.; Melnik, I.; Yoffe, S.; Sharon, Y., Near-field optical photomask repair with a femtosecond laser. *J. Microsc.* **1999,** *194*, 537-541.

241. Nolte, S.; Chichkov, B.; Welling, H.; Shani, Y.; Lieberman, K.; Terkel, H., Nanostructuring with spatially localized femtosecond laser pulses. *Opt. Lett.* **1999,** *24*, 914-916.

242. Hwang, D. J.; Chimmalgi, A.; Grigoropoulos, C. P., Ablation of thin metal films by short-pulsed lasers coupled through near-field scanning optical microscopy probes. *J. Appl. Phys.* **2006,** *99*, 044905.

243. Hwang, D. J.; Grigoropoulos, C. P.; Yoo, J.; Russo, R. E., Optical near-field ablation-induced plasma characteristics. *Appl. Phys. Lett.* **2006,** *89*, 254101.

244. Wu, B.; Becker, J. S., Bioimaging of metals in rat brain hippocampus by laser microdissection inductively coupled plasma mass spectrometry (LMD-ICP-MS) using high-efficiency laser ablation chambers. *Int. J. Mass Spectrom.* **2012,** *323*, 34-40.

245. Ovchinnikova, O. S., Toward Nanoscale Chemical Imaging: The Intersection of Scanning Probe Microscopy and Mass Spectrometry. In *Scanning Probe Microscopy of Functional Materials*, Springer: **2010**; pp 181-198.

246. Kossakovski, D.; O'Connor, S.; Widmer, M.; Baldeschwieler, J.; Beauchamp, J., Spatially resolved chemical analysis with an NSOM-based laser desorption microprobe. *Ultramicroscopy* **1998,** *71*, 111-115.

247. Heitz, J.; Yakunin, S.; Stehrer, T.; Wysocki, G.; Bäuerle, D. In *Laser-induced nanopatterning, ablation, and plasma spectroscopy in the near-field of an optical fiber tip*, XVII International Symposium on Gas Flow, Chemical Lasers, and High-Power Lasers, International Society for Optics and Photonics: **2009**; p 71311W.

248. Zorba, V.; Mao, X.; Russo, R. E., Optical far-and near-field femtosecond laser ablation of Si for nanoscale chemical analysis. *Anal. Bioanal. Chem.* **2010,** *396*, 173-180.

249. Bonse, J.; Höhm, S.; Kirner, S. V.; Rosenfeld, A.; Krüger, J., Laser-induced periodic surface structures—a scientific evergreen. *IEEE J. Sel. Topics Quantum Electron.* **2017,** *23*, 109-123.

250. Xia, Z.; Chen, C.; Fang, H.; Chen, S., The mechanism and process of nanosecond pulsed-laser induced subwavelength periodic ripples on silica films. *Appl. Surf. Sci.* **2015,** *337*, 151-157.

251. Huang, M.; Zhao, F.; Cheng, Y.; Xu, N.; Xu, Z., Origin of laser-induced near-subwavelength ripples: interference between surface plasmons and incident laser. *ACS Nano* **2009,** *3*, 4062-4070.

252. Farrokhi, H.; Zhou, W.; Zheng, H.; Li, Z., Non-ablative texturing of silicon surface with a continuous wave fiber laser. *Opt. Express* **2012,** *20*, 23180-23185.

253. Ferguson, J.; Reeves, L.; Schneider, W., Vapor absorption spectra and oscillator strengths of naphthalene, anthracene, and pyrene. *Can. J. Chem.* **1957,** *35*, 1117-1136.

254. Sambles, J. R., An electron microscope study of evaporating gold particles: the Kelvin equation for liquid gold and the lowering of the melting point of solid gold particles. *Proc. R. Soc. Lond. A* **1971,** *324*, 339-351.

255. Chapuis, P.-O.; Greffet, J.-J.; Joulain, K.; Volz, S., Heat transfer between a nano-tip and a surface. *Nanotechnology* **2006,** *17*, 2978.

256. Novotny, L.; Stranick, S. J., Near-field optical microscopy and spectroscopy with pointed probes. *Annu. Rev. Phys. Chem.* **2006,** *57*, 303-331.

257. Gupta, R.; Dyer, M.; Weimer, W., Preparation and characterization of surface plasmon resonance tunable gold and silver films. *J. Appl. Phys.* **2002,** *92*, 5264-5271.

258. Yang, L.; Li, Z.; Wang, P.; Zhang, L.; Fang, Y., Optical properties of noncontinuous gold shell engineered on silica mesosphere. *Plasmonics* **2014,** *9*, 121-127.

259. Lazare, S.; Bonneau, R.; Gaspard, S.; Oujja, M.; De Nalda, R.; Castillejo, M.; Sionkowska, A., Modeling the dynamics of one laser pulse surface nanofoaming of biopolymers. *Appl. Phys. A* **2009,** *94*, 719.

260. Lazare, S.; Tokarev, V.; Sionkowska, A.; Wiśniewski, M., Surface foaming of collagen, chitosan and other biopolymer films by KrF excimer laser ablation in the photomechanical regime. *Appl. Phys. A* **2005,** *81*, 465-470.

261. Cao, F.; Donnarumma, F.; Murray, K. K., Wavelength dependent atomic force microscope tip-enhanced laser ablation. *Appl. Surf. Sci.* **2018,** *447*, 437-441.

262. Qiu, S.; Chu, H.; Zou, Y.; Xiang, C.; Zhang, H.; Sun, L.; Xu, F., Thermochemical studies of Rhodamine B and Rhodamine 6G by modulated differential scanning calorimetry and thermogravimetric analysis. *J. Therm. Anal. Calorim.* **2016,** *123*, 1611-1618.

263. Zenobi, R.; Deckert, V., Scanning near-field optical microscopy and spectroscopy as a tool for chemical analysis. *Angew. Chem. Int. Ed.* **2000,** *39*, 1746-1756.

264. Noël, S.; Hermann, J.; Itina, T., Investigation of nanoparticle generation during femtosecond laser ablation of metals. *Appl. Surf. Sci.* **2007,** *253*, 6310-6315.

265. Tufeu, R.; Petitet, J. P.; Denielou, L.; Le Neindre, B., Experimental determination of the thermal conductivity of molten pure salts and salt mixtures. *Int. J. Thermophys.* **1985,** *6*, 315-330.

266. Ramires, M. L. V.; De Castro, C. A. N., Thermal conductivity of aqueous potassium chloride solutions. *Int. J. Thermophys.* **2000,** *21*, 671-679.

267. Bonetto, F.; Lebowitz, J. L.; Rey-Bellet, L., Fourier's law: a challenge to theorists. In *Mathematical physics 2000*, World Scientific: **2000**; pp 128-150.

268. Butt, H.-J.; Cappella, B.; Kappl, M., Force measurements with the atomic force microscope: Technique, interpretation and applications. *Surf. Sci. Rep.* **2005,** *59*, 1-152.

269. Bailo, E.; Deckert, V., Tip-enhanced Raman scattering. *Chem. Soc. Rev.* **2008,** *37*, 921-930.

270. Allison, D. P.; Mortensen, N. P.; Sullivan, C. J.; Doktycz, M. J., Atomic force microscopy of biological samples. *Wiley Interdiscip. Rev. Nanomed. Nanobiotechnol.* **2010,** *2*, 618-634.

271. Bradshaw, J. A.; Ovchinnikova, O. S.; Meyer, K. A.; Goeringer, D. E., Combined chemical and topographic imaging at atmospheric pressure via microprobe laser

desorption/ionization mass spectrometry–atomic force microscopy. *Rapid Commun. Mass Spectrom.* **2009,** *23*, 3781-3786.

272. Zoriy, M. V.; Becker, J. S., Near-field laser ablation inductively coupled plasma mass spectrometry: a novel elemental analytical technique at the nanometer scale. *Rapid Commun. Mass Spectrom.* **2009,** *23*, 23-30.

273. Bezanilla, M.; Manne, S.; Laney, D. E.; Lyubchenko, Y. L.; Hansma, H. G., Adsorption of DNA to mica, silylated mica, and minerals: characterization by atomic force microscopy. *Langmuir* **1995,** *11*, 655-659.

274. Mandel, M.; Igambi, L.; Bergendahl, J.; Dodson, M.; Scheltgen, E., Correlation of melting temperature and cesium chloride buoyant density of bacterial deoxyribonucleic acid. *J. Bacteriol.* **1970,** *101*, 333-338.

275. Nelson, R. W.; Rainbow, M. J.; Lohr, D. E.; Williams, P., Volatilization of high molecular weight DNA by pulsed laser ablation of frozen aqueous solutions. *Science* **1989,** *246*, 1585-1587.

276. Wang, K.; Donnarumma, F.; Herke, S. W.; Herke, P. F.; Murray, K. K., Infrared laser ablation sample transfer of tissue DNA for genomic analysis. *Anal. Bioanal. Chem.* **2017,** *409*, 4119-4126.

277. Berkenkamp, S.; Kirpekar, F.; Hillenkamp, F., Infrared MALDI mass spectrometry of large nucleic acids. *Science* **1998,** *281*, 260-262.

278. Romano, L. J.; Levis, R. J., Nondestructive laser vaporization of high molecular weight, single-stranded DNA. *J. Am. Chem. Soc.* **1991,** *113*, 9665-9667.

279. Colotte, M.; Coudy, D.; Tuffet, S.; Bonnet, J., Adverse effect of air exposure on the stability of DNA stored at room temperature. *Biopreserv. Biobank.* **2011,** *9*, 47-50.

280. Matsuo, S.; Toyokuni, S.; Osaka, M.; Hamazaki, S.; Sugiyama, T., Degradation of DNA in dried tissues by atmospheric oxygen. *Biochem. Biophys. Res. Commun.* **1995,** *208*, 1021-1027.

281. Lü, J.; Li, H.; An, H.; Wang, G.; Wang, Y.; Li, M.; Zhang, Y.; Hu, J., Positioning isolation and biochemical analysis of single DNA molecules based on nanomanipulation and single-molecule PCR. *J. Am. Chem. Soc.* **2004,** *126*, 11136-11137.

282. Zhang, Y.; Hu, X.; Sun, J.; Shen, Y.; Hu, J.; Xu, X.; Shao, Z., High-resolution imaging and nano-manipulation of biological structures on surface. *Microsc. Res. Tech.* **2011,** *74*, 614-626.

283. Kalisky, T.; Blainey, P.; Quake, S. R., Genomic analysis at the single-cell level. *Annu. Rev. Genet.* **2011,** *45*, 431-445.

284. Navin, N.; Kendall, J.; Troge, J.; Andrews, P.; Rodgers, L.; McIndoo, J.; Cook, K.; Stepansky, A.; Levy, D.; Esposito, D., Tumour evolution inferred by single-cell sequencing. *Nature* **2011,** *472*, 90.

285. Shapiro, E.; Biezuner, T.; Linnarsson, S., Single-cell sequencing-based technologies will revolutionize whole-organism science. *Nat. Rev. Genet.* **2013,** *14*, 618.

286. Zong, C.; Lu, S.; Chapman, A. R.; Xie, X. S., Genome-wide detection of single-nucleotide and copy-number variations of a single human cell. *Science* **2012,** *338*, 1622-1626.

287. Gawad, C.; Koh, W.; Quake, S. R., Single-cell genome sequencing: current state of the science. *Nat. Rev. Genet.* **2016,** *17*, 175.

288. Vasdekis, A. E.; Stephanopoulos, G., Review of methods to probe single cell metabolism and bioenergetics. *Metab. Eng.* **2015,** *27*, 115-135.

289. Wang, D.; Bodovitz, S., Single cell analysis: the new frontier in 'omics'. *Trends Biotechnol.* **2010,** *28*, 281-290.

290. Rubakhin, S. S.; Romanova, E. V.; Nemes, P.; Sweedler, J. V., Profiling metabolites and peptides in single cells. *Nat. Methods* **2011,** *8*, S20.

291. Macaulay, I. C.; Voet, T., Single cell genomics: advances and future perspectives. *PLoS Genet.* **2014,** *10*, e1004126.

292. Saliba, A.-E.; Westermann, A. J.; Gorski, S. A.; Vogel, J., Single-cell RNA-seq: advances and future challenges. *Nucleic Acids Res.* **2014,** *42*, 8845-8860.

293. Datta, S.; Malhotra, L.; Dickerson, R.; Chaffee, S.; Sen, C. K.; Roy, S., Laser capture microdissection: Big data from small samples. *Histol. Histopathol.* **2015,** *30*, 1255.

294. Frumkin, D.; Wasserstrom, A.; Itzkovitz, S.; Harmelin, A.; Rechavi, G.; Shapiro, E., Amplification of multiple genomic loci from single cells isolated by laser micro-dissection of tissues. *BMC Biotechnol.* **2008,** *8*, 17.

295. Espina, V.; Wulfkuhle, J. D.; Calvert, V. S.; VanMeter, A.; Zhou, W.; Coukos, G.; Geho, D. H.; Petricoin III, E. F.; Liotta, L. A., Laser-capture microdissection. *Nat. Protoc.* **2006,** *1*, 586.

APPENDIX. LETTERS OF PERMISSION

VITA

Fan Cao was born in Yangzhou, China in 1989. He received a Bachelor of Science degree with a major of pharmaceutics from China Pharmaceutical University in 2011. After graduation, he decided to pursue a Master of Science degree in analytical chemistry in Hong Kong Baptist University with a fellowship under supervision of Dr. Kelvin Leung in 2012. After one year working experience as an analytical scientist in the R&D department from Dawnray Pharmaceutical, he decided to extend his study in analytical chemistry abroad in the United States. He joined Dr. Kermit K. Murray research group in Louisiana State University (LSU) for the doctoral program of analytical chemistry. During his doctoral program, he received an average 4.0 GPA for all the lessons. He is currently a member of the American Society of Mass Spectrometry (ASMS) and American Chemistry Society (ACS) and has presented several posters and talks in eight conferences. He has published two first-author papers and three co-author papers. In addition, he has two other first-author manuscripts in preparation for publishing. Mr. Cao is currently a candidate of Doctor of Philosophy in chemistry, which is planned to be awarded at the Spring 2019 Commencement.